Analysis of Active Compensation for Shock, Vibration, and Wind-up in Disk Drives

by

David Bradley Davies

SUBMITTED TO THE DEPARTMENT OF
MECHANICAL ENGINEERING
IN PARTIAL FULFILLMENT OF THE
REQUIREMENTS FOR THE
DEGREE OF
MASTER OF SCIENCE IN MECHANICAL ENGINEERING

at the

MASSACHUSETTS INSTITUTE OF TECHNOLOGY

June 1991

Signature of Author: _____

Department of Mechanical Engineering
May 10, 1991

Certified by: _____

Kamal Youcef-Toumi
Associate Professor, Department of Mechanical Engineering

Certified by: _____

Michael D. Sidman Ph.D.
Consultant Engineer, Digital Equipment Corporation

Accepted by: _____

Professor Ain A. Sonin
Chairman, Departmental Graduate Committee

Analysis of Active Compensation for Shock, Vibration, and Wind-up in Disk Drives

by

David Bradley Davies

Submitted to the Department of Mechanical Engineering
on May 10, 1991 in partial fulfillment of the
requirements for the Degree of
Master of Science in Mechanical Engineering

ABSTRACT

This thesis describes analysis and experimental verification of an acceleration feedback active compensation system for shock, vibration, and wind-up acting on a disk drive with a balanced, rotary actuator. Included is a model of the drive dynamics, simulation of the active closed loop servo system, and laboratory verification of the simulated results.

A twelfth order model was developed to explain the fundamental drive behavior in conjunction with its shock mount suspension. The model was verified through impact, modal, and shaker table analysis. A complete drive state-space model including drive dynamics and controller action was also developed and verified. It was found that sensing and feedback of drive angular acceleration acts to simultaneously minimize the track position error due to external shock, vibration, and wind-up.

Laboratory results show that track position error oscillation due to shock, vibration, and wind-up is virtually eliminated leading to significant improvements in average seek time.

Thesis Advisor: Kamal Youcef-Toumi
Associate Professor, Department of Mechanical Engineering

Acknowledgments

I would foremost like to thank the Digital Equipment Corporation Storage Systems Engineering and Technology Group for the financial backing of this work.

I would also like to thank the Digital Equipment Corporation Storage Systems Servo/Mechanical Advanced Development Group for providing the technical assistance and hardware necessary to complete this research. Specifically, I would like to thank my supervisor, Mike Sidman, for his insight, advice, and technical expertise.

Finally, I would like to thank Prof. Kamal Youcef-Toumi at MIT for his technical guidance, support, and willingness to work across the miles.

Contents

List of Figures

List of Tables

Chapter 1

Introduction

Shock and vibration is an area of growing concern for compact, high density disk drive products. With track densities exceeding 2000 tracks per inch, the passive damping provided by existing drive shock mounts may not be adequate to attenuate the effects of shock, vibration, and self-induced drive excitation called wind-up. To provide for necessary improvements in tracking accuracy and seek/settling characteristics, an active compensation system is desirable.

1.1 Problem Definition

A disk drive is composed of a Head/Disk Assembly (HDA) isolated from an external supporting structure by compliant shock mounts. A sketch of such a system is shown in Figure 1.1. The shock mounts serve to dampen external shock and vibration that would otherwise adversely affect drive performance. As a side effect, the existence of

shock mounting leads to wind-up.

Wind-up is induced by actuator positioning, especially during high acceleration seeks. A disk drive 'seek' is defined as the operation of moving the drive read/write heads from one disk track to another. During a seek, the actuator applies a torque against the HDA. This torque is transmitted through the compliant shock mounts to the supporting structure. The result is rotational oscillation of the HDA itself within the supporting structure. The problem exists when the heads of the actuator approach their desired track. Since the HDA is oscillating, the track is now rotating with respect to the read/write heads causing track position error.

A trade-off exists in the design of disk drive shock mounts. On one extreme, the shock mounts can be very stiff to minimize the effect of wind-up; however, most damping of external vibration propagated by the supporting frame to the HDA will be lost. On the other hand, if the shock mounts are very compliant, minimizing the effect of external shock and vibration, the wind-up problem may become severe. Therefore, a compromise is normally made between allowable external shock and vibration and allowable wind-up effects. But, with increasing disk track density, a compromise has become harder to reach.

As such, an active disturbance compensation system (ADCS) may be a desirable disk drive supplement. The most common form of active compensation involves the measurement of HDA acceleration. In theory, the acceleration can be fed through a gain and into the actuator servo control loop to compensate the position of read/write

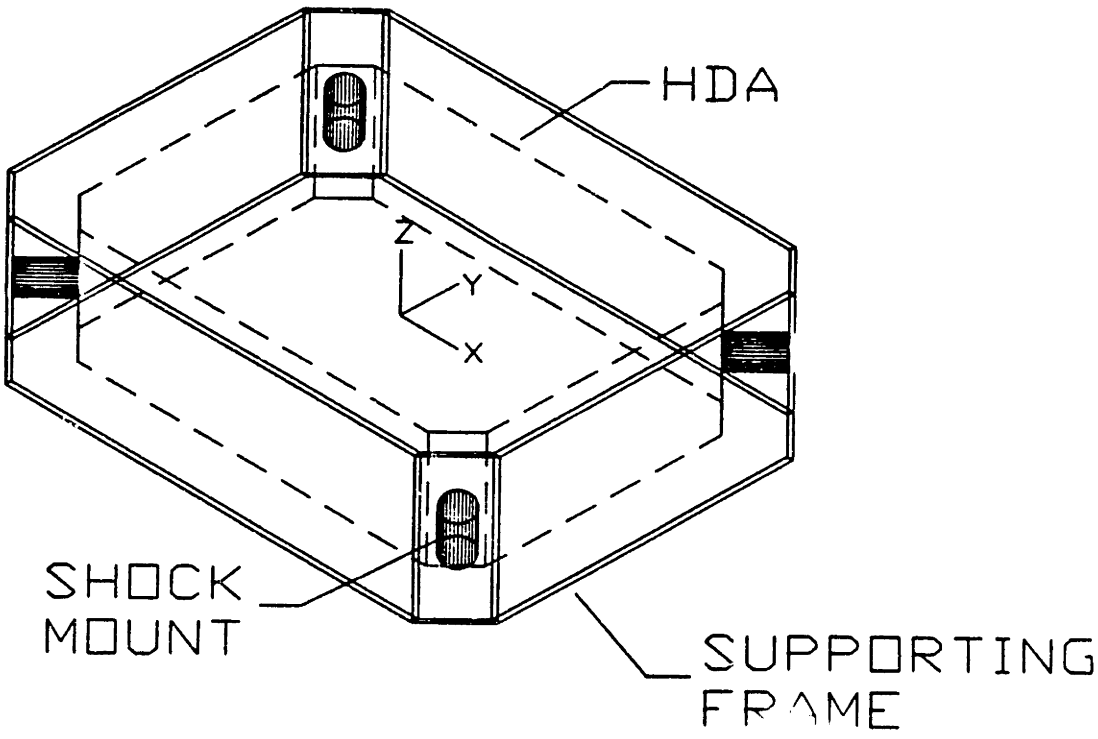

Figure 1.1: Sketch of drive system.

heads for a disturbance. This is done by providing additional acceleration in positioning the actuator in anticipation of radial acceleration of the data track. Previously, this strategy was not practical due to both the prohibitively high cost and poor signal quality of accelerometers. However, with the price of accelerometers decreasing substantially and recent technological improvements in accelerometer design, this type of strategy is now worth consideration.

1.2 Previous Work

The concept of an active compensation system has existed for more than 10 years in different forms.

In a 1977 U.S. Patent, Robert A. White proposed a method for active disturbance compensation of disk storage devices [1]. He proposed that:

> "An accelerometer is mounted on a fixed base of the system and receives the undelayed shock force and provides an output signal indicative of the magnitude and direction of the shock force being applied to the system. The undelayed output signal on the accelerometer is applied to transducer means which move the flying head away from or toward the magnetic device in anticipation of the shock force disturbing the gap between the flying head and the rotation magnetic device."

A sketch of White's invention is shown in Figure 1.2. The use of an accelerometer (27) to measure the external disturbance, the placement of the accelerometer exter-

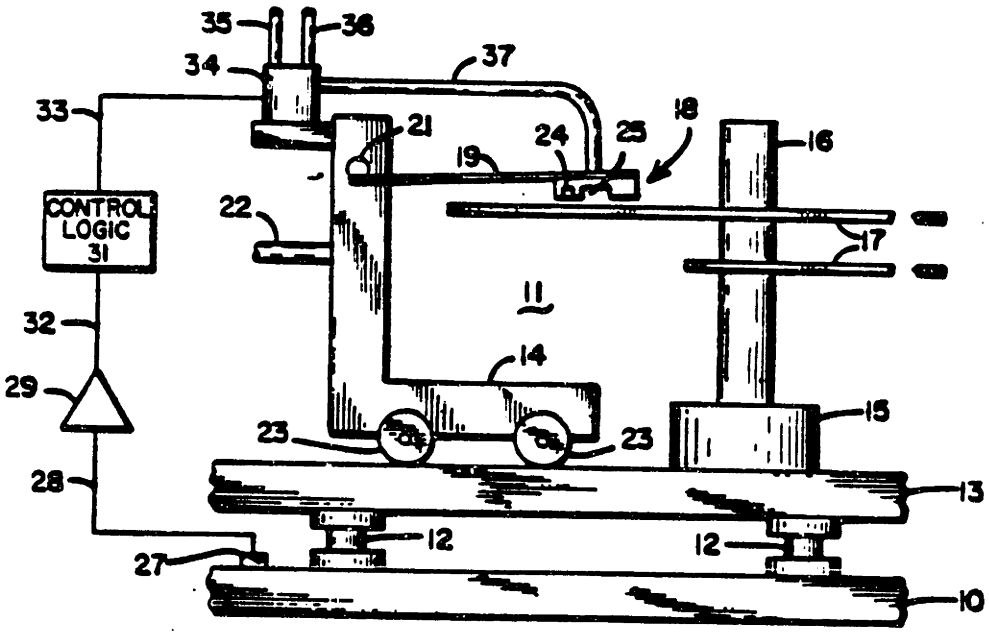

Figure 1.2: A pictorial and logic diagram representation of the shock compensating system invention applied to an electromechanical servo adjusted flying head and a disk file memory system.

nal to the drive shock mounts (12) to *anticipate* the drive error due to an external disturbance, and the feedback of the signal (28,29,32,31,33) to reposition the flying heads (18) for the disturbance, are key elements of this concept.

In 1986, Vernon Lynn Knowles and Darwin Mitchel Hanks claimed a number of new points [2] . First, they suggested that the shock compensating system proposed by White can compensate the actuator for not only external disturbances, but also internally generated disturbances including vibration due to the spindle drive or the actuator drive motor (wind-up). To accomplish this, they proposed that the accelerometer should be mounted directly to the HDA, internal to the shock mounts. This change, they claimed, would allow for a more accurate measurement of the magnitude of internally generated disturbances. Also, by mounting the accelerometer internal to the shock mount system, a knowledge of the shock mount transfer function is not required. This feature is desirable as the shock mount characteristics may change over time.

In 1986, Moriya, Shiragami, and Yamaguchi [4] proposed a compensation system in which optical acceleration detectors mounted external to the shock mounts are used to detect externally induced vibration of the HDA. The measured signal is then

> "... applied to control section for stabilization of the control system and also, for proper treatment upon application of excessively large external vibrations or impacts with consequent improvements of reliability and stability of the apparatus."

In 1989, Aruga, Mizoshita, Iwatsubo and Hatagami [5] proposed that control of a multi-positioning drive can be achieved using information concerning the HDA acceleration. They proposed that by measuring the acceleration of the HDA caused by the motion of one actuator and feeding this information to all actuators, the position error of the system of actuators can be reduced. The results of their tests using two linear actuators are described in the paper *Acceleration Feedforward Control for Head Positioning in Magnetic Disk Drives* [6].

Finally, Dunstan, Hogg, Scura, and Sheu [7] proposed a compensation system in which the instantaneous rotational velocity of the HDA is measured and used in interpreting the acceleration of the drive for the purpose of error compensation. This method is accomplished by measuring the rotational velocity resulting from accelerations applied to the HDA. The velocity is derived from the instantaneous changes in disk rotational speed as seen by the magnetic heads. The measured velocity is filtered and differentiated to produce an acceleration signal. The signal is then fed through a gain and into the servo positioning loop for the purpose of error correction.

1.3 Thesis Outline

In developing an active compensation system for use in a disk drive with a balanced, rotary actuator, a number of steps were required. First, a rigorous analysis of the drive dynamics was performed to develop an understanding of the response of this class of drives to all disturbance type inputs including wind-up. Based on the devel-

oped model, computer simulation was performed to predict an optimal compensation system. From this information, laboratory testing was completed to verify the effectiveness of the system.

Chapter 2 outlines basic disk drive terminology as well as details of the test disk drive specifications. Chapter 3 begins with modeling efforts including assumptions and evaluation of model results. This chapter ends with a detailed twelfth order disk drive dynamic model based on the balanced, rotary-actuated test drive. The next chapter presents the work involved in integrating the drive dynamic model and the active compensation system into a software simulation. This chapter evaluates the results of the simulation and presents an optimal acceleration feedback controller design. Following this, Chapter 5 presents the laboratory results in using accelerometers to achieve effective active disturbance compensation. The final chapter contains a discussion of the results and recommendations for future work.

Chapter 2

Drive Description

This chapter provides basic background information on disk drive terminology as well as the layout information for the test drive.

The experimental research was performed on a 5.25" disk drive. The drive has a radial storage density exceeding 2000 data tracks per inch. Head positioning is accomplished through a balanced, rotary actuator, characteristic of many drives on the market today.

The disk drive is composed of a Head/Disk Assembly (HDA) and electronic circuitry isolated from an external supporting frame by compliant shock mounts. A basic description of individual components is found below.

2.1 Head/Disk Assembly

The HDA is comprised of all components of the disk drive internal to the shock mounts. The HDA's two integral parts are the spindle and the actuator. The spindle is comprised of the disks and the spindle hub including the spindle bearing and motor. The actuator is comprised of the read/write heads, the arms supporting the heads, and the actuator hub assembly. A top view showing the relative position of the actuator and the spindle in the HDA is shown in Figure 2.1.

2.2 Supporting Frame

The external supporting frame has four mounting holes at the base. These holes allow for the attachment of the supporting frame to a mounting plate. The plate then can be slid into a stacked drive or similar mounting configuration.

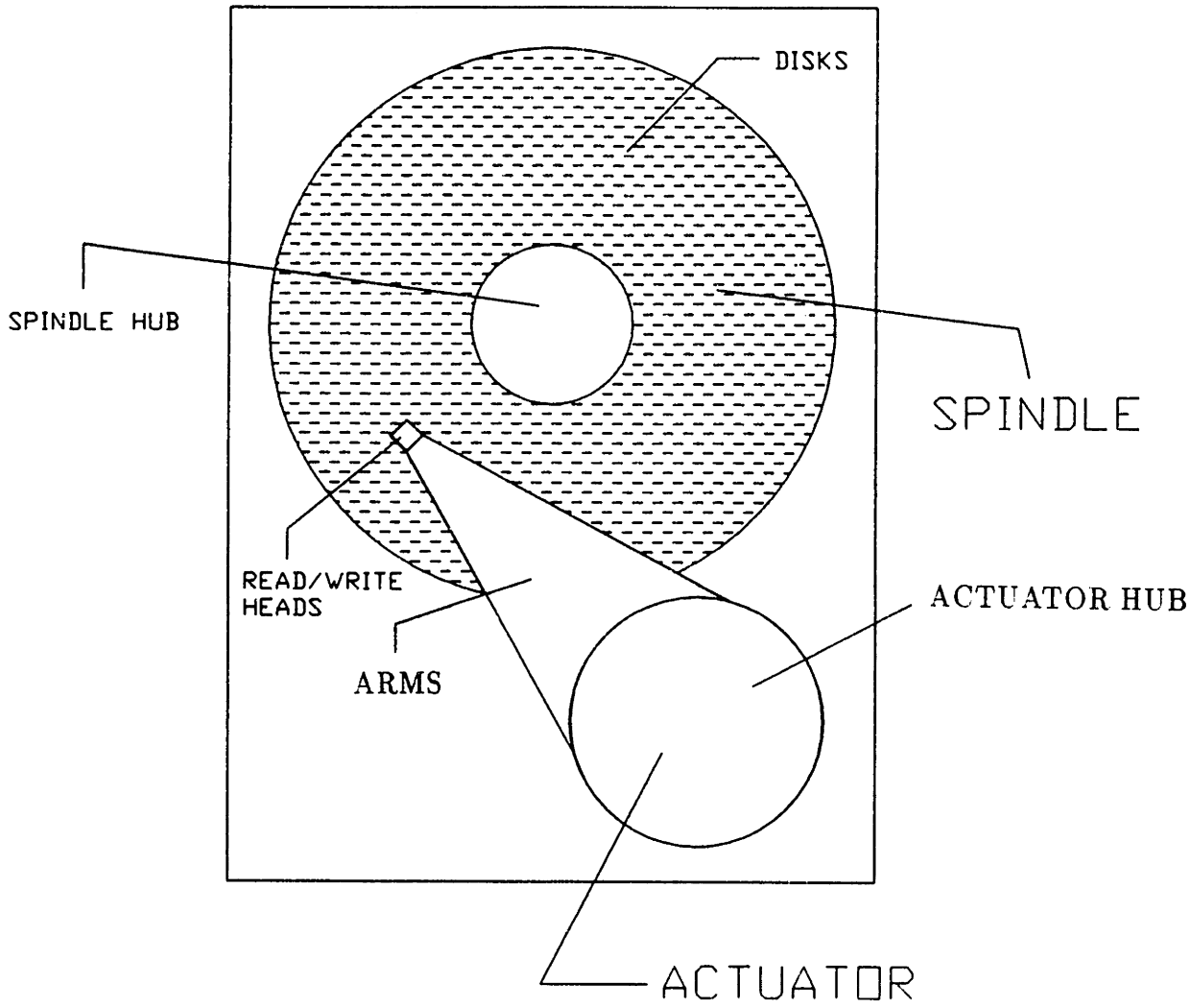

Figure 2.1: Illustration of the relative position of the actuator and spindle in the HDA.

Chapter 3

Modeling of HDA/Shock Mount Dynamics

In designing an effective ADCS, an understanding of the fundamental dynamic behavior of the HDA was required. This understanding came through modeling and experimental evaluation of modeled results. From an accurate model, computer simulation could be performed to optimize an ADCS. Therefore, this work provided a starting point for laboratory testing and evaluation of an active compensation system.

This chapter presents the modeling of a disk drive system beginning with a list of potential drive model characteristics. Following this, preliminary model assumptions are discussed, and the most basic model is introduced. Then, laboratory model evaluation is presented including a brief description of hardware and test procedures. The chapter concludes with a detailed model of the test drive including experimental

evaluation supporting the final drive model.

3.1 Model Characteristics

The fundamental goal of the modeling procedure was to find the simplest model to effectively predict the motion of the HDA. To reach this point, all relevant modeling parameters and effects were evaluated. The following list contains the most prominent of the modeling parameters and effects:

- Moment of inertia of the HDA.
- Shock mount damping.
- Shock mount stiffness.
- Inertia of the HDA.
- Location of HDA center of mass.
- Shock mount position and orientation.
- Input type and location.
- Shock mount non-linearity.
- Shock mount cross-coupling (both stiffness and damping).
- Compliance of the HDA housing.

- Torsion of the spindle.
- Precession of the spindle.
- Gyroscopic effects.
- Actuator bearing friction.

In building a model effective enough to describe the basic low frequency HDA dynamics, many of the above parameters were assumed negligible as discussed in Section 3.2.

3.2 Initial Assumptions

To begin modeling, initial assumptions were required. Each of the initial test drive model assumptions is discussed in the following section.

3.2.1 Actuator

The rotary actuator[1] was assumed to be perfectly balanced about a frictionless bearing and was assumed to be rigid and constrained to rotation only in its horizontal plane of rotation with respect to the HDA. Therefore, no translational motion of the actuator in its plane of rotation was permitted with respect to the HDA. As such, a pure rotation of the HDA would leave the orientation of an uncontrolled actuator

[1]The 'actuator' is comprised of the read/write heads, the arms supporting the heads, and the actuator hub assembly as discussed in Section 2.1.

fixed in inertial space, while changing the relative position of the actuator with respect to the HDA, as shown exaggerated in Figure 3.1. Track position error is due to the difference in radial position between a selected read/write data head and a specific disk track center. Based on the assumption of a balanced, rigid, frictionless actuator, all track position error could be assumed to be due only to pure rotation of the HDA.

Also, all reaction torque transmitted to the HDA during seek activity in the drive from the actuator was modeled as a pure couple or a pure torque input to the HDA.

Finally, since the actuator servo bandwidth is approximately 400Hz, the actuator servo control system was assumed to be ineffective in compensating for disturbances above this frequency.

3.2.2 Spindle

The spindle was also assumed to be rigidly mounted in its plane of rotation, and the imbalance and gyroscopic effects due to the spindle were assumed to be negligible. Finally, the effect of the spindle servo on the drive dynamic response was assumed to be insignificant, as the spindle drive motor servo bandwidth is approximately 5Hz. Given that the spindle reaction torque disturbances are so low in frequency relative to head positioning servo bandwidths, it was assumed that their effect on the closed loop tracking error was negligible.

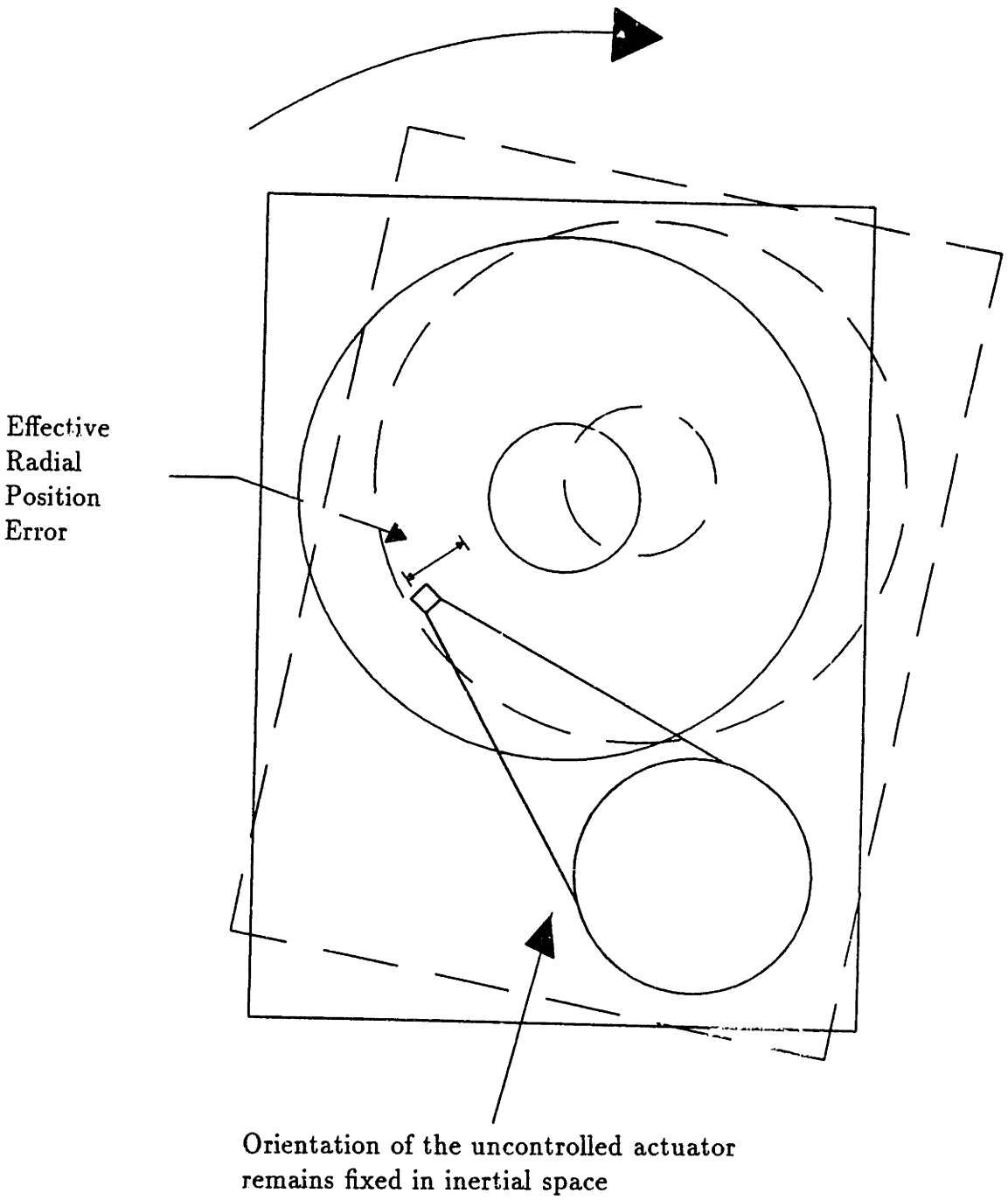

Figure 3.1: Motion of the actuator due to an exaggerated rotation of the HDA.

3.2.3 HDA Housing and Shock Mounts

The HDA was assumed to behave as a rigid body. Therefore, all flexibility of the HDA was assumed to be negligible in the frequency range of interest (< 400Hz).

The energy absorbing shock mounts act as highly nonlinear spring/dashpots. Due to their anisotropic nature, the stiffness/damping varies with the speed of loading. However, for small motions, the shock mounts were assumed to behave in a linear fashion. Also, for small motion the orientation of the shock mounts was assumed to be unimportant, and the shock mounts were lumped into a single idealized spring/damper element.

All compliance due to the external supporting frame was assumed to be lumped into the shock mount compliance.

Initially, cross-coupling between motion in orthogonal directions was assumed to be negligible. This included dynamic, damping, and stiffness coupling between translational/ orthogonal-translational, rotational/ orthogonal-rotational, and translational/ rotational motion.

3.3 Initial Modeling

Based on the initial assumptions discussed in Section 3.2, a simple single-degree-of-freedom model of the HDA was constructed as shown in Figure 3.2. This pure torsional second-order system is excited only by a torque input, τ, and the angular position output, θ, can be perfectly predicted for all time. In this case, the parameter

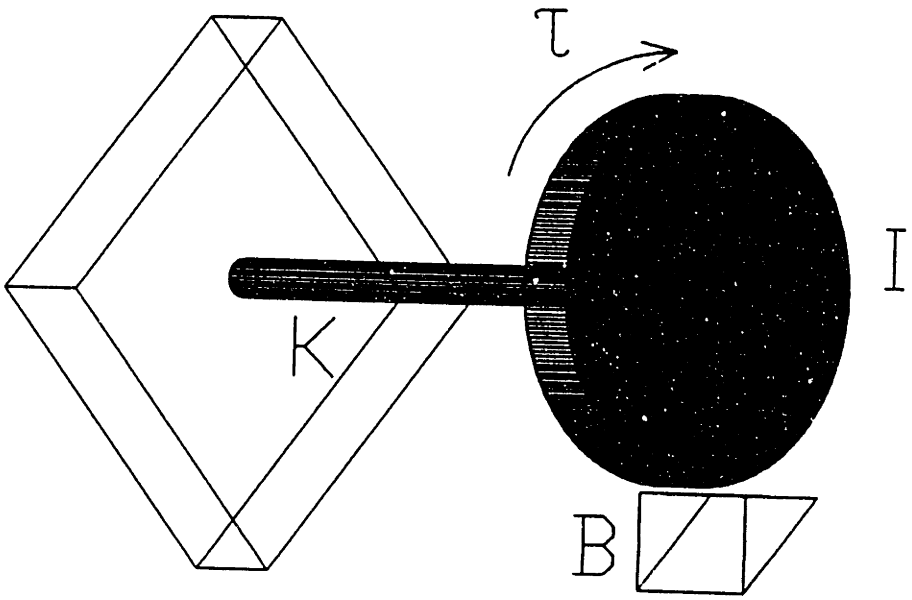

Figure 3.2: Single degree-of-freedom torsional model.

(I) represents the moment of inertia of the HDA, the parameter (K) represents the torsional stiffness of the shock mounts, and the parameter (B) represents the torsional damping of the shock mounts. The input to the system (τ) could represent the torque applied by the actuator during a seek.

Because the track position error was assumed to be due only to pure rotation of the HDA, and since the other coupling factors were assumed insignificant, this simple model provided a starting point for laboratory analysis.

The equations of motion of this system are given by:

$$I\ddot{\theta} + B\dot{\theta} + K\theta = \tau \tag{3.1}$$

where θ is the absolute rotational position of the HDA with respect to an inertial reference frame[2].

[2]Note: this model does not account for rotational motion of the supporting frame.

3.4 Laboratory Hardware and Test Process

To check the validity of the single-degree-of-freedom model, laboratory testing was required. Testing took the form of impact testing, modal analysis, shaker table analysis, and drive hardware-based testing.

3.4.1 Hardware

This section briefly describes the hardware used for each test procedure. More complete hardware specifications are found in Appendix A.

Impact Testing

Impact testing was performed using a PCB Model 086B01 Impulse Force Hammer. Response measurements were made using both PCB Model 309A Piezoelectric Accelerometers and Kaman Model KD2810-1U Inductive Position Sensors. Data acquisition was taken through a Hewlett Packard 3562A Dynamic Signal Analyzer.

Modal Analysis

Modal Analysis was completed using a PC based Hewlett Packard 3566A Dynamic Signal Analyzer with Structural Measurement Systems STARModal Software. Measurements were taken using the PCB Model 086B01 Impulse Force Hammer and the PCB Model 309A Piezoelectric Accelerometers.

Shaker Table Analysis

Shaker table analysis was completed by mounting the drive supporting frame to a rigid plate, placing the plate on a set of linear slides, and then exciting the plate with a sinusoidal input. The sinusoidal input was generated using a Hewlett Packard 3562A Dynamic Signal Analyzer. The HDA response was measured using PCB Model 309A Piezoelectric Accelerometers and interpreted using the Hewlett Packard 3562A Dynamic Signal Analyzer.

Drive Hardware Based Testing

Seek testing was performed using software that completed both random and specific actuator seeks. Drive response was measured using PCB Model 309A Piezoelectric Accelerometers, Kaman Inductive Sensors, and drive circuit board based hardware that provided both actuator motor current and track position error. Summing junctions on the drive circuit board were also available as input points for swept sine actuator testing and controller profile evaluation.

3.4.2 Testing and Results

The following sections briefly discuss the experimental procedure followed for each type of testing. The results of each test procedure are presented and discussed at the end of each specific section.

Impact Testing

Impact testing provided a simple initial evaluation of the HDA dynamic response. This type of testing was performed by imparting an impulse to the HDA, normally with a calibrated impact hammer, and then measuring either the frequency response of the system from the point of impact to an accelerometer, the acceleration of the system as measured by the accelerometer, or the positional response of the system as measured by position sensors.

To conduct measurements of the HDA position during impact testing, the HDA supporting frame was first rigidly mounted. For accurate results, the position sensors were also then rigidly mounted to the same baseplate as shown in Figure 3.3.

A hammer was then used to lightly strike the HDA at various points. The Hewlett Packard 3562A Dynamic Signal Analyzer then captured the time response as measured by the position sensors. Angular position was obtained by subtracting the linear information from the sensors Y1 and Y2. Figure 3.4 shows the translational motion of the HDA due to an impact in the direction of the center of the HDA (drive off) as measured by a single inductive sensor. In the figure, the initial higher frequency response is due to the fact that the impulse was not perfectly applied through the center of mass of the HDA. However, both the damped natural frequency and the damping for the translational response can be easily interpreted from the figure.

In comparison, Figure 3.5 shows the position of the HDA as measured by sensors Y1 and Y2 during a 1300 track seek by the drive actuator. Figure 3.6 shows a scaled

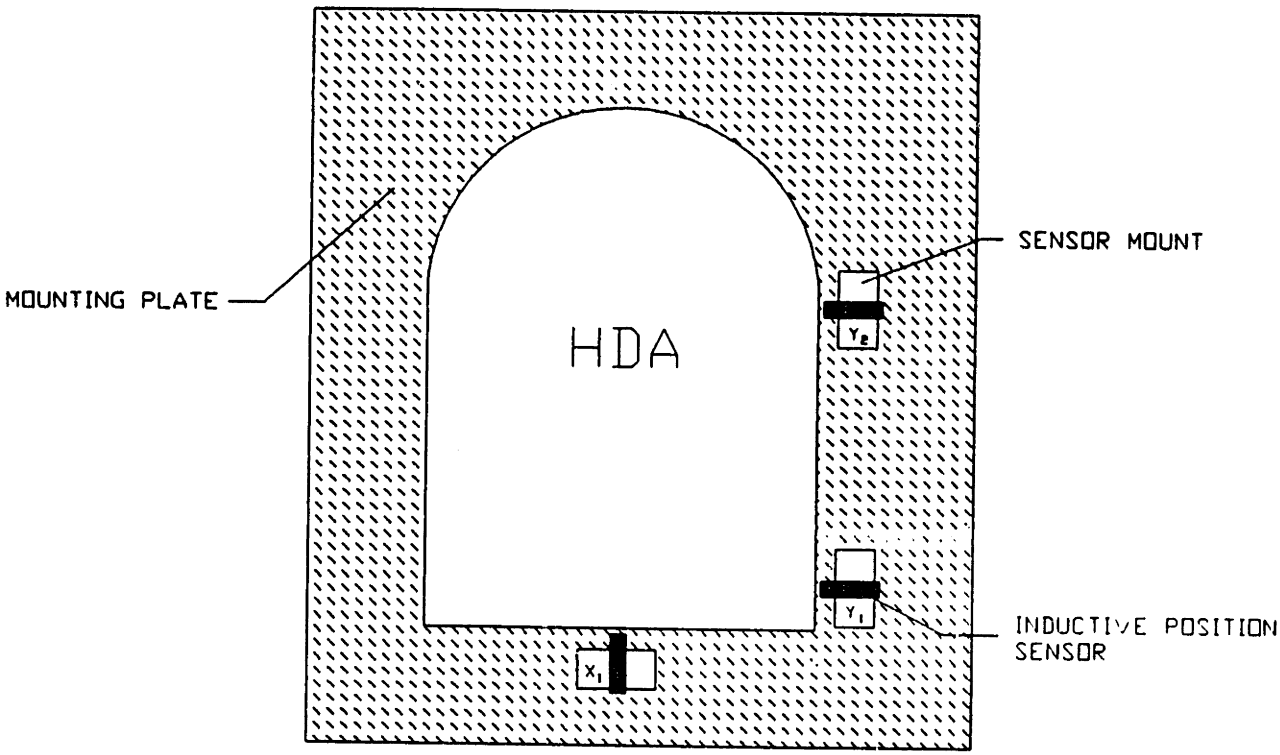

Figure 3.3: Position of inductive sensors.

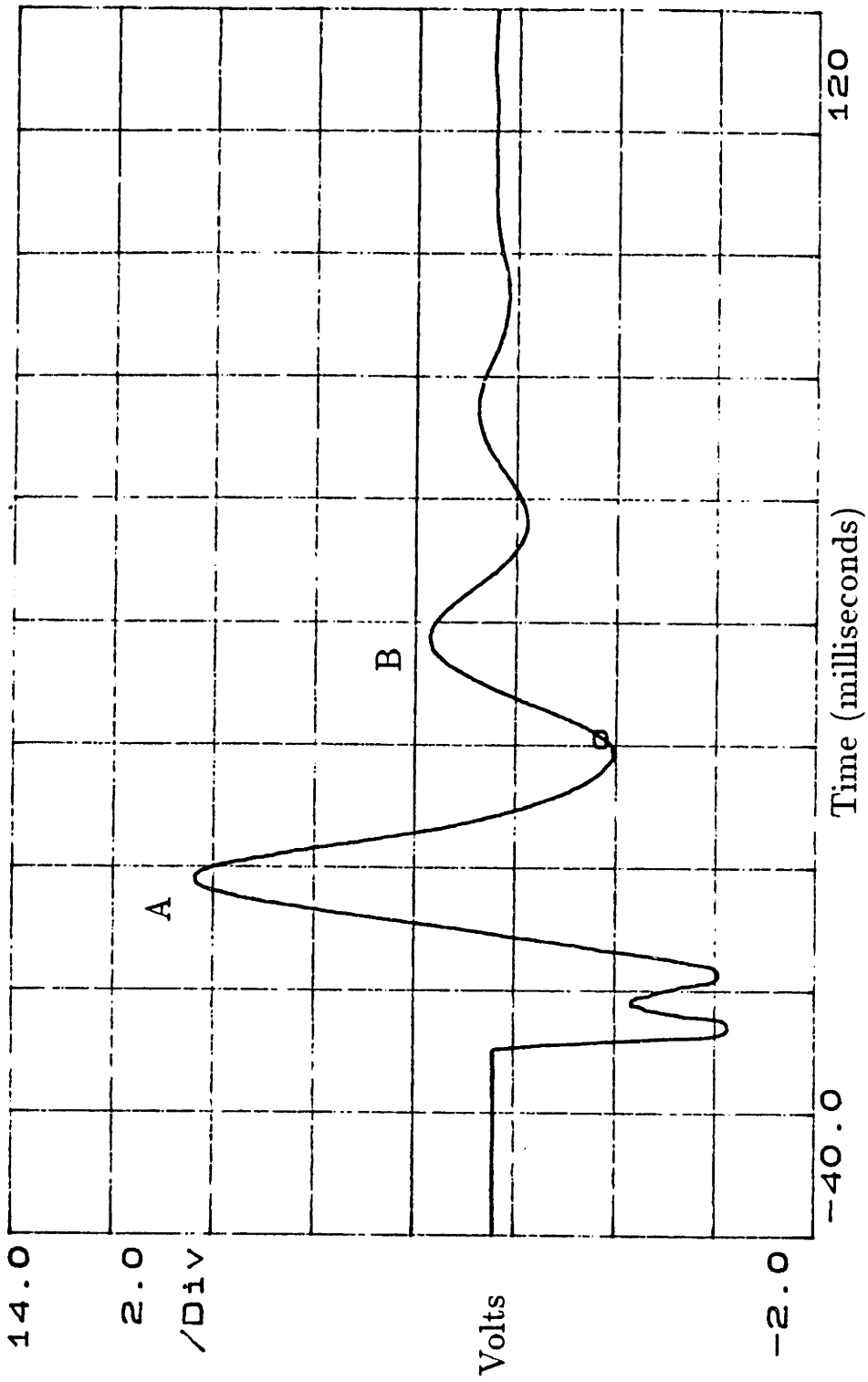

Figure 3.4: Translational motion of the HDA due to an impact in the direction of the center of mass.

rotational position of the HDA, obtained by subtracting the output of the sensor Y2 from the output of the sensor Y1. In this case, the observed damped natural frequency is much higher than that observed for translational motion.

This type of testing provided useful information about both the damped natural frequency of the HDA and the shock mount damping for both translational and rotational motion in the plane observable by the inductive sensors.

The damped natural frequency for motion in the plane of the disk stack was approximated by measuring the time between successive peaks in Figures 3.4 and 3.6. For example, in Figure 3.4, the measured time between peaks A and B is approximately 0.03 seconds. The inverse of this (33.3Hz) gives the damped natural frequency of the system for translational motion along this axis.

The damping ratio was estimated by comparing the magnitudes of successive peaks. For example, by measuring the magnitude of two successive peaks in Figure 3.4 (A = 2.09, B= 0.44) and using the formula for the logarithmic decrement shown below [8]:

$$\zeta = \frac{\delta}{\sqrt{4\pi^2 + \delta^2}} \tag{3.2}$$

where:

$$\delta = \ln \frac{A}{B} \tag{3.3}$$

The damping ratio, ζ, was found to be 0.20 for motion in translational directions (X and Y) and 0.225 for motion in a rotational direction in the plane of the disks.

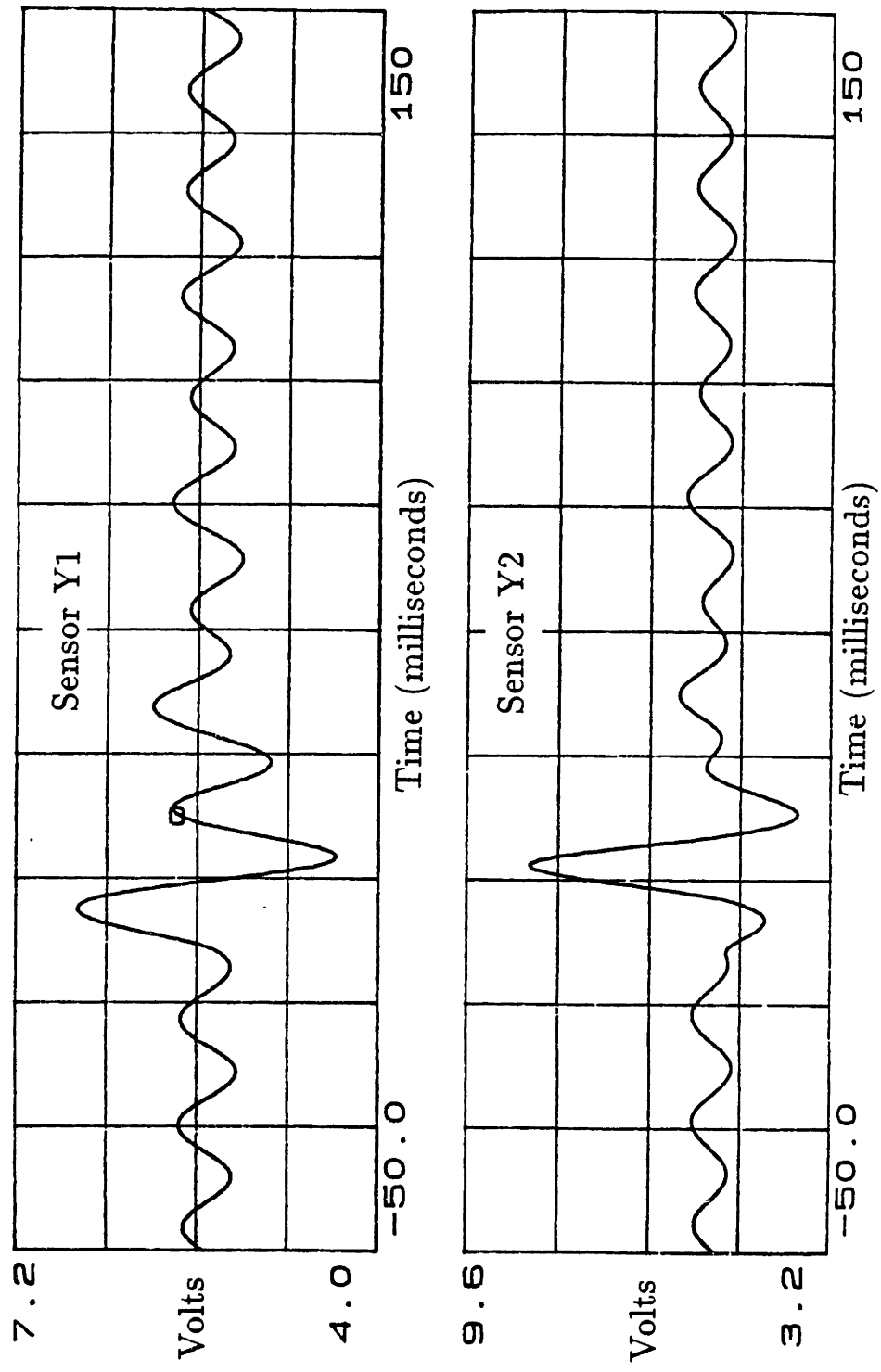

Figure 3.5: Translational motion of the HDA as measured by inductive position sensors Y1 and Y2 during a 1300 track seek.

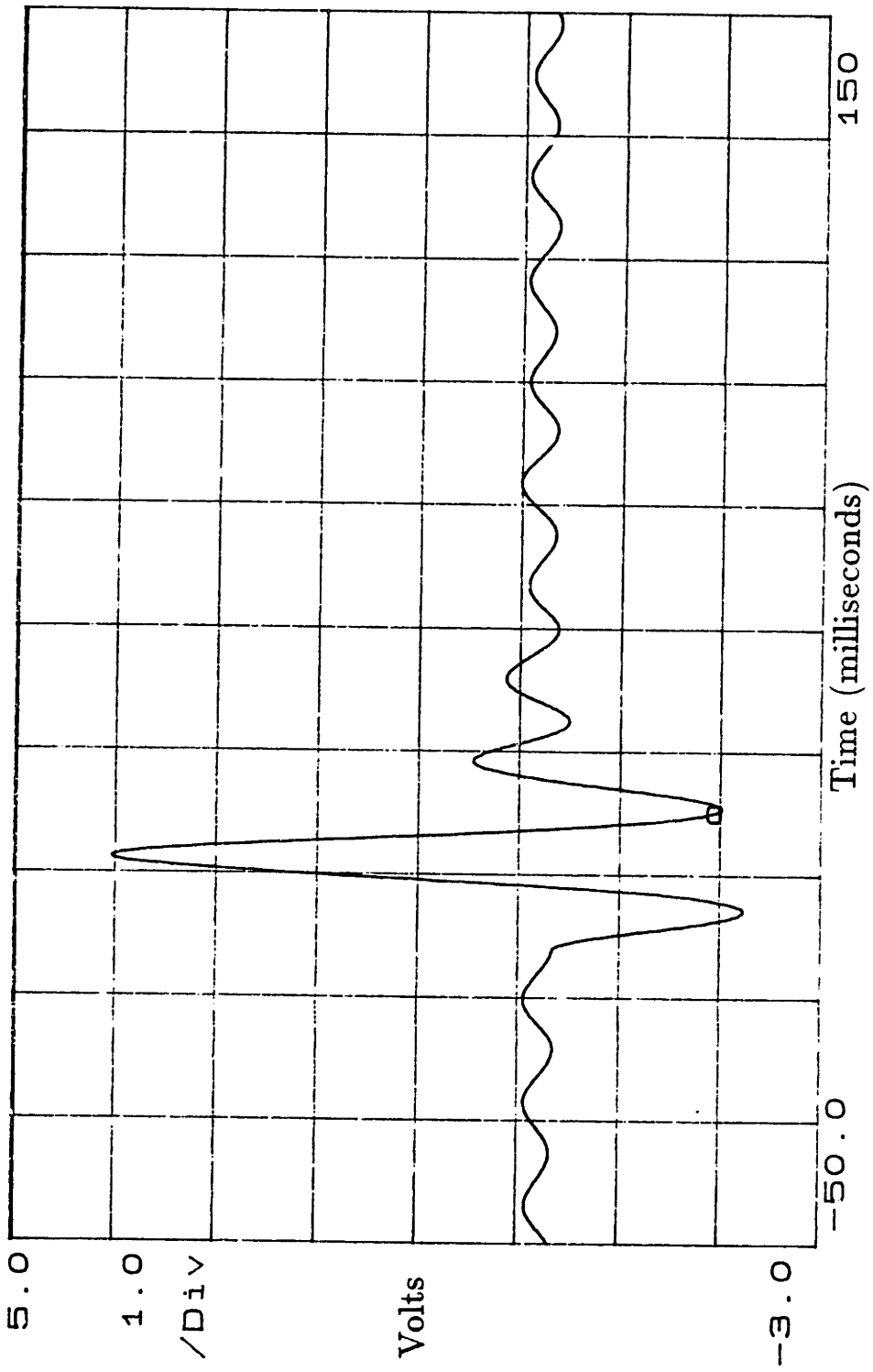

Figure 3.6: Scaled rotational motion of the HDA obtained by subtracting the output of the inductive position sensors Y1 and Y2.

This type of testing, however, was limited by the chosen rigid mounting location, Y1,Y2, and X1, of the inductive position sensors.

On the other hand, accelerometers were easily placed at any accessible mounting location for testing of drive frequency response or acceleration. Acceleration testing was useful in determining the existence of cross-coupling between orthogonal motion in the HDA/shock mount system.

In testing the drive, preliminary experiments indicated a strong possibility of cross-coupling between both translational and rotational motion in the plane of the disks and also possible coupling between horizontal and vertical motion. However, a more complete analysis was required to verify these possibilities.

Modal Analysis

To fully understand the HDA/shock mount dynamics, modal analysis was performed. This type of testing was more involved, but it provided insight into the higher order modes of vibration of the HDA and potential cross-coupling in the system.

First, forty-two evenly spaced test points were chosen on the accessible portion of the HDA. A three dimensional mesh of the test points is shown in Figure 3.7. The set of points represents the upper half of the HDA, as the lower half of the HDA was inaccessible due to the HDA supporting frame. An accelerometer was then placed along one of the coordinate axis (X, Y, or Z) at an arbitrary test point, after which ten impulses were applied by the impact hammer at each of the forty-two test points. A frequency response was calculated between each impact test point

and each accelerometer location and evaluated using the Hewlett Packard 3566A Dynamic Signal Analyzer. Each set of ten impacts was then averaged to get a clear representation of the frequency response from the test point to the accelerometer. After completing the tests, the accelerometer was moved to one of the remaining axis (X, Y, or Z) and the tests were repeated, and so on.

The STARModal software combined each of the sets of data to produce a three dimensional animated view of the modes of vibration. Figure 3.8 shows snapshots of a rotational mode of the HDA as represented by the STARModal software.

The STARModal software animation results clearly show the predicted coupling between translational and rotational motion in the plane of the disk stack.

Also, the results verified the natural frequencies predicted through impact testing (35Hz translational, 75Hz rotational in the plane of the disks).

Finally, the STARModal software illustrated the spectral proximity of all higher order modes of HDA vibration. From the analysis, no substantial higher order modes of vibration exist below 500Hz. However, a significant rotational mode (in the plane of the disks) exists at approximately 540Hz and pronounced translational modes (in the plane of the disks) exist around 1700Hz.

However, the modal animation data inconclusively proved the existence of coupling between translational motion along the X or Y axis or rotation around the Z axis to motion along the Z axis or rotation around the X or Y axis.

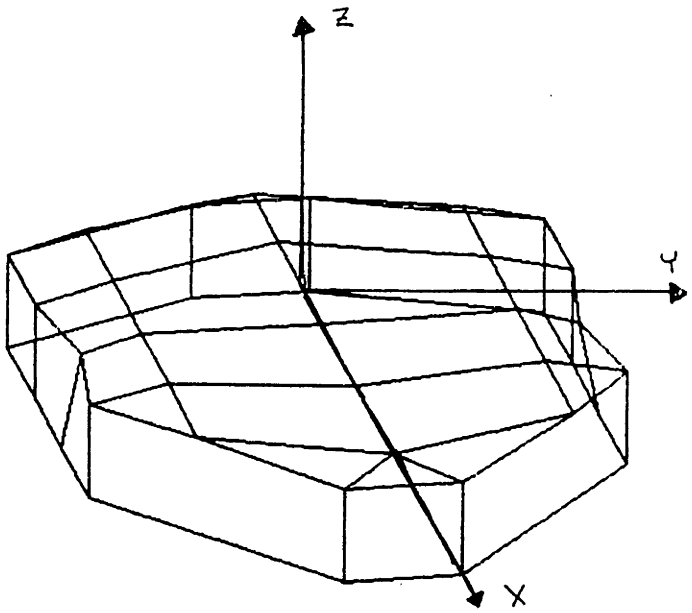

Figure 3.7: Three dimensional mesh of test points for modal analysis.

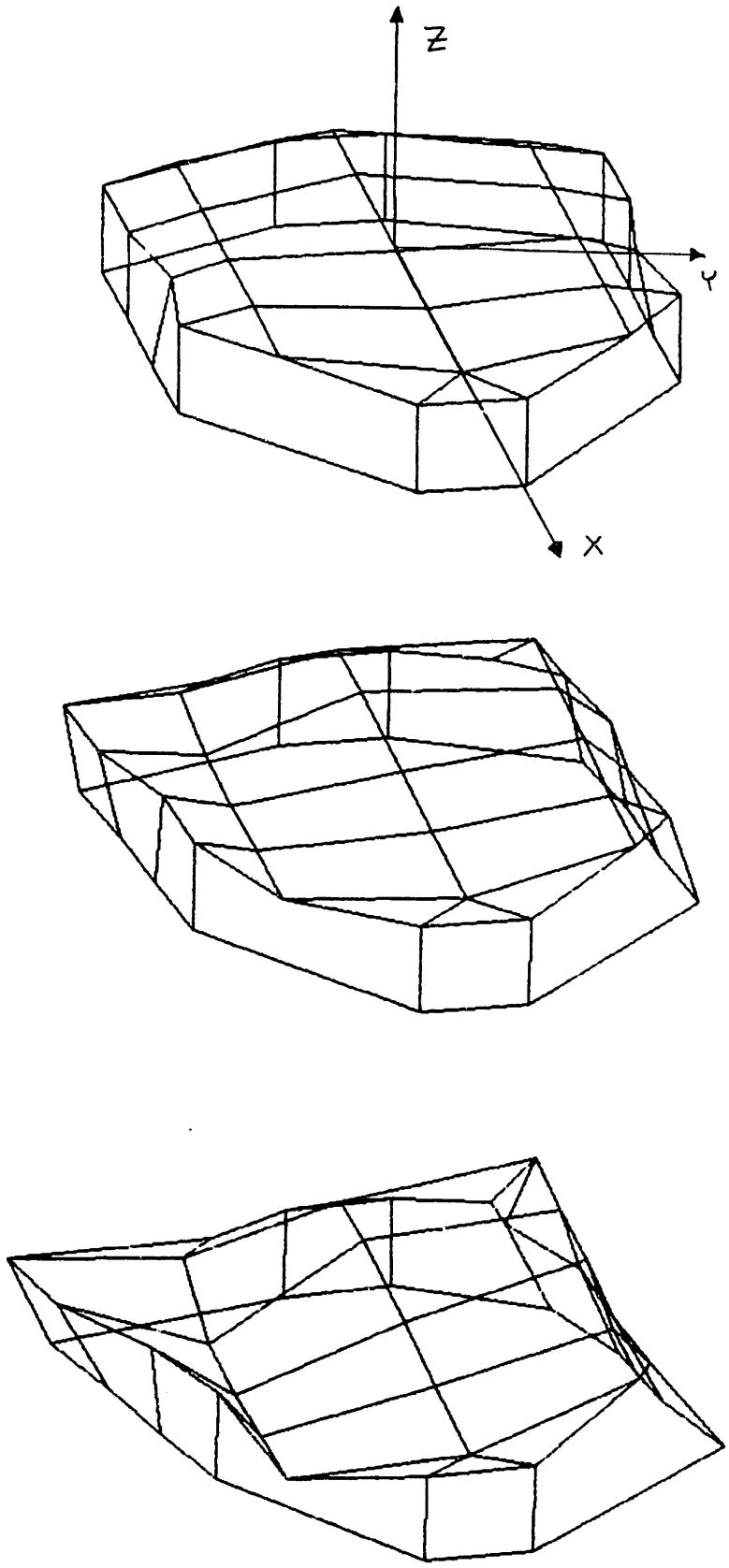

Figure 3.8: STARModal animated rotational motion of the HDA.

Shaker Table Analysis

To test for any unknown coupling, a shaker table was used. The shaker table provided a swept sine (10Hz to 200Hz) translational acceleration input to the drive supporting frame in the horizontal plane of the disks.

By comparing the magnitude of the translational acceleration of the supporting frame to the magnitude of the acceleration of the HDA in each of the 6 degrees of freedom (3 translational, 3 rotational), the existence of coupled motion could be determined.

The results indicated no substantial coupling between translational motion of the supporting frame in the horizontal plane of the disks to translational motion of the HDA in the Z direction or rotational motion of the HDA around the X axis or Y axis over an input frequency range from 10Hz to 200Hz.

The predicted coupling between rotation of the HDA around the Z axis to translational motion of the drive supporting frame (along the X and Y axis) was also verified.

Finally, it was found that small coupling exists between translational motion of the supporting frame and orthogonal translational motion of the HDA in the horizontal plane of the disks.

Drive Hardware Based Testing

A typical plot of track position error versus actuator motor current for a seek of 1300 disk tracks in length is shown in Figure 3.9. The track position error data is only useful once the read/write heads reach their destination track (A). Before this point, the heads passed over a large number of disk tracks during the seek operation, and the position error signal shows the position error of the read/write heads relative to the current disk track being crossed at each sampling instant.

3.4.3 Conclusions

Due to the planar coupling in the drive, the single-degree-of-freedom model developed in Section 3.3 is not sufficient to describe the motion of the HDA.

However, a six-degree-of-freedom model describing the motion of the HDA is unnecessary due to the non-existence of coupling from planar motion of the supporting frame in the horizontal plane of the disks to translational motion of the HDA along the Z axis or rotational motion of the HDA around the X axis or Y axis.

Therefore, a three-degree-of-freedom model describing the planar motion of the HDA is both necessary and sufficient to accurately predict the rigid body modes of the drive behavior.

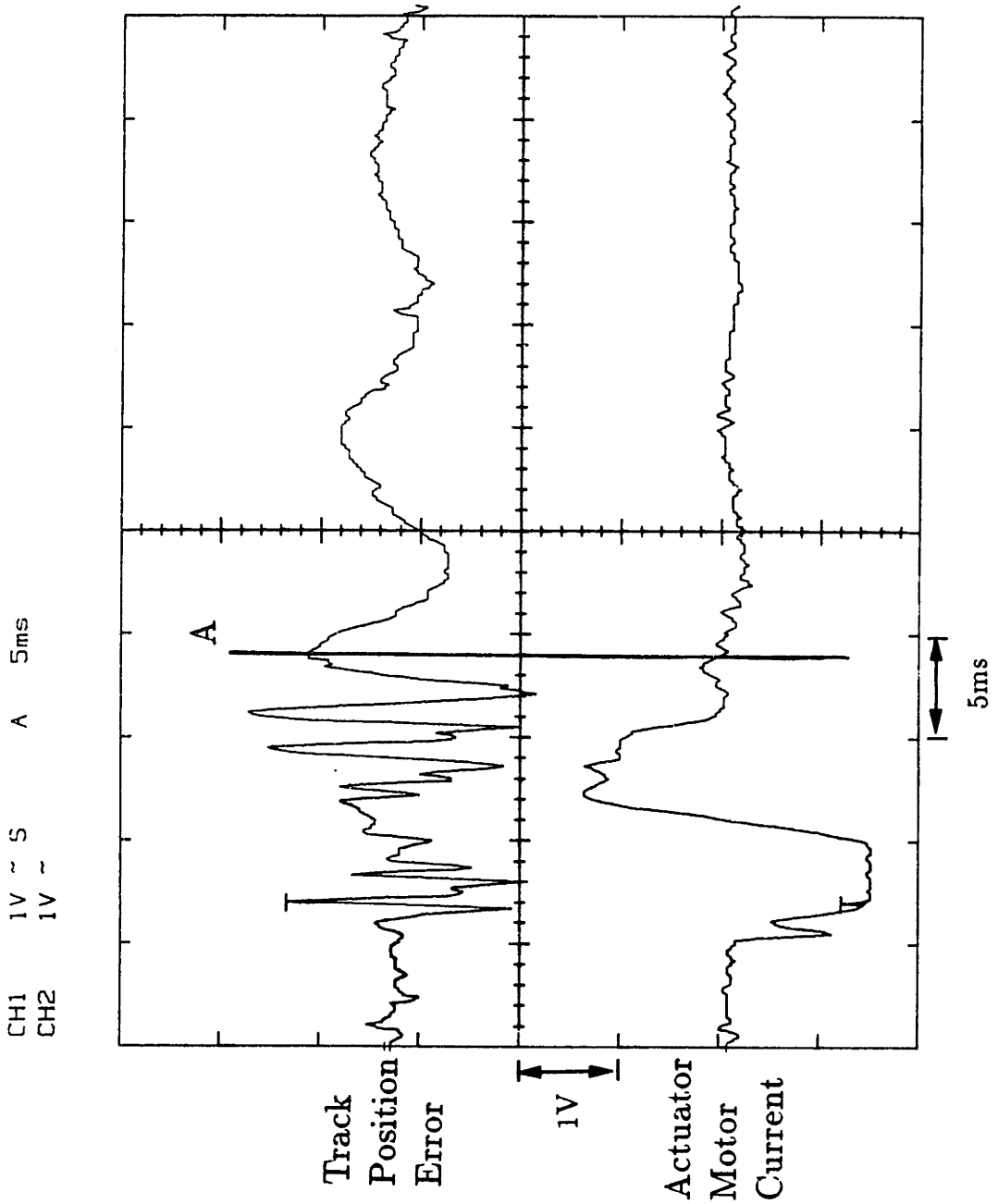

Figure 3.9: Typical track position error and actuator motor current for a 1300 track seek.

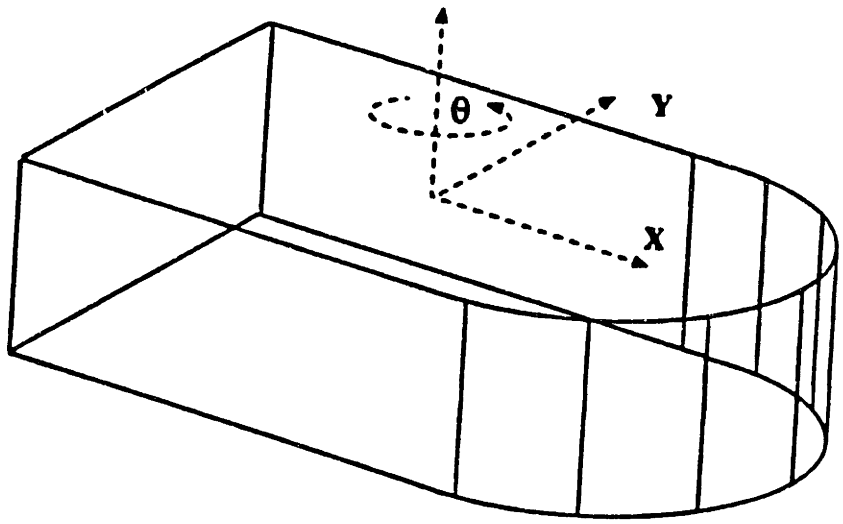

Figure 3.10: Model coordinate definition.

3.5 Three-Degree-of-Freedom Model

In this model, the HDA was assumed to behave as a rigid body undergoing planar motion where the exact position and orientation of the HDA were determined using both the translational and rotational coordinates (x, y, θ). The coordinate system was defined as fixed in inertial space at the center of the HDA in equilibrium as shown in Figure 3.10.

The dynamic model of the HDA was constructed in state-space form as shown below where [**M**] is the mass matrix, [**B**] is the damping matrix, [**K**] is the stiffness matrix, $\underline{\mathbf{X}}$ is the position vector, and $\underline{\mathbf{F}}$ is the vector of force inputs on the HDA.

$$[\mathbf{M}]\,\ddot{\underline{\mathbf{X}}} + [\mathbf{B}]\,\dot{\underline{\mathbf{X}}} + [\mathbf{K}]\,\underline{\mathbf{X}} = \underline{\mathbf{F}} \tag{3.4}$$

The position vector $\underline{\mathbf{X}}$ is described by:

$$\underline{\mathbf{X}} = \begin{bmatrix} X \\ Y \\ \theta \end{bmatrix} \tag{3.5}$$

The mass matrix is given by:

$$[\mathbf{M}] = \begin{bmatrix} m_{xx} & m_{xy} & m_{x\theta} \\ m_{yx} & m_{yy} & m_{y\theta} \\ m_{\theta x} & m_{\theta y} & m_{\theta\theta} \end{bmatrix} \tag{3.6}$$

The damping matrix is given by:

$$[\mathbf{B}] = \begin{bmatrix} b_{xx} & b_{xy} & b_{x\theta} \\ b_{yx} & b_{yy} & b_{y\theta} \\ b_{\theta x} & b_{\theta y} & b_{\theta\theta} \end{bmatrix} \tag{3.7}$$

The stiffness matrix is given by:

$$[\mathbf{K}] = \begin{bmatrix} k_{xx} & k_{xy} & k_{x\theta} \\ k_{yx} & k_{yy} & k_{y\theta} \\ k_{\theta x} & k_{\theta y} & k_{\theta\theta} \end{bmatrix} \tag{3.8}$$

The following sections describe how the individual parameters in the above model were derived and verified.

3.5.1 Mass Matrix

To simplify the mass matrix, the first two diagonal terms, m_{xx} and m_{yy}, were assumed to be the mass of the test drive HDA, m, including the circuit board (2.54 kg). The third diagonal term, $m_{\theta\theta}$, was assumed to be the moment of inertia of the HDA, I, about the point of rotation. This value was approximated to be $9.34 \cdot 10^{-4} Kg\ m^2$ from design specifications. The off-diagonal terms in the mass matrix show dynamic coupling in the system. No dynamic coupling was assumed between the two translational directions, X and Y. However, due to the offset center of mass of the HDA from the center of rotation of the shock mount system, r, an approximation to the dynamic coupling between translational and rotational motion could be given as the mass of the HDA times the radial offset of the center of mass. In the test drive, the center of mass offset, r, is approximately 5mm in both the X and Y directions (from design specs). The values for $m_{x\theta}$, $m_{y\theta}$, $m_{\theta x}$, and $m_{\theta y}$ were approximated by $-m \cdot r = -2.54kg \cdot 0.005m$. The mass matrix can therefore be simplified as:

$$[\mathrm{M}] = \begin{bmatrix} m & 0 & -mr \\ 0 & m & -mr \\ -mr & -mr & I \end{bmatrix} = \begin{bmatrix} 2.54 & 0 & -1.27 \cdot 10^{-2} \\ 0 & 2.54 & -1.27 \cdot 10^{-2} \\ -1.27 \cdot 10^{-2} & -1.27 \cdot 10^{-2} & 9.34 \cdot 10^{-4} \end{bmatrix} \quad (3.9)$$

3.5.2 Damping Matrix

The diagonal terms of the damping matrix contain information concerning the natural frequency of the system, the damping ratio of the system, and the amount of cross-

coupling between damping components in each of the three coordinate directions. These terms can be approximated as follows:

$$b_{xx} = 2\zeta_x \omega_x m \tag{3.10}$$

$$b_{yy} = 2\zeta_y \omega_y m \tag{3.11}$$

$$b_{\theta\theta} = 2\zeta_\theta \omega_\theta I \tag{3.12}$$

where ζ_x, ζ_y, ζ_θ are the damping ratios for a response in the X, Y, θ directions respectively, and ω_x, ω_y, ω_θ are the natural frequencies of the system in the X, Y, θ directions respectively.

For translational motion in both the X and Y directions, ζ_x and ζ_y were found to be approximately $(0.2\ \frac{Kg}{s})$, as discussed in Section 3.4.2. For rotational motion, ζ_θ was estimated at $(0.225\ \frac{Kg}{s})$.

To derive the system's natural frequencies, $\omega_x, \omega_y, \omega_\theta$, the damped natural frequencies, $\omega_{xd}, \omega_{yd}, \omega_{\theta d}$, were found through impact testing as discussed in Section 3.4.2. The natural frequency was then derived from the damped natural frequency using the following formulas [9]:

$$\omega_x = \omega_{xd} \frac{1}{\sqrt{1-\zeta_x^2}} \tag{3.13}$$

$$\omega_y = \omega_{yd} \frac{1}{\sqrt{1-\zeta_y^2}} \tag{3.14}$$

$$\omega_\theta = \omega_{\theta d} \frac{1}{\sqrt{1-\zeta_\theta^2}} \tag{3.15}$$

Due to the orientation of the shock mounts, the translational damped natural frequency differed slightly (1-2Hz) between the X and Y directions. However, to simplify the model, an average value of 35Hz was used for motion in both directions. The damped natural frequency for rotational motion was determined to be 75Hz. These values were verified from the modal analysis results.

As determined from shaker table analysis, coupling existed between translational motion (X and Y) in the horizontal plane of the disks. Assuming this coupling was due to the shock mounts (damping/stiffness characteristics), a coupling factor, c_f, was found and included in the damping and stiffness matrices to scale the magnitude of the translational output orthogonal to the translational input. For the test drive, this value was derived by comparing the measured frequency responses of the system as shown below:

$$\frac{Y_{out}}{X_{in}} = c_f \frac{X_{out}}{X_{in}} \tag{3.16}$$

where X_{in} is the measured translational acceleration of the supporting frame, X_{out} is the measured translational acceleration of the HDA along the same axis as the input, and Y_{out} is the measured translational acceleration of the HDA orthogonal to the input.

As a simple approximation, the off-diagonal terms, b_{xy} and b_{yx}, are equal to the

coupling factor, c_f, times the diagonal value, b_{xx}. For the test drive, the value c_f = 0.05.

To further simplify the model, cross coupling in the damping matrix between translational and rotational motion was assumed to be insignificant and approximately equal to zero.

The damping matrix [**B**] in $\frac{Kg}{s}$ can then be summarized as:

$$[\mathbf{B}] = \begin{bmatrix} 2\zeta_x\omega_x m & -c_f 2\zeta_x\omega_x m & 0 \\ -c_f 2\zeta_x\omega_x m & 2\zeta_y\omega_y m & 0 \\ 0 & 0 & 2\zeta_\theta\omega_\theta I \end{bmatrix} = \begin{bmatrix} 223.4 & -11.17 & 0 \\ -11.17 & 223.4 & 0 \\ 0 & 0 & 0.198 \end{bmatrix} \quad (3.17)$$

3.5.3 Stiffness Matrix

The diagonal terms in the stiffness matrix, k_{xx}, k_{yy}, and $k_{\theta\theta}$, were calculated using the following general formulas:

$$k_{xx} = \omega_x^2 m \quad (3.18)$$

$$k_{yy} = \omega_y^2 m \quad (3.19)$$

$$k_{\theta\theta} = \omega_\theta^2 I \quad (3.20)$$

The off-diagonal coupling terms, k_{xy} and k_{yx}, were approximated using the identical coupling factor, c_f, found in the damping matrix as shown in the formula below:

$$k_{xy} = k_{yx} = -c_f k_{xx} \tag{3.21}$$

Again, no coupling was assumed in this matrix between the translational and rotational motion.

The stiffness matrix [K] in $\frac{Kg}{s^2}$ can then be summarized as:

$$[\mathbf{K}] = \begin{bmatrix} \omega_x^2 m & -c_f \omega_x^2 m & 0 \\ -c_f \omega_x^2 m & \omega_y^2 m & 0 \\ 0 & 0 & \omega_\theta^2 I \end{bmatrix} = \begin{bmatrix} 1.228 \cdot 10^5 & -6.14 \cdot 10^3 & 0 \\ -6.14 \cdot 10^3 & 1.228 \cdot 10^5 & 0 \\ 0 & 0 & 207.41 \end{bmatrix} \tag{3.22}$$

Note: the terms in the [K] matrix have units of $\frac{Kg}{s^2}$.

3.5.4 Force Input Matrix

The force input matrix is simply a vector showing both the type and distribution of the inputs internal to the shock mounts. These inputs could take the form of actuator seeks or direct impacts to the HDA. The force input vector is shown below.

$$\underline{\mathbf{F}} = \begin{bmatrix} F_x \\ F_y \\ \tau_\theta \end{bmatrix} \tag{3.23}$$

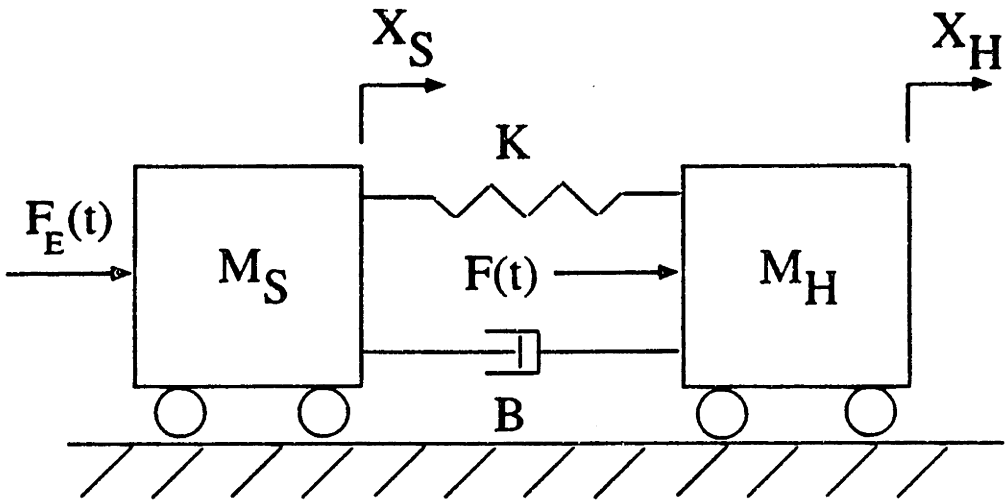

Figure 3.11: Expanded model of HDA.

3.6 Expanded Model for External Inputs

Previously, the external supporting frame in which the HDA is mounted was assumed to be fixed in inertial space. However, this in reality is not the case. During actual drive operation, the supporting frame undergoes translational and rotational acceleration.

To explain this behavior, the model was expanded as shown by the simple 2 degree-of-freedom model in Figure 3.11, where M_H is the mass of the HDA, X_H is the position of the HDA, K and B are the stiffness and damping of the shock mounts, M_S is the mass of the external structure including the drive supporting frame, X_S is the position of the external structure, $F_E(t)$ is the force input to the external structure, and $F(t)$ is the force input to the HDA.

Deriving the state-space equations of motion for the HDA gives:

$$M_H\ddot{X}_H + B(\dot{X}_H - \dot{X}_S) + K(X_H - X_S) = F(t) \tag{3.24}$$

or, by manipulation of the terms,

$$\ddot{X}_H + \frac{B}{M_H}\dot{X}_H + \frac{K}{M_H}X_H = \frac{B}{M_H}\dot{X}_S + \frac{K}{M_H}X_S + \frac{F(t)}{M_H} \tag{3.25}$$

Generalizing this two degree-of-freedom model to include motion in six degrees of freedom, and substituting the previously determined 3x3 mass matrix, [**M**], for M_H, the 3x3 damping matrix, [**B**], for B, the 3x3 stiffness matrix [**K**] for K, and the force input matrix $\underline{\mathbf{F}}$ for $F(t)$ as $\underline{\mathbf{F_H}}$ gives:

$$\underline{\ddot{\mathbf{X}}_\mathbf{H}} + [\mathbf{M}]^{-1}[\mathbf{B}]\underline{\dot{\mathbf{X}}_\mathbf{H}} + [\mathbf{M}]^{-1}[\mathbf{K}]\underline{\mathbf{X}_\mathbf{H}} = [\mathbf{M}]^{-1}[\mathbf{B}]\underline{\dot{\mathbf{X}}_\mathbf{S}} + [\mathbf{M}]^{-1}[\mathbf{K}]\underline{\mathbf{X}_\mathbf{S}} + [\mathbf{M}]^{-1}\underline{\mathbf{F}_\mathbf{H}} \tag{3.26}$$

and, adding by identity:

$$\begin{bmatrix} \underline{\ddot{\mathbf{X}}_\mathbf{S}} \\ \underline{\dot{\mathbf{X}}_\mathbf{S}} \end{bmatrix} = \begin{bmatrix} \mathbf{0} & \mathbf{0} \\ \mathbf{I} & \mathbf{0} \end{bmatrix} \begin{bmatrix} \underline{\dot{\mathbf{X}}_\mathbf{S}} \\ \underline{\mathbf{X}_\mathbf{S}} \end{bmatrix} + \begin{bmatrix} \mathbf{I} & \mathbf{0} \\ \mathbf{0} & \mathbf{0} \end{bmatrix} \begin{bmatrix} \underline{\ddot{\mathbf{X}}_\mathbf{S}} \\ \underline{\mathbf{F}_\mathbf{H}} \end{bmatrix} \tag{3.27}$$

Rearranging the above equations and placing them into a system matrix format gives:

$$\begin{bmatrix} \underline{\ddot{\mathbf{X}}_\mathbf{H}} \\ \underline{\dot{\mathbf{X}}_\mathbf{H}} \\ \underline{\ddot{\mathbf{X}}_\mathbf{S}} \\ \underline{\dot{\mathbf{X}}_\mathbf{S}} \end{bmatrix} = \begin{bmatrix} -[\mathbf{M}]^{-1}[\mathbf{B}] & -[\mathbf{M}]^{-1}[\mathbf{K}] & [\mathbf{M}]^{-1}[\mathbf{B}] & [\mathbf{M}]^{-1}[\mathbf{K}] \\ [\mathbf{I}] & [\mathbf{0}] & [\mathbf{0}] & [\mathbf{0}] \\ [\mathbf{0}] & [\mathbf{0}] & [\mathbf{0}] & [\mathbf{0}] \\ [\mathbf{0}] & [\mathbf{0}] & [\mathbf{I}] & [\mathbf{0}] \end{bmatrix} \begin{bmatrix} \underline{\dot{\mathbf{X}}_\mathbf{H}} \\ \underline{\mathbf{X}_\mathbf{H}} \\ \underline{\dot{\mathbf{X}}_\mathbf{S}} \\ \underline{\mathbf{X}_\mathbf{S}} \end{bmatrix} \tag{3.28}$$

$$+\begin{bmatrix} [0] & [M^{-1}] \\ [0] & [0] \\ [I] & [0] \\ [0] & [0] \end{bmatrix} \begin{bmatrix} \ddot{\underline{X}}_S \\ \underline{F_H} \end{bmatrix} \tag{3.29}$$

and the output equation has the form:

$$\underline{Y} = \begin{bmatrix} -[M]^{-1}[B] & -[M]^{-1}[K] & [M]^{-1}[B] & [M]^{-1}[K] \end{bmatrix} \begin{bmatrix} \dot{\underline{X}}_H \\ \underline{X_H} \\ \dot{\underline{X}}_S \\ \underline{X_S} \end{bmatrix} \tag{3.30}$$

$$+\begin{bmatrix} [0] & [M]^{-1} \end{bmatrix} \begin{bmatrix} \ddot{\underline{X}}_S \\ \underline{F_H} \end{bmatrix} \tag{3.31}$$

where the outputs $\underline{Y}$ are defined as,

$$\underline{Y} = \begin{bmatrix} \ddot{X}_H \\ \ddot{Y}_H \\ \ddot{\theta}_H \end{bmatrix} \tag{3.32}$$

The motion of the HDA $\underline{X_H}$ is described by:

$$\underline{\mathbf{X_H}} = \begin{bmatrix} X_H \\ Y_H \\ \theta_H \end{bmatrix} \tag{3.33}$$

The motion of the external structure $\underline{\mathbf{X_S}}$ is described by:

$$\underline{\mathbf{X_S}} = \begin{bmatrix} X_S \\ Y_S \\ \theta_S \end{bmatrix} \tag{3.34}$$

The Force Input Matrix $\underline{\mathbf{F_H}}$ describing inputs internal to the shock mounts is given by:

$$\underline{\mathbf{F_H}} = \begin{bmatrix} F_x \\ F_y \\ \tau_\theta \end{bmatrix} \tag{3.35}$$

[I] is a 3x3 identity matrix, and $[\mathbf{M}]^{-1}$ is the inverse of the mass matrix.

By placing the model in this format, external inputs could be characterized based on the acceleration imposed on the supporting frame without knowledge of the mass or moment of inertia of the supporting frame.

3.6.1 HDA Transfer Function Matrix

Based on the model, a transfer function matrix can be created to describe each of the three outputs based on each of the six individual inputs such that:

$$\underline{\mathbf{Y}} = [\mathbf{T}]\,\underline{\mathbf{X}} \tag{3.36}$$

where:

$$[\mathbf{T}] = \begin{bmatrix} T_{11} & T_{12} & T_{13} & T_{14} & T_{15} & T_{16} \\ T_{21} & T_{22} & T_{23} & T_{24} & T_{25} & T_{26} \\ T_{31} & T_{32} & T_{33} & T_{34} & T_{35} & T_{36} \end{bmatrix} \tag{3.37}$$

The numerical values of the individual elements of the [T] matrix are found in Appendix B.

3.7 Six-Degree-of-Freedom Model Evaluation

The following sections show the results of the laboratory verification of the six-degree-of-freedom model through simulated actuator seeks and shaker table analysis.

3.7.1 Simulated Actuator Seeks

A typical idealized model of the actuator motor current input profile is shown in Figure 3.12, set to arbitrary magnitude of 1. The actuator motor current is directly proportional to the torque applied by the actuator. This profile represents a typical 14ms seek for the test drive. As discussed in Section 1.1, a seek is defined as the

operation of moving the read/write heads from one disk track to another. Therefore, a 14ms seek is a seek operation taking 14ms to complete.

Figure 3.13 shows the modeled angular position of the HDA due to the modeled actuator motor current input profile, assuming a motor torque constant of 1. The actual measured angular position of the HDA with respect to inertial space (as measured using the inductive position sensors) is shown in Figure 3.14. The seek chosen for comparison was 1300 tracks in length, taking approximately 14ms to complete.

As can be seen from the figure, the shape and damping of the predicted response very closely resembled the measured response. The magnitude discrepancies of the second period were most likely due to a slight difference in input profile and time length.

3.7.2 Experimental Verification of Model

To further evaluate the expanded model, a shaker table was used. In this analysis, the HDA was excited with a swept sine translational acceleration input to the supporting frame over a frequency range from 20Hz - 110Hz. A frequency response, magnitude and phase, was then calculated using the HP3562A Dynamic Signal Analyzer by comparing the measured acceleration of the HDA ($\ddot{X}_{hda}, \ddot{Y}_{hda}, \ddot{\theta}_{hda}$) to the measured acceleration of the supporting frame ($\ddot{X}_s$) across the frequency range. The measured frequency response was then compared to a modeled frequency response generated using the MATRIXx software package and the expanded model developed previously.

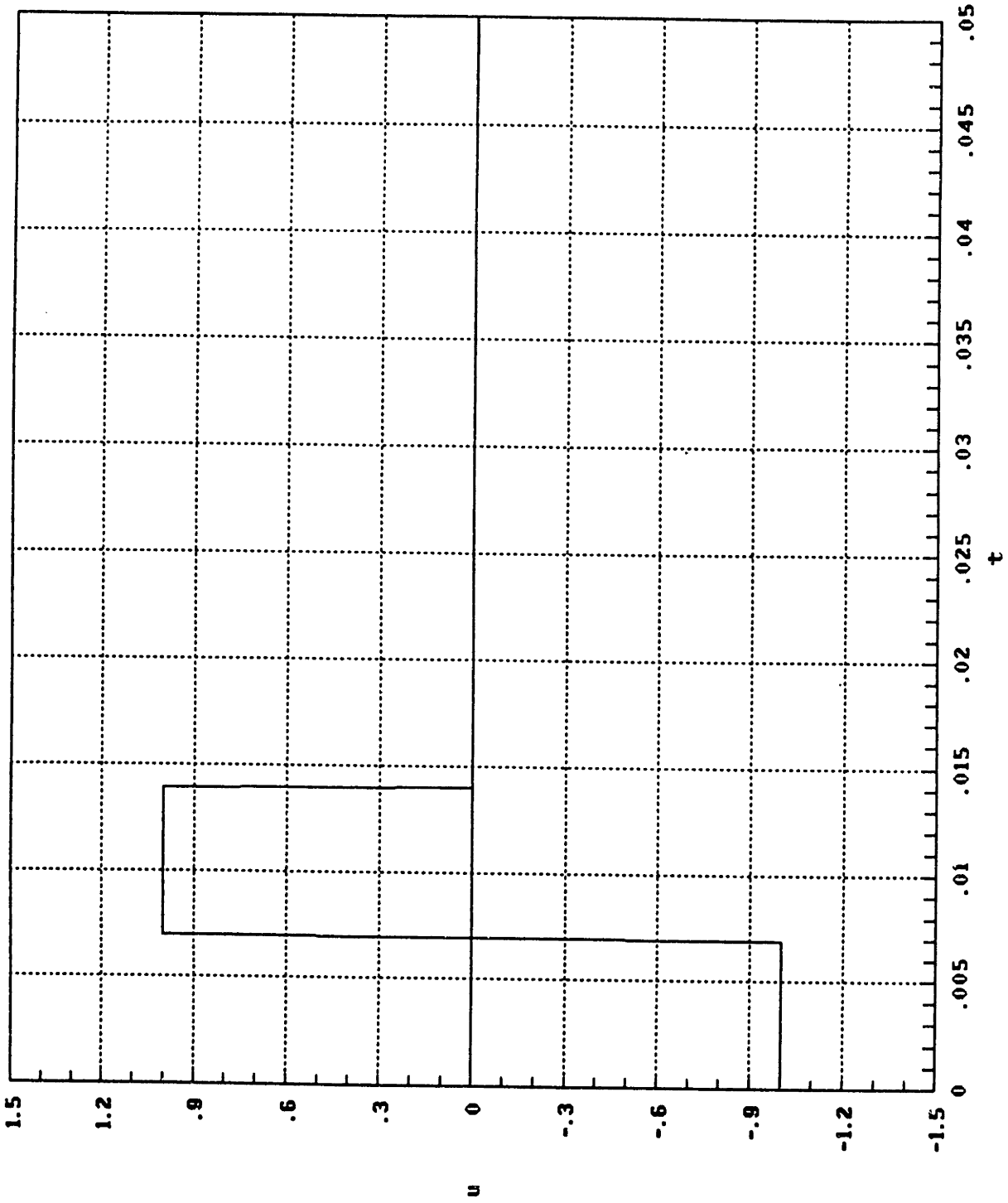

Figure 3.12: Model of actuator motor current input for a 14ms seek.

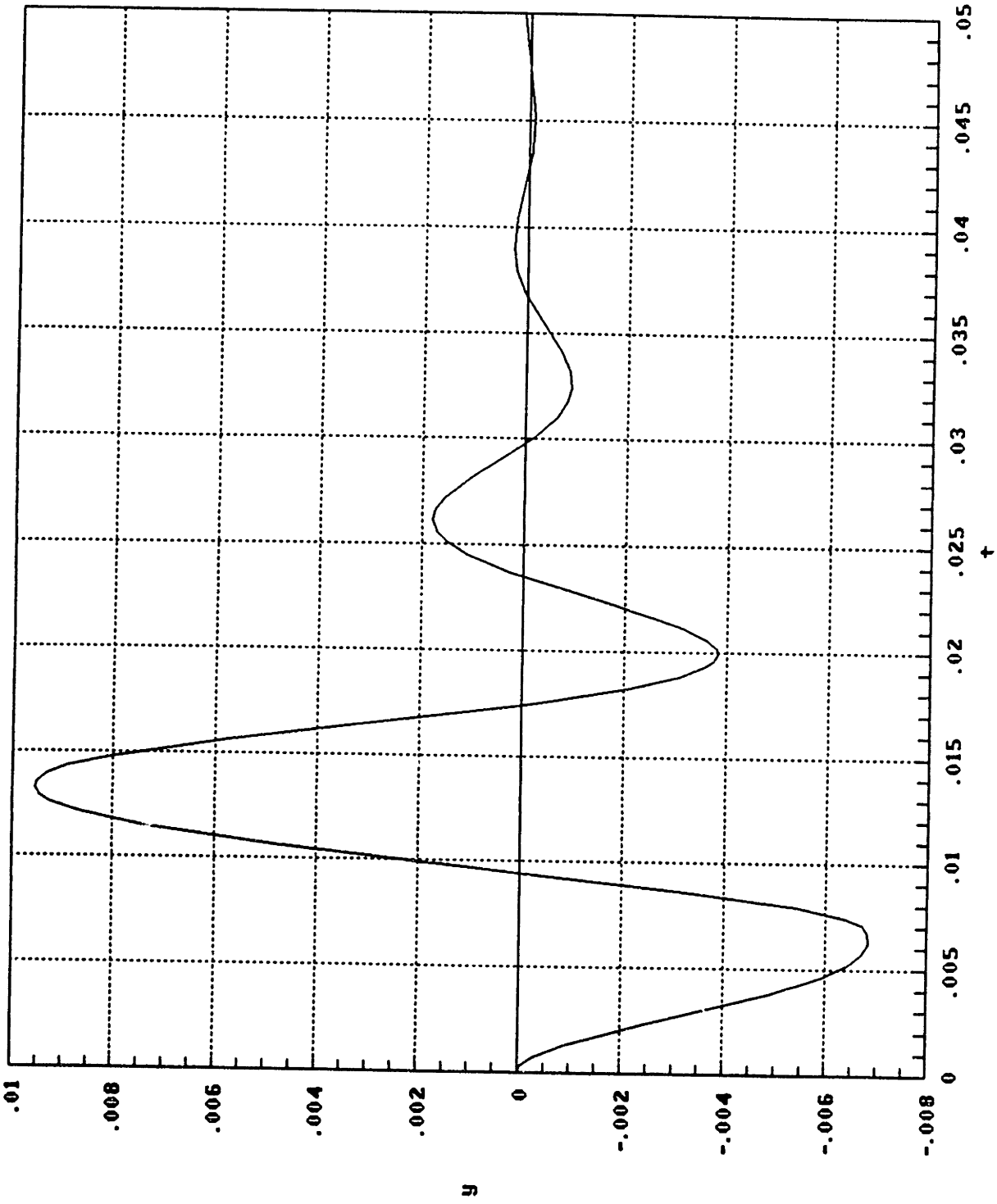

Figure 3.13: Simulated HDA angular position due to modeled actuator motor current input (14ms seek).

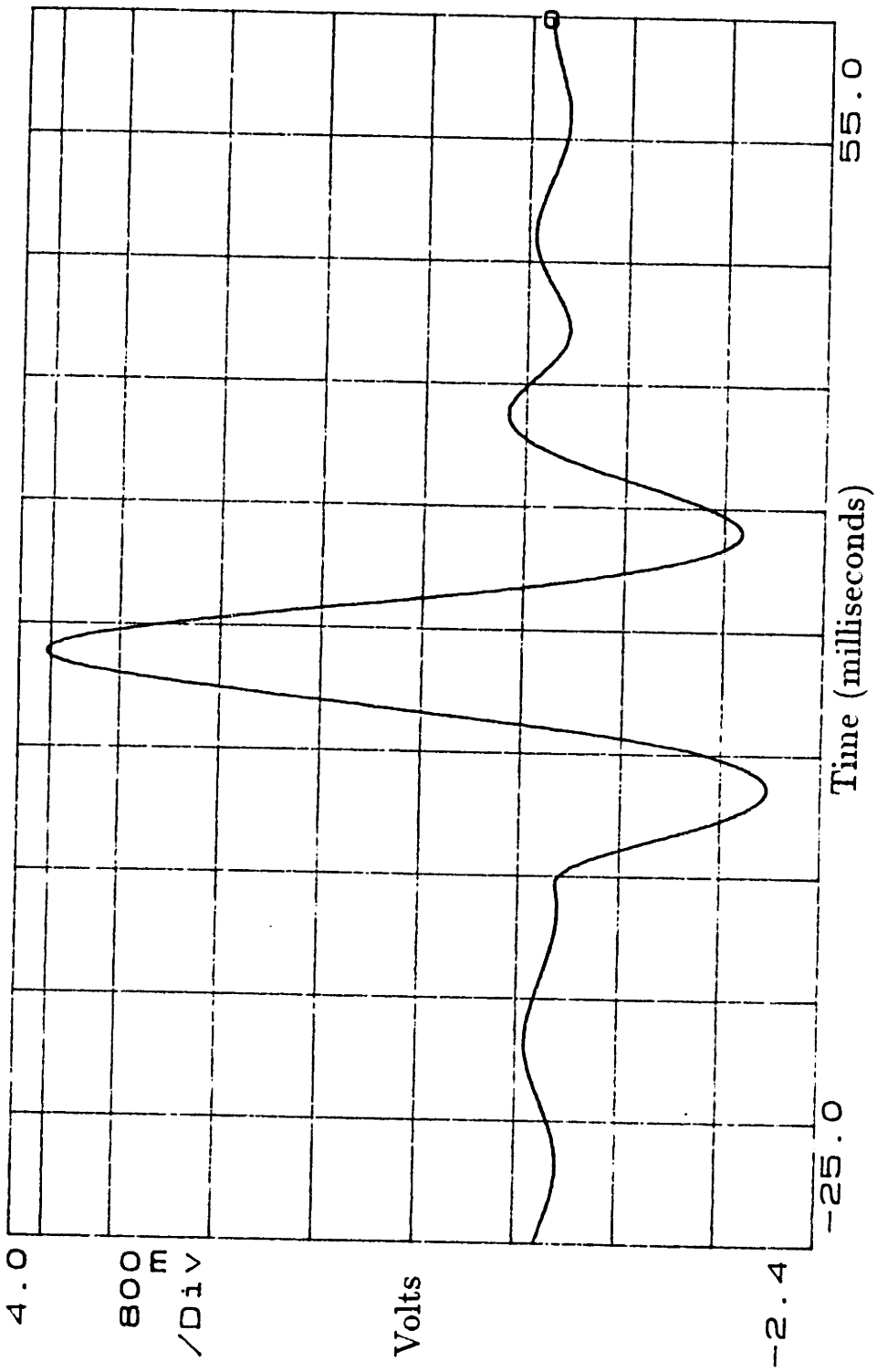

Figure 3.14: Measured rotational position of the HDA during a 1300 track seek.

Figure 3.15 shows the modeled frequency response of the system from a translational acceleration input to the supporting frame, $\ddot{X}_s$, to a translational acceleration of the HDA along the same axis, $\ddot{X}_{hda}$. Figure 3.16 shows the measured frequency response of the system. In comparison, both magnitude plots have a resonance peak of approximately 11dB at 33Hz with approximately the same slope across the frequency range. Similarly, the modeled phase closely resembled the measured phase.

Figure 3.17 shows the modeled frequency response of the system from a translational acceleration input to the supporting frame, $\ddot{X}_s$, to an orthogonal translational acceleration of the HDA, $\ddot{Y}_{hda}$. Figure 3.18 and Figure 3.19 show the measured frequency response of the system. Figure 3.19 explains the strange behavior of the measurement above 80Hz by illustrating the incoherence in the measurement. This incoherence was due to the small magnitude of the output at this frequency. In the comparison of the modeled response to the measured response, the magnitudes closely resembled one another except in the range where measurement coherence was lost. Similarly, the modeled phase also closely resembled the measured phase except in this range.

Figure 3.20 shows the modeled frequency response of the system from a translational acceleration input to the supporting frame, $\ddot{X}_s$, to an angular acceleration of the HDA, $\ddot{\theta}_{hda}$. The actual angular acceleration of the HDA was measured using two opposing linear accelerometers. Based on the distance between the two opposing linear accelerometers, a scaled rotation of the actual output was measured. In the

measurement, this distance was 5cm. Therefore, the measured acceleration equals $(0.05 \cdot \ddot{\theta})$. Figure 3.21 shows the measured frequency response. In comparison, both plots have magnitude peaks around 35Hz and 75Hz with nearly identical slopes across the frequency range. Also, the predicted phase closely resembled the measured phase of the system.

3.8 Conclusions

Based on the experimental results, the twelfth order model satisfactorily explains the rigid body planar behavior of the drive.

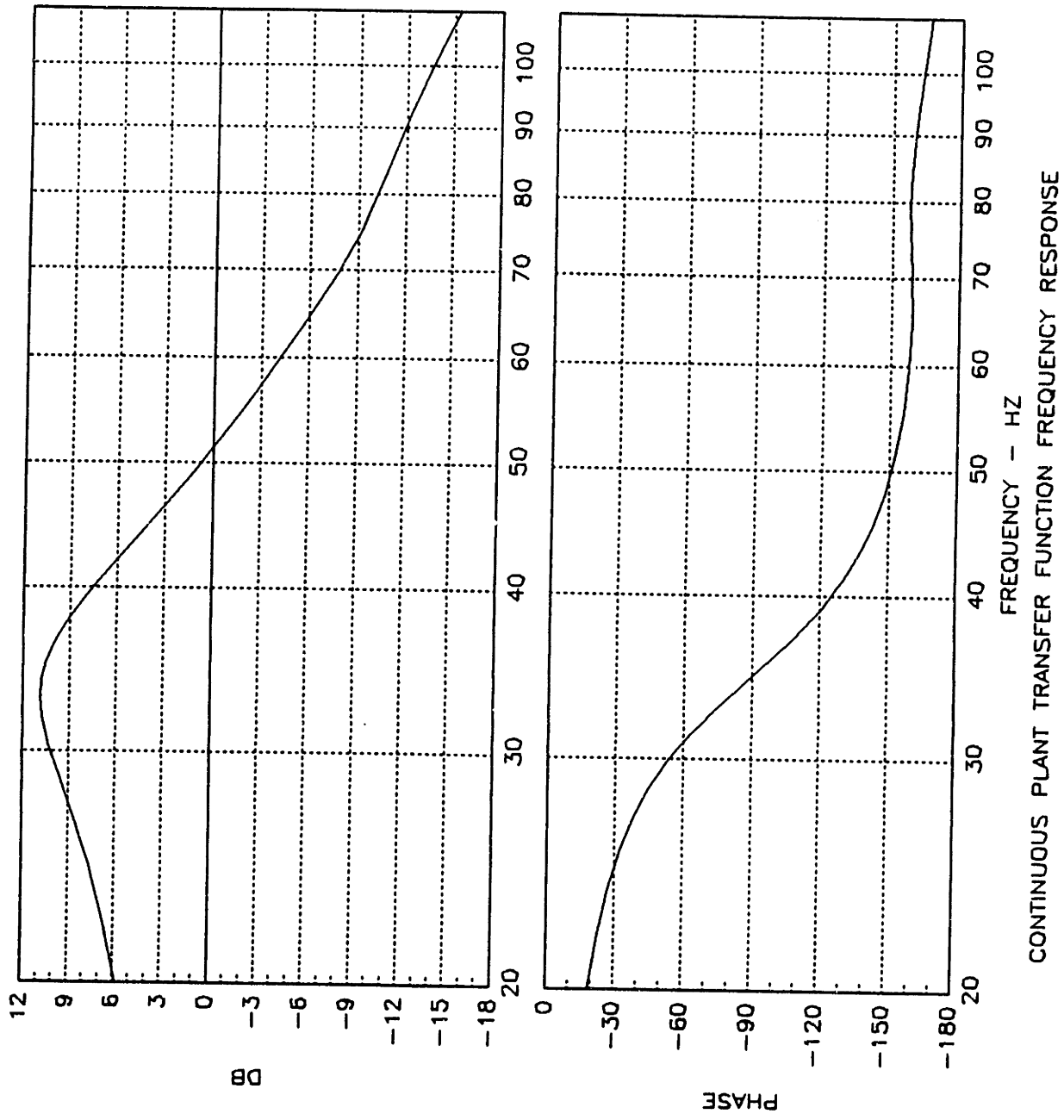

Figure 3.15: Modeled frequency response of the system from a translational acceleration of the supporting frame to a translational acceleration of the HDA (output along same axis as input).

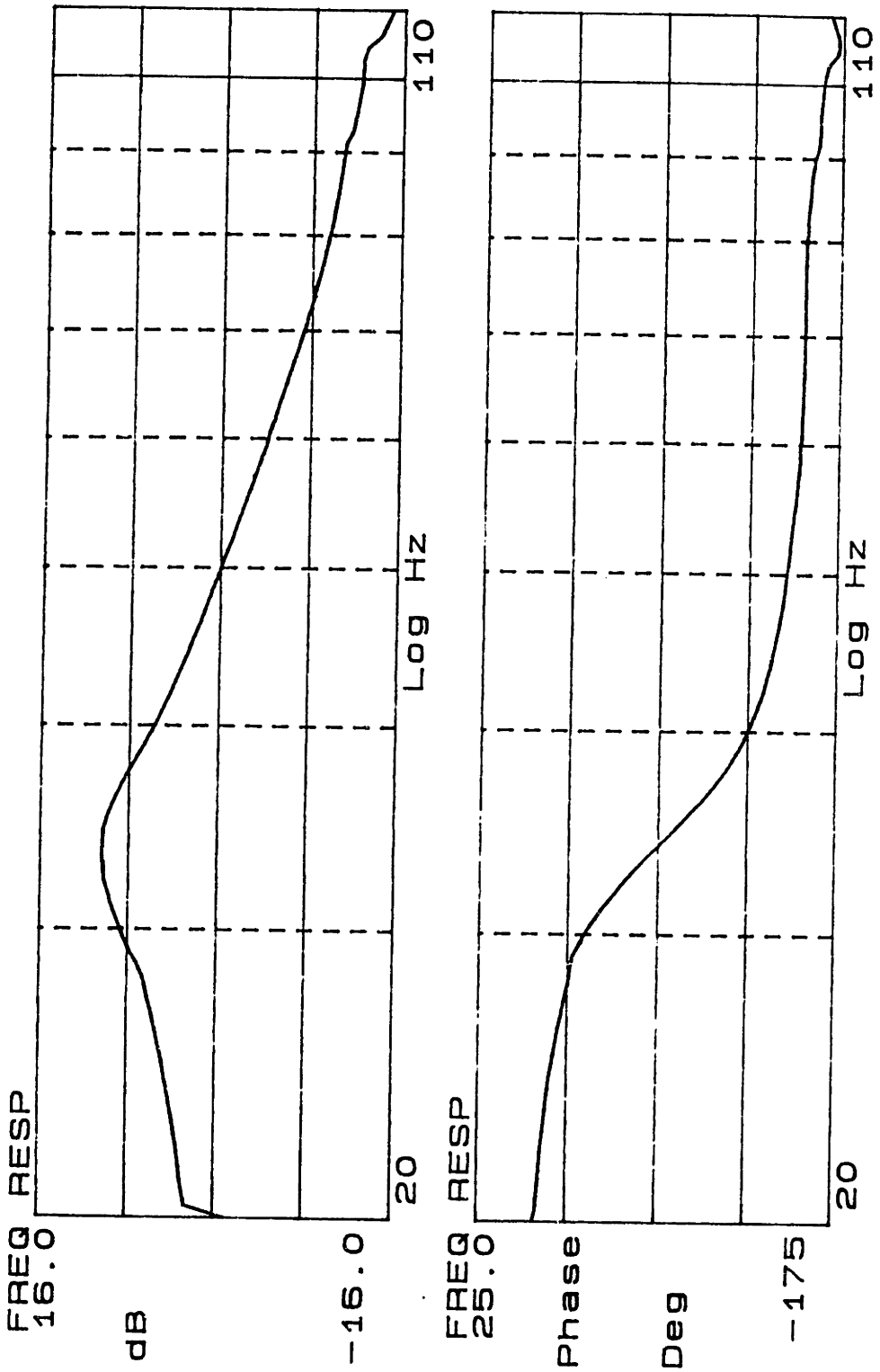

Figure 3.16: Measured frequency response of the system from a translational acceleration of the supporting frame to a translational acceleration of the HDA (output measured along same axis as input).

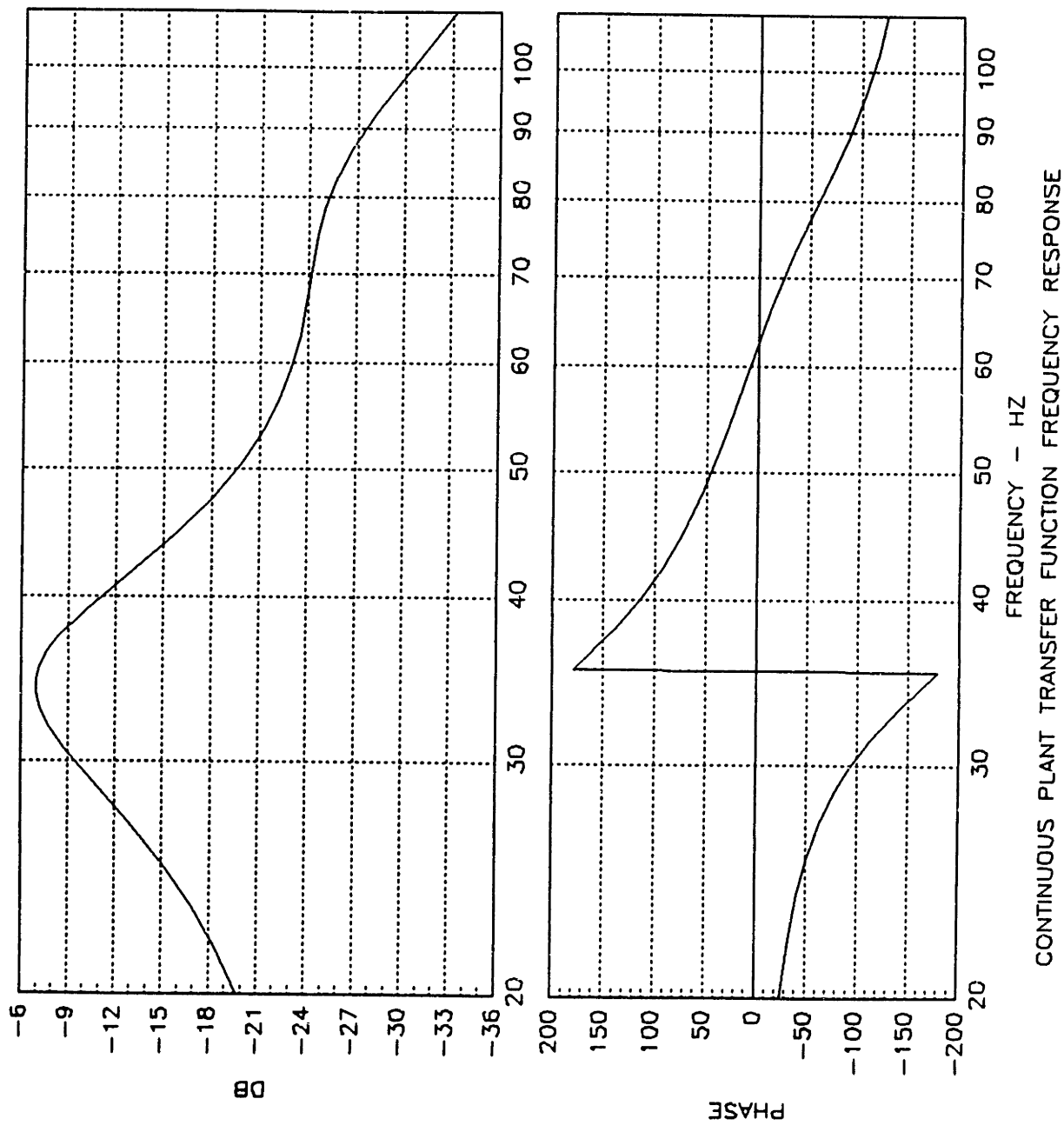

Figure 3.17: Modeled frequency response of the system from a translational acceleration of the supporting frame to a translational acceleration of the HDA (output orthogonal to input).

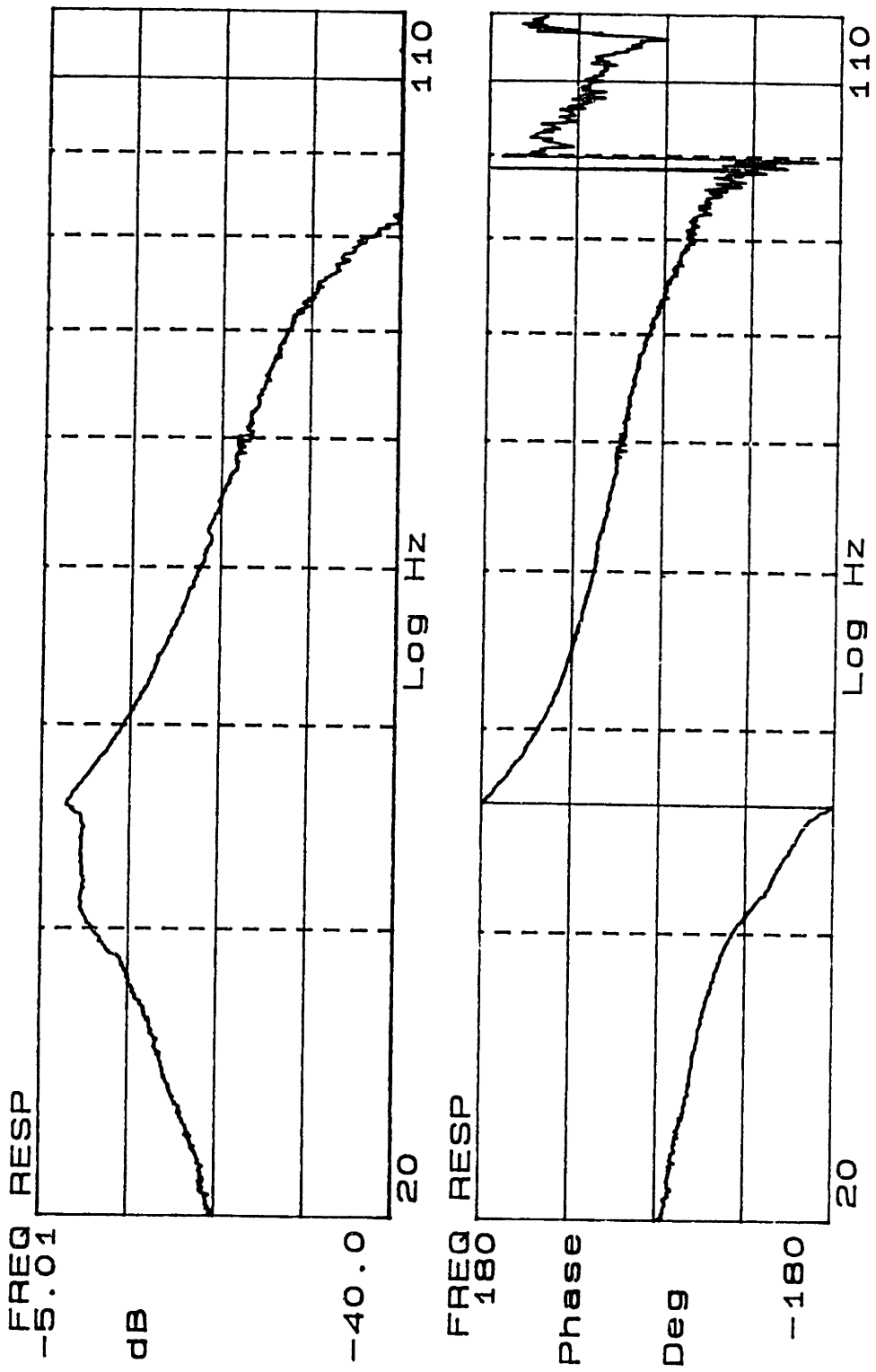

Figure 3.18: Measured frequency response of the system from a translational acceleration of the supporting frame to a translational acceleration of the HDA (output measured orthogonal to input).

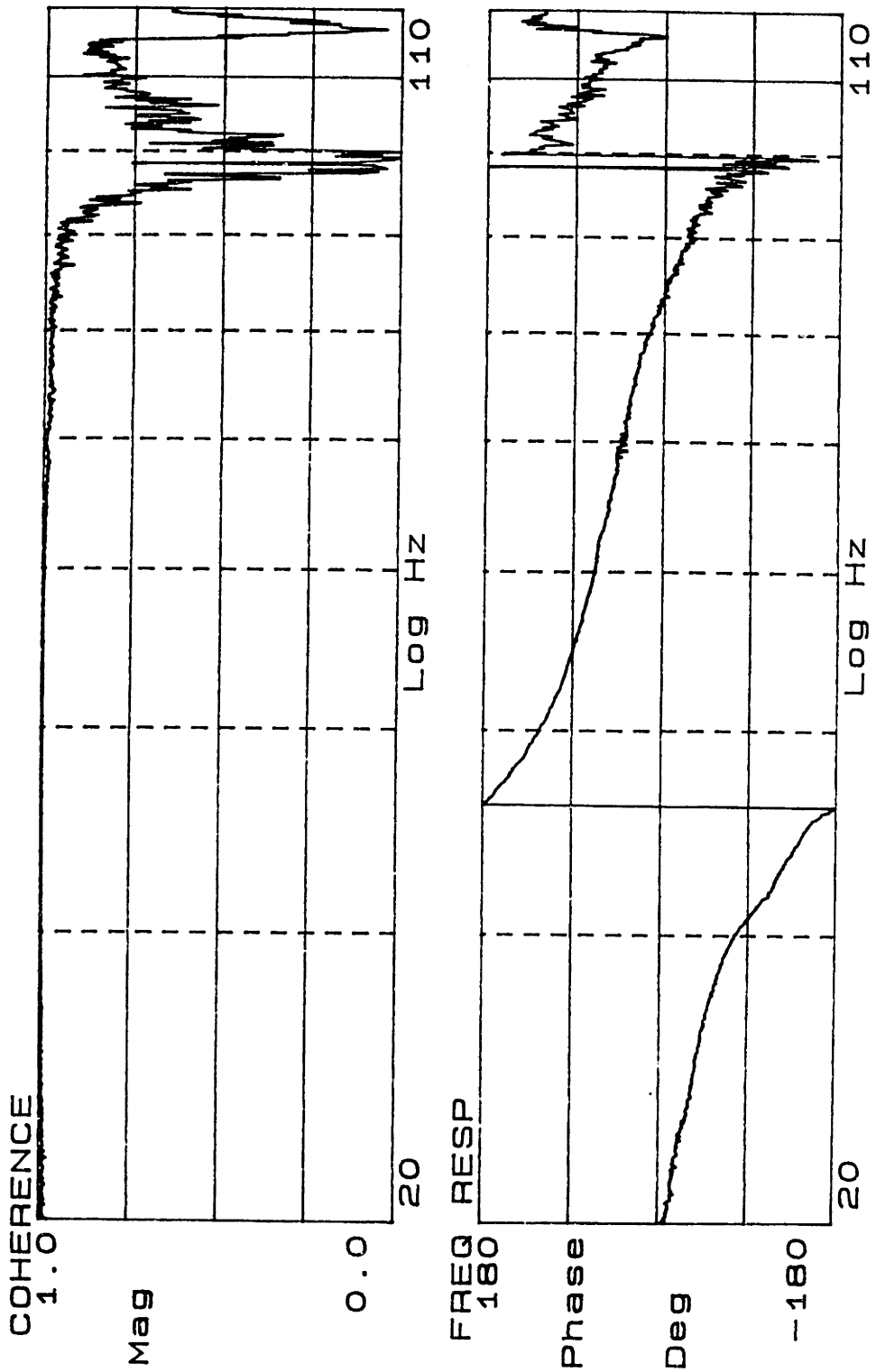

Figure 3.19: Plot of coherence vs. phase for measured frequency response of the system from a translational acceleration of the supporting frame to a translational acceleration of the HDA (output orthogonal to the input).

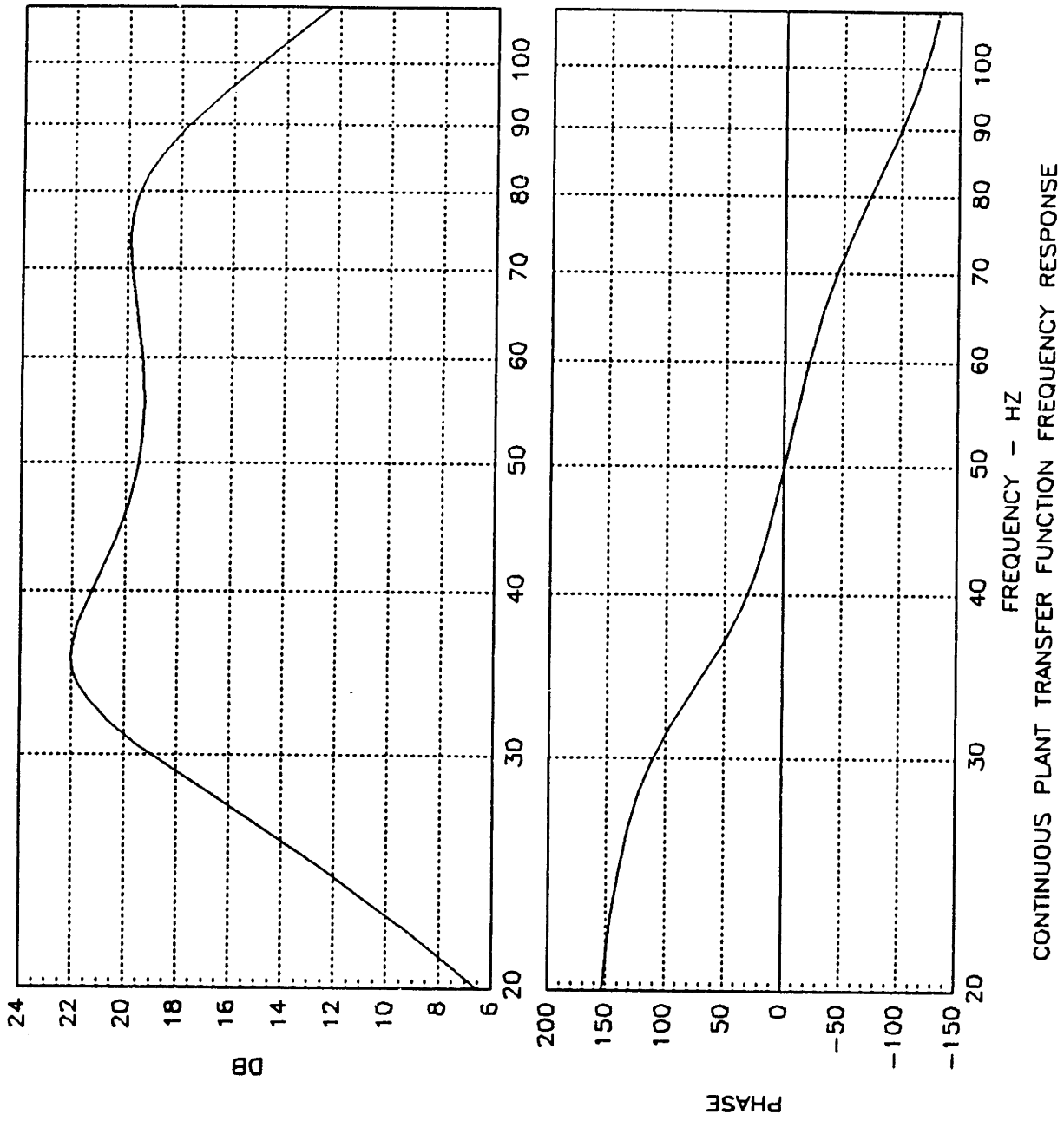

Figure 3.20: Modeled frequency response of the system from a translational acceleration of the supporting frame to an angular acceleration of the HDA.

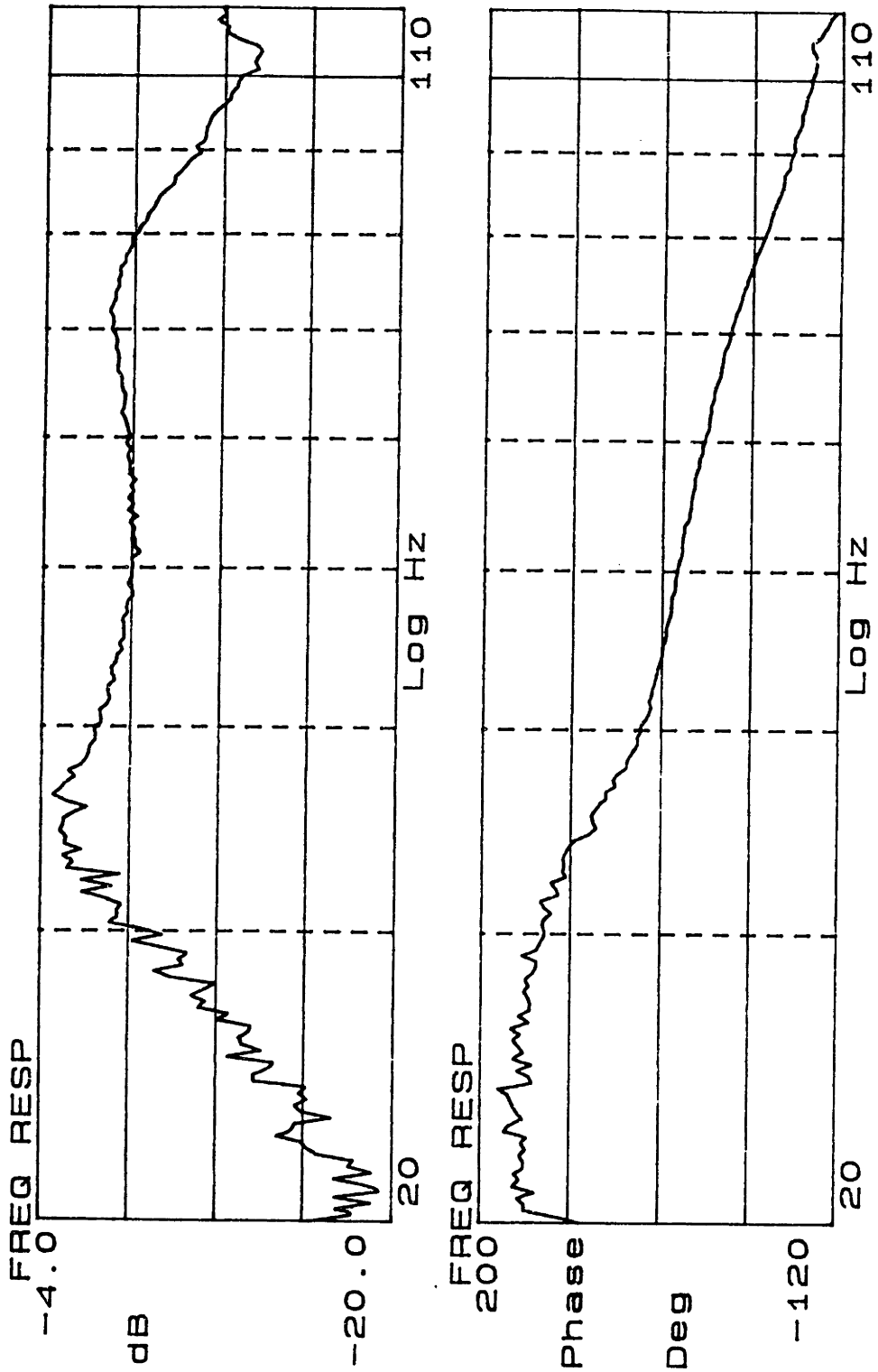

Figure 3.21: Measured frequency response of the system from a translational acceleration of the supporting frame to an angular acceleration of the HDA.

Chapter 4

Simulation of the ADCS in a Disk Drive with an Operating Servo System

The goal of computer simulation of an active disturbance compensation system was to develop an understanding of how feedback of HDA chassis angular acceleration affects disk drive tracking servo performance.

4.1 Disk Drive Block Diagram

A sketch of the complete disk drive block diagram is shown in Figure 4.1. The block diagram consists of three main components: the HDA Assembly, the Actuator Assembly, and the Servo Controller.

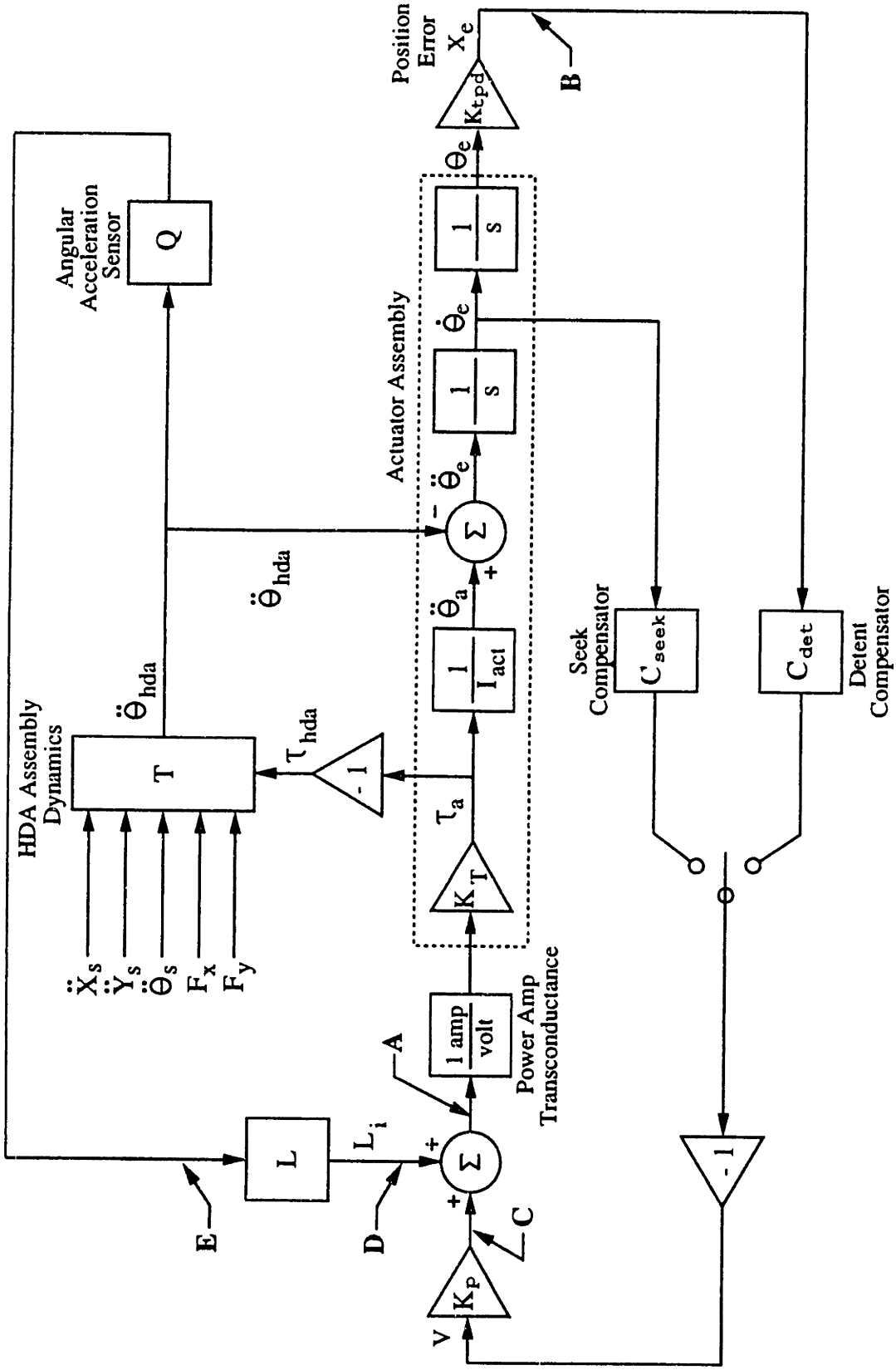

Figure 4.1: Sketch of disk drive block diagram.

4.1.1 HDA Assembly

The HDA Assembly is the dynamic model of the HDA motion presented in Section 3.6. The inputs to the HDA assembly include the three external accelerations of the supporting frame, $\ddot{X}_s$, $\ddot{Y}_s$, and $\ddot{\theta}_s$, and the three internal forces, or torque, acting internally to the shock mounts, F_x, F_y, and τ_θ. This torque, τ_θ, is a reaction torque on the HDA applied by the actuator. It may be especially large during seek activity and is represented in Figure 4.1 by τ_{hda}.

The output of the HDA Assembly, $\ddot{\theta}_{hda}$, represents the angular acceleration of the HDA. As discussed in Section 3.2.1, only pure rotation of the HDA can be linked to position error. The angular acceleration of the HDA, $\ddot{\theta}_{hda}$, is measured by a sensor, Q, and fed through a controller, L, before being summed into the servo control loop.

4.1.2 Actuator Assembly

The actuator assembly consists of a basic model describing the actuator dynamics.

The actuator arm structure was assumed to be rigid (infinite stiffness) over the frequency range of interest for shock, vibration, and wind-up (< 400Hz). As discussed in Section 3.2.1, the actuator was also assumed to be perfectly balanced about a frictionless bearing. Therefore, the actuator can be modeled as a pure inertia.

Angular acceleration of the actuator can then be calculated by dividing the actuator motor torque (directly proportional to motor current) by the moment of inertia of the actuator. As described in Section 3.2.1, position error is determined by the radial

difference in position of the read/write heads with respect to a specific track center line. Similarly, acceleration error is determined by the radial difference in acceleration of the read/write heads with respect to the specific track center. Therefore, in Figure 4.1, the difference junction determines the angular acceleration error, $\ddot{\theta}_e$.

Integrating the angular acceleration error once gives the angular velocity error, $\dot{\theta}_e$, and integrating again gives the angular position error, θ_e.

4.1.3 Drive Servo Controller Model

The drive has two primary controller modes: seek and detent. Seek mode is used during seek operations when the heads are in the process of moving from one track to another. To maintain control during a seek operation, the actuator must not be allowed to exceed a constrained velocity. Therefore, seek mode feeds back the velocity error through gain, C_{seek}, to the gain K_p. Once the read/write heads reach their desired track, the drive enters detent mode. Detent mode is used during read/write operations where positional information is necessary. Detent mode feeds back the angular position error, θ_e, through gain, K_{tpd}, to determine track position error, X_e, and then through a single lead compensator, C_{det}, to the gain K_p. The detent mode compensator in the model was designed such that the position loop had a bandwidth of approximately 400Hz with a 30 degree phase margin. The seek mode proportional compensator was approximated by adjusting its gain such that the response resembled a typical actuator seek profile.

Table 4.1: Actuator assembly simulation parameters.

Gain (Seek Mode)	K_p	1.667 $\frac{amp}{volt}$
Gain (detent mode)	K_p	0.210 $\frac{amp}{volt}$
Actuator Motor Torque Constant	K_t	0.25839 $\frac{N \cdot m}{amp}$
Moment of Inertia of Actuator	I_{act}	9.8122e-5 $\frac{Kg \cdot m^2}{1}$

The transconductance power amplifier translates voltage commands into motor current as $\frac{1amp}{1V}$.

The motor torque constant, K_t, relates the amount of motor torque produced per unit of input current to the motor. The motor torque, τ_{hda}, acts to rotate both the actuator inertia, I_{act}, and acts as a reaction torque on the HDA (hence the -1 sign as an input to the HDA Assembly).

4.2 Simulation Parameter Determination

The HDA Assembly transfer function parameters are found in Appendix B. The relevant transfer functions are T_{31}, T_{32}, T_{33}, T_{34}, T_{35}, and T_{36}. These transfer functions output the rotational acceleration of the HDA, $\ddot{\theta}_{hda}$, given any of the 6 inputs, $\ddot{X}_s$, $\ddot{Y}_s$, $\ddot{\theta}_s$, F_x, F_y, and τ_θ ($\tau_\theta = \tau_{hda}$).

The given Actuator Assembly parameters are listed in Table 4.1.

Initially, the value for the sensor, Q, was assumed to be 1 $\frac{V \cdot s^2}{rad}$.

The gain, K_{tpd}, was derived experimentally by feeding a swept sine input (75Hz to

2000Hz) from an HP 3562A Dynamic Signal Analyzer into the summing junction after the gain K_p in Figure 4.1. An open loop frequency response was then measured from a point (A) before the actuator motor to point (B) immediately following the gain, K_{tpd}. In the disk drive system model, this open loop transfer function is described by:

$$\frac{B(s)}{A(s)} = \frac{K_t K_{tpd}}{I_{act} s^2} \tag{4.1}$$

The values for the actuator motor torque constant, K_t, and the moment of inertia of the actuator, I_{act}, are known. Therefore, by substituting a value of 1 for K_{tpd} into the transfer function above and comparing the magnitude of the frequency response to the magnitude of the experimentally measured frequency response, the gain, K_{tpd}, can be derived. Figure 4.2 shows a plot of the experimentally measured frequency response. Figure 4.3 shows the predicted frequency response (using MATRIXx) for both an analog and a more accurate discrete-time system where the gain, K_{tpd}, is equal to $3.4277 \cdot 10^4 \frac{V \cdot s}{rad}$. In comparison, both plots have approximately the same magnitude and slope across the frequency range. Likewise, both plots show an equivalent change in phase across the frequency range from 75Hz to 2000Hz. The hardware used to measure the phase in Figure 4.2 wrapped the negative 180 degree phase around to appear as an initial positive 180 degree phase. Therefore, any phase less than -180 degrees appears as (360 + phase) in the plot.

The continuous detent lead compensator, C_{det}, transfer function parameters were

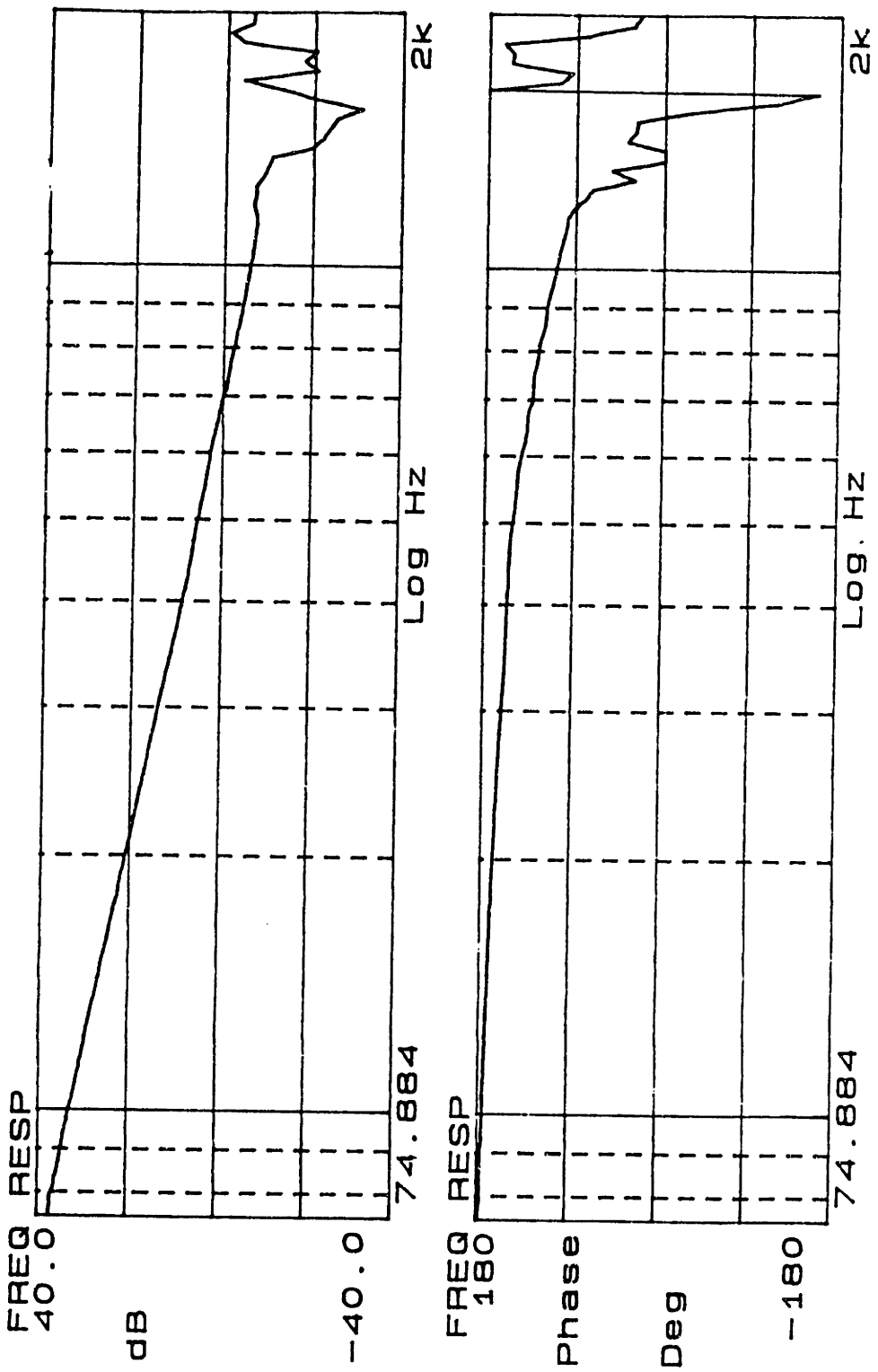

Figure 4.2: Measured open loop actuator frequency response.

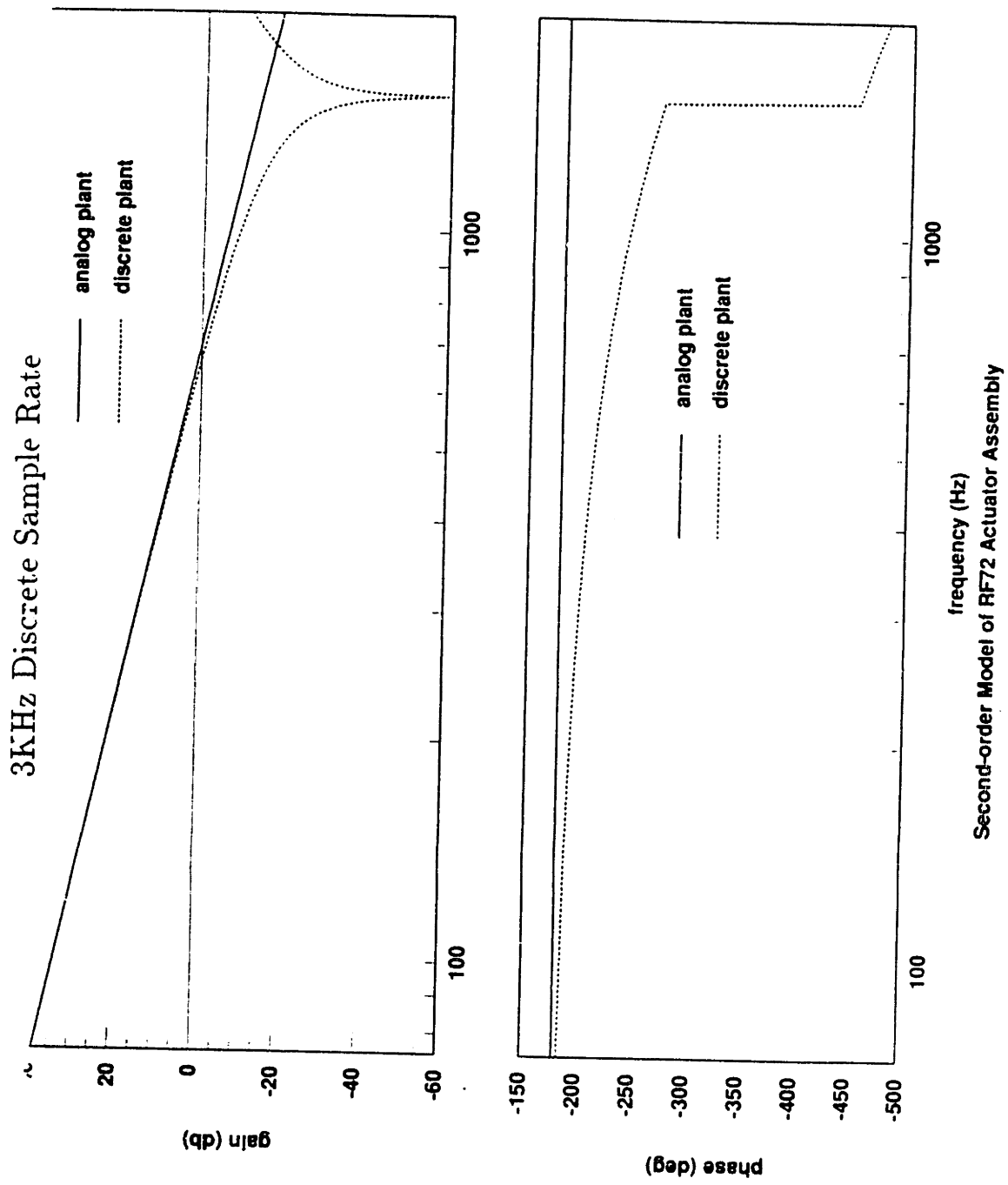

Figure 4.3: Simulated open loop actuator frequency response.

determined in a similar manner. Using an HP 3562A swept sine input at the same location (A), the open loop controller frequency response was measured from points (A) to (C). Figure 4.4 shows the results of this measurement. From this plot, a lead compensator was chosen to have the similar characteristics of 30 degree phase margin at approximately 400Hz, and approximately the same gain across the frequency range from 75Hz to 2000Hz. A lead controller that approximately fits these parameters is given by:

$$C_{det} = \frac{.61693s + 841.86}{s + 4628.9} \tag{4.2}$$

Figure 4.2 shows a plot of the modeled magnitude and phase of the lead compensator in series with the actuator dynamics over a frequency range from 75Hz to 2000Hz. In this case, the modeled magnitude of the frequency response doesn't match exactly the measured magnitude of the frequency response with the compensator in series, but the modeled gain is a close approximation. However, the goal of achieving a 30 degree phase margin has been achieved.

The velocity controller gain, C_{seek}, is assumed to be equal to 1.

4.3 MATRIXx Simulation

Once the system parameters were derived, the information was placed into a MATRIXx System Build model for simulation. A plot of this is shown in Figure 4.6. MATRIXx simulation source files are included in Appendix C.

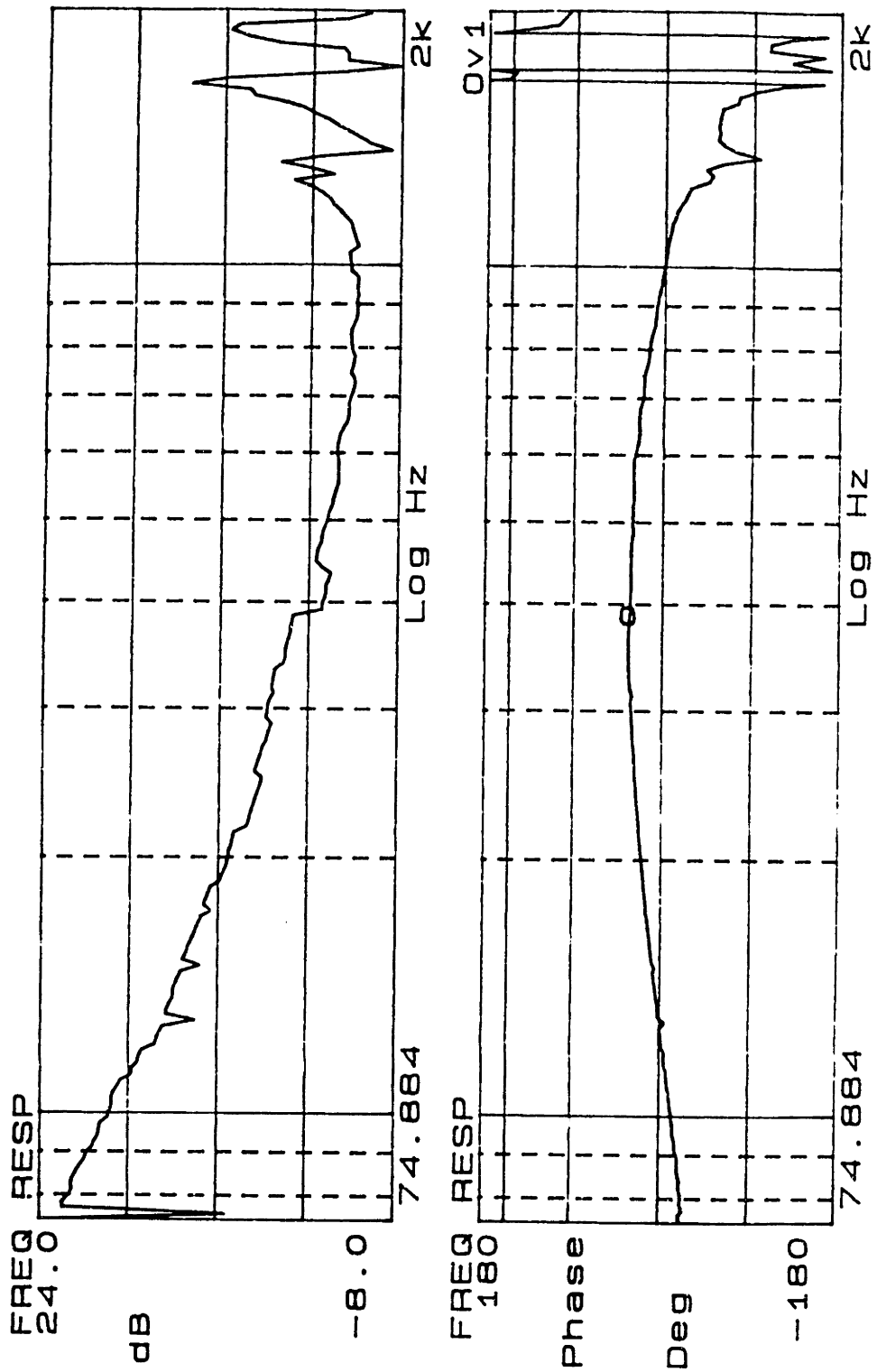

Figure 4.4: Measured open loop frequency response of drive lead controller coupled with actuator.

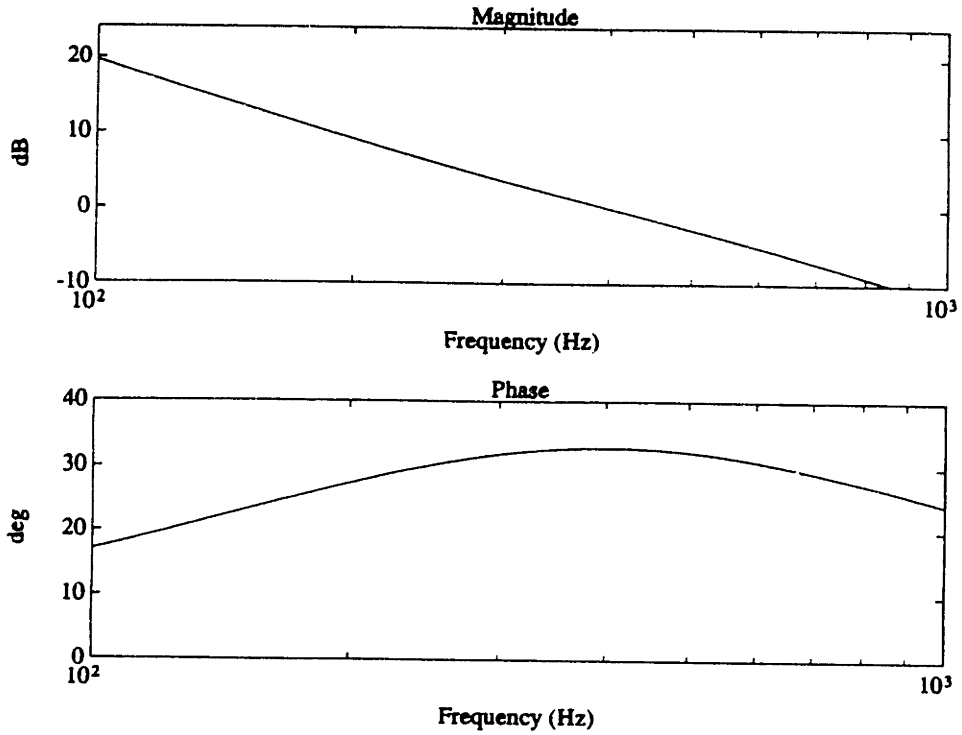

Figure 4.5: Modeled open loop frequency response of drive lead controller coupled with actuator

The System Build model included both the 6 degree-of-freedom HDA dynamic model developed in Section 3.6 and the servo model presented in Section 4.1. This model allowed for simple simulation and comparison of the position error as a function of controller design, L, and the type and location of the inputs. The inputs took the form of actuator seeks, external shock and vibration, and shock and vibration internal to the shock mounts. The sensor characteristics, Q, were also altered in order to place a simulated filter in the feedback loop.

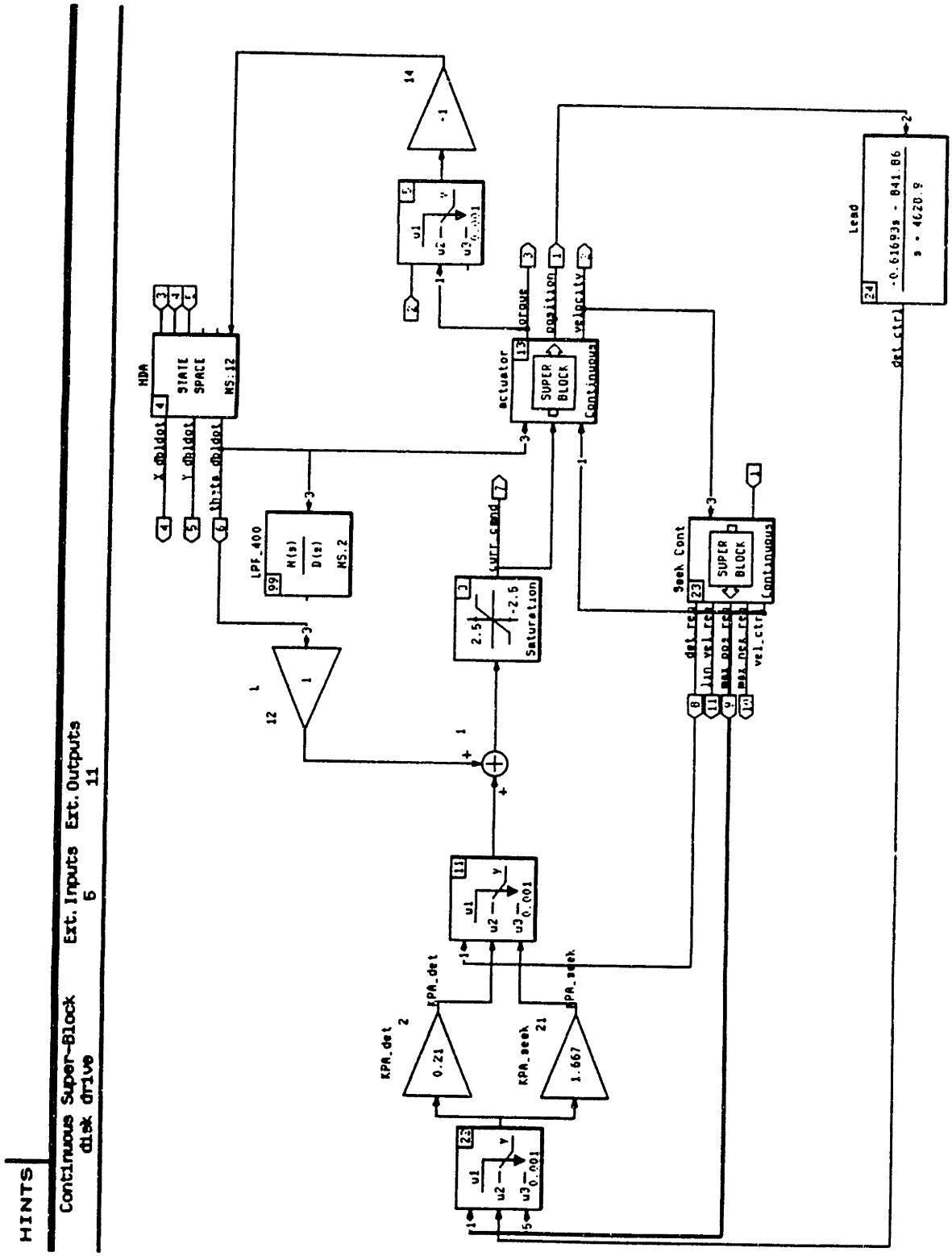

Figure 4.6: MATRIXx System Build model for drive simulation.

4.4 Determination of Accelerometer Compensation to Eliminate the Effects of Shock, Vibration, and Wind-up

To minimize the effects of shock, vibration, and wind-up, an optimal acceleration feedback controller, L, had to be chosen.

As a starting point, it was useful to develop a transfer function relationship between an external disturbance input (to the supporting frame) and a track position error output in terms of the feedback compensator L. By minimizing this derived function in terms of L, the track position error due to an external disturbance input was also minimized.

Based on the block diagram of the system presented in Section 4.1, a transfer function was obtained from an external translational disturbance input, $\ddot{X}_s$, to a position error output, X_e.

This was simplified using DOE-MACSYMA by creating and solving the three independent equations shown below. The three equations were derived from Figure 4.1 using simple block diagram algebra.

$$\ddot{\theta}_{hda} = \ddot{X}_s T_{31} - \tau T_{36} \tag{4.3}$$

$$\tau = K_t(LQ\ddot{\theta}_{hda} - X_e C_{det} K_p) \tag{4.4}$$

$$X_e = \frac{\frac{\tau}{I_{act}} - \ddot{\theta}_{hda}}{s^2} K_{tpd} \tag{4.5}$$

Solving the above three equations for $\frac{X_e}{\ddot{X}_s}$ gives,

$$\frac{X_e}{\ddot{X}_s} = \frac{(K_t K_{tpd} LQ - I_{act} K_{tpd}) T_{31}}{(I_{act} K_t LQ s^2 + C_{det} I_{act} K_p K_t K_{tpd}) T_{36} + I_{act} s^2 + C_{det} K_p K_t K_{tpd}} \tag{4.6}$$

where $\ddot{X}_s$ is the external disturbance input, and T_{31} and T_{36} are the HDA transfer functions given in Appendix B.

Appendix D contains the DOE-MACSYMA simulation source files.

Substitution of the above numerical values into Equation 4.6 yields:

$$\frac{X_e}{\ddot{X}_s} = \frac{N_{tf}}{D_{tf}} \tag{4.7}$$

where (displayed to 3 significant digits),

$$\begin{aligned} N_{tf} &= (2.91 \cdot 10^{11} L - 1.11 \cdot 10^{8}) s^4 + (1.51 \cdot 10^{15} L - 5.73 \cdot 10^{11}) s^3 + \\ &\quad (7.31 \cdot 10^{17} L - 2.78 \cdot 10^{14}) s^2 \end{aligned} \tag{4.8}$$

and,

$$\begin{aligned} D_{tf} &= (7.75 \cdot 10^{2} L + 2.42) s^7 + (3.65 \cdot 10^{6} L + 1.20 \cdot 10^{4}) s^6 + \\ &\quad (3.40 \cdot 10^{8} L + 3.64 \cdot 10^{7}) s^5 + (1.65 \cdot 10^{11} L + 5.71 \cdot 10^{9}) s^4 + \\ &\quad 2.36 \cdot 10^{13} s^3 + 1.41 \cdot 10^{16} s^2 + 1.61 \cdot 10^{18} s + 4.56 \cdot 10^{20} \end{aligned} \tag{4.9}$$

Setting the left hand side of Equation 4.7 to zero and solving for L gives the

function in terms of s which minimizes the equation. The solution turns out to be a constant gain of magnitude:

$$L_{opt} = 3.7974379 \cdot 10^{-4} \tag{4.10}$$

At this value of L, the value of the position error, X_e, is zero for all translational external disturbances! Surprisingly, the compensator requires no dynamics to satisfy this condition!

Substitution of this value for L into the MATRIXx System Build model described in Section 4.3 shows that this value of L simultaneously completely desensitizes the track position error, X_e, to all disturbances, $\ddot{X}_s$, $\ddot{Y}_s$, $\ddot{\theta}_s$, F_x, F_y, and τ_θ.

Figure 4.7 shows a comparison of the simulated track position error due to a 15ms seek between an uncompensated system ($L = 0$) and a compensated system at ($L = L_{opt}$). As shown in the figure, the position error induced by a torque applied to the HDA during a drive seek operation has been eliminated through the feedback of the HDA angular acceleration through a gain of $L = L_{opt}$.

This optimal gain can also be derived by setting the numerator in Equation 4.6 equal to zero. This gives the solution in terms of the moment of inertia of the actuator, I_{act}, the motor torque constant, K_t, and the sensor, Q, as shown in the following equation:

$$L_{opt} = \frac{I_{act}}{K_t Q} = 3.7974379 \cdot 10^{-4} \tag{4.11}$$

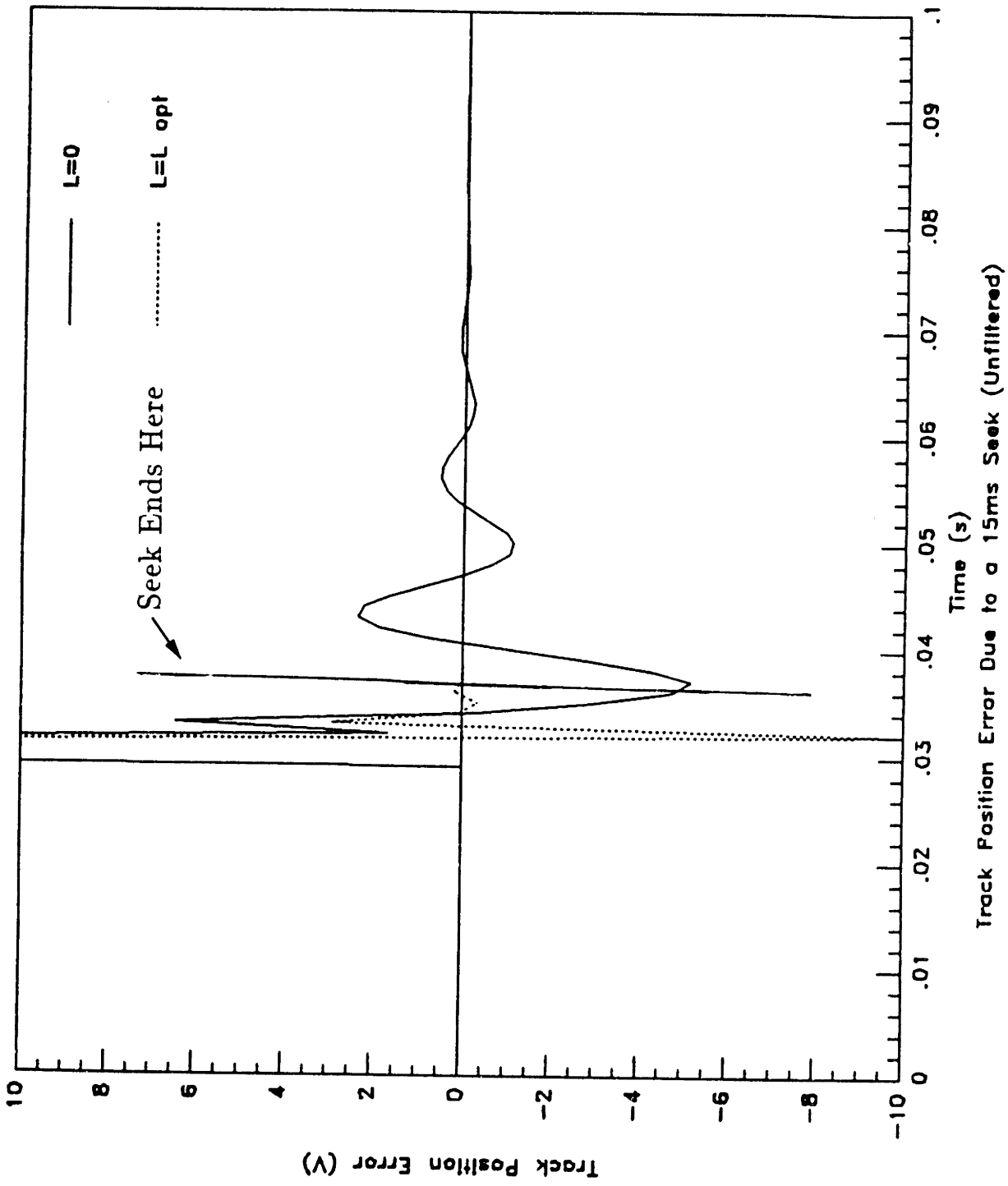

Figure 4.7: Comparison of track position error due to a 15ms seek (simulated).

4.5 Stability Issues

It is important to understand the robustness of the existing control system to the addition of this new feedback. The robustness can be observed from a root locus plot of the system. By supplying the simulation software with an open loop transfer function from a point (D) immediately following the feedback gain, L, to the point (E) immediately preceding the feedback gain, L, it will compute and plot the root locus of the closed loop system as feedback gain, L, varies from zero to infinity (shown as a gain L_i in Figure 4.1).

Using DOE-MACSYMA, this open loop transfer function is computed by solving the following two equations for $\frac{\ddot{\theta}_{hda}}{L_i}$:

$$\tau = K_t(L_i - \frac{K_p C_{det} K_{tpd}(\frac{\tau}{I_{act}} - \ddot{\theta}_{hda})}{s^2}) \tag{4.12}$$

and:

$$\ddot{\theta}_{hda} = -\tau T_{36} \tag{4.13}$$

Solving for $\frac{\ddot{\theta}_{hda}}{L_i}$ gives:

$$\frac{\ddot{\theta}_{hda}}{L_i} = \frac{I_{act} K_t s^2 T_{36}}{K_p K_t K_{tpd}(C_{det} I_{act} T_{36} + C_{det}) + I_{act} s^2} \tag{4.14}$$

Substituting in the numerical values gives:

$$\frac{\ddot{\theta}_{hda}}{L_i} = \frac{N_{rl}}{D_{rl}} \tag{4.15}$$

where (displayed to 3 significant digits):

Table 4.2: Location of poles and zeros in unfiltered system.

Zeros	Poles
0	-38.767 + 206.61i
0	-38.767 - 206.61i
0	-118.03 + 471.21i
0	-118.03 - 471.21i
-42.248 + 210.09i	-1175.6 + 2537.6i
-42.248 - 210.09i	-1175.6 - 2537.6i
-4634.3	-2305.1

$$N_{rl} = 3.20 \cdot 10^2 s^7 + 1.51 \cdot 10^6 s^6 + 1.40 \cdot 10^8 s^5 + 6.81 \cdot 10^{10} s^4 \qquad (4.16)$$

and:

$$D_{rl} = s^7 + 4.97 \cdot 10^3 s^6 + 1.50 \cdot 10^7 s^5 + 2.36 \cdot 10^{10} s^4 + 9.75 \cdot 10^{12} s^3 + 5.81 \cdot 10^{15} s^2 + 6.56 \cdot 10^{17} s + 1.83 \cdot 10^{20} \qquad (4.17)$$

Placing this transfer function in MATRIXx gives the root locus plot shown in Figure 4.8.

From the plot, it is clear that the system will become unstable at some gain greater than zero. The exact gain was determined to be $1.3 \cdot 10^{-2}$. This value was nearly 20 times greater than the optimal gain, L_{opt}, for this disk drive. This suggested that it should be exceedingly difficult to destabilize an existing servo system with the introduction of HDA acceleration feedback designed to reject shock, vibration, and wind-up. Of course, high frequency, unmodeled modes could be a problem.

Figure 4.9 shows the exact position of the poles on the root locus when the system is at the optimal gain.

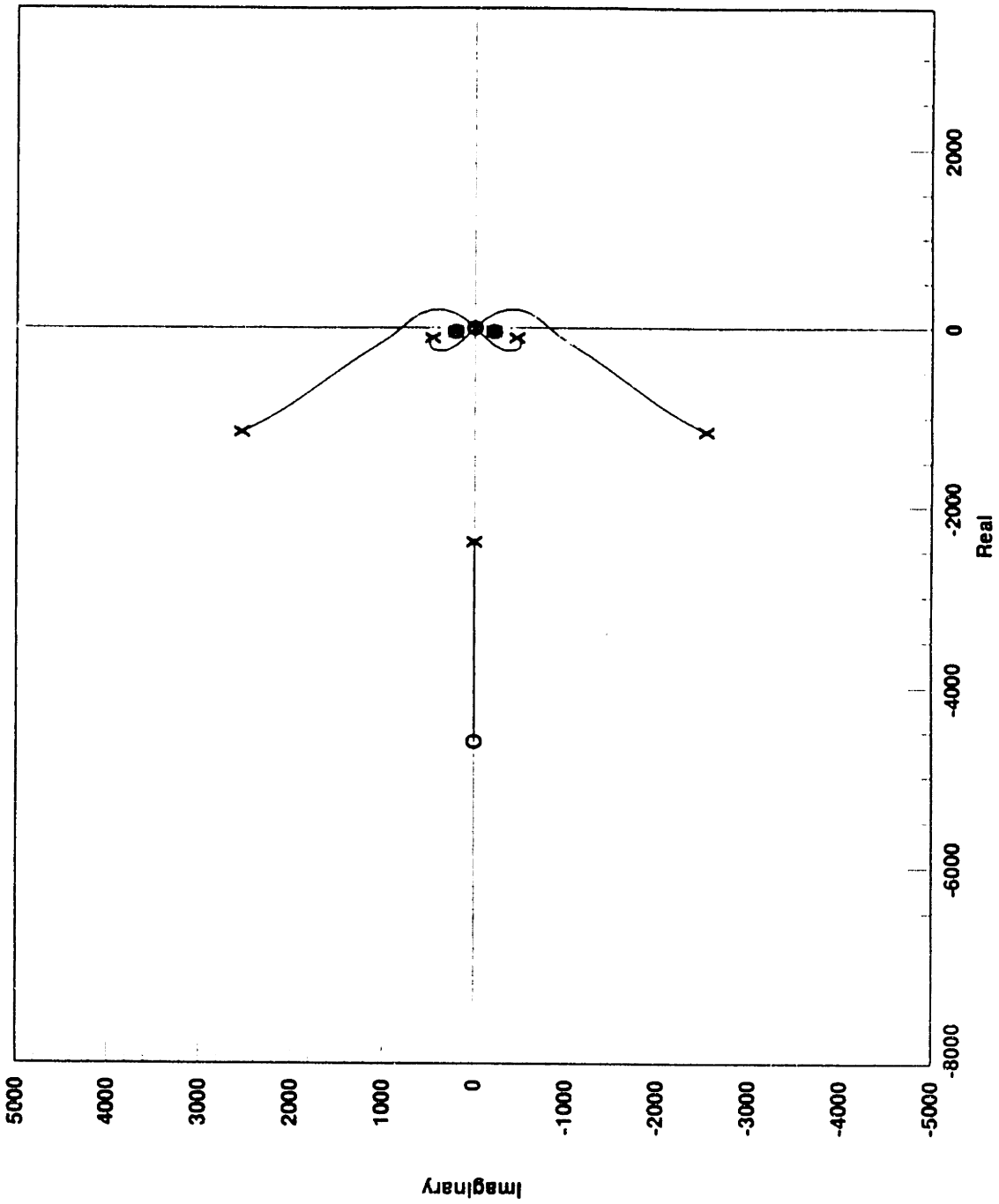

Figure 4.8: Root locus with acceleration feedback.

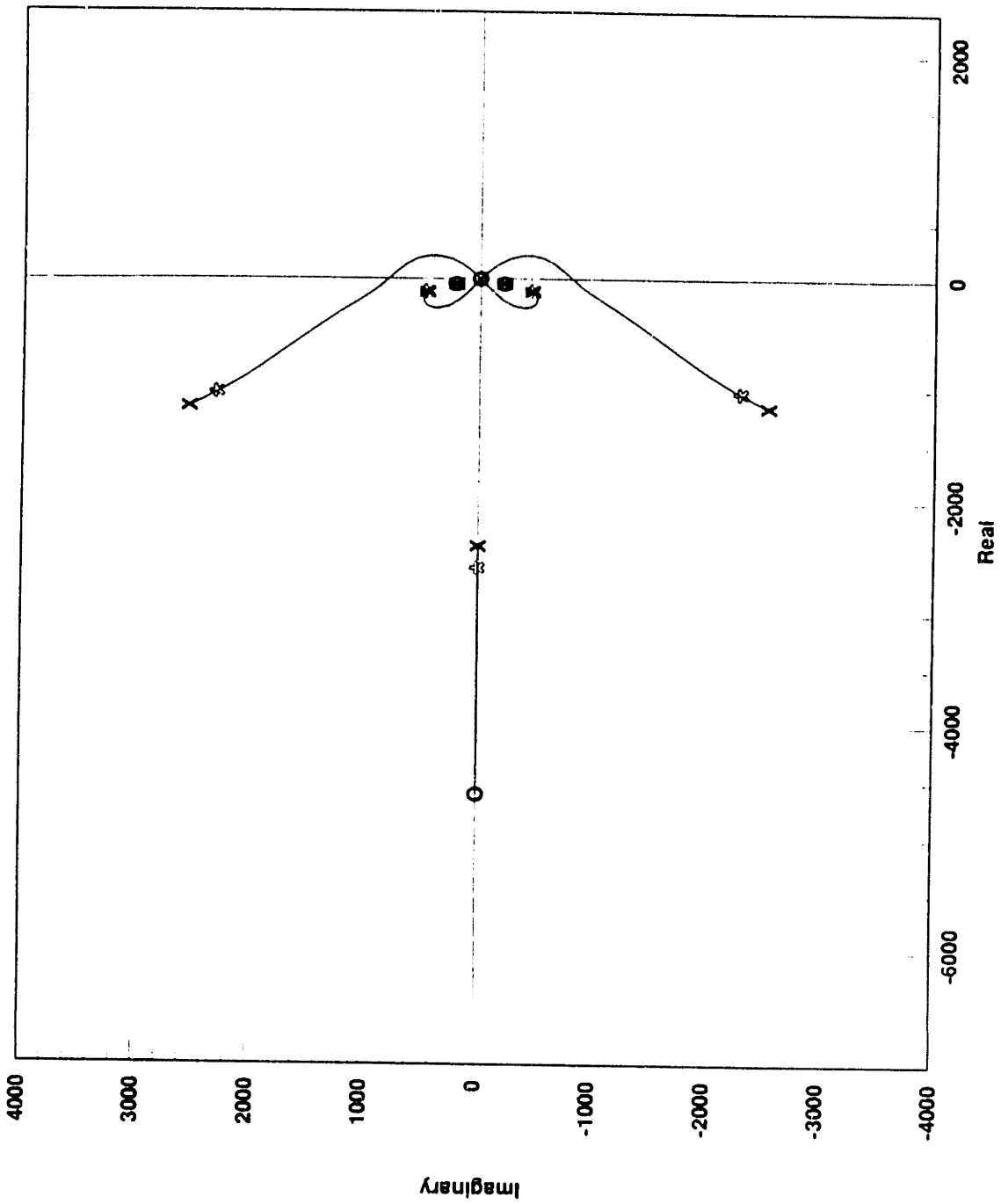

Figure 4.9: Position of the poles on the root locus at optimal gain.

Table 4.3: Location of poles on root locus at the optimal gain.

-38.769	+	206.61i
-38.769	-	206.61i
-119.34	+	472.68i
-119.34	-	472.68i
-1056.1	+	2287.5i
-1056.1	-	2287.5i
-2514.3		

The location of the poles on the root locus at a gain of L_{opt} is given in Table 4.3.

4.6 Effective Improvement Range

Although the stability range of the closed loop system is very large, the range of improvement in decreasing position error is much smaller. As the feedback gain is increased from 0 to L_{opt}, the position error due to disturbances goes to zero. However, if the gain is increased beyond this point, the feedback of HDA acceleration begins to *cause* position error. If the optimal gain, L_{opt}, is doubled, the magnitude of the position error is equal to the magnitude of the position error in an uncompensated system. If the gain is increased beyond this point, the position error induced by a disturbance will be larger than the position error induced by the same disturbance in an uncompensated system.

Figure 4.10 shows the magnitude of position error (z-axis) versus gain, L, (y-axis) and frequency of external translational disturbance input (x-axis). The gain varies from 0 to 0.001, and the frequency varies from 10Hz to 200Hz. From the plot, it is

Table 4.4: Improvement in position error with variation from optimal gain.

Gain Variation $\pm$ from (L_{opt})	Factor of Improvement
0%	∞
5%	20.0
10%	10.0
15%	6.6
20%	5.0
25%	4.0
30%	3.3
35%	2.8
40%	2.5
45%	2.2
50%	2.0

apparent that the position error varies linearly with the feedback gain, and is not affected by the frequency of the input disturbance.

At the optimal gain, the improvement in position error is infinite, meaning that the position error goes to zero. However, if the optimal gain is varied by as much as $\pm$ 20%, the position error is improved less than 5 times. At $\pm$ 50%, the position error is improved by less than a factor of 2. The position error improvement due to variations from 0 to 50% is shown in Table 4.4.

Note: A factor of improvement of 2 signifies that the magnitude of the position error due to an input disturbance has decreased by a factor of 2 over the magnitude of the position error due to the same disturbance in an uncompensated system.

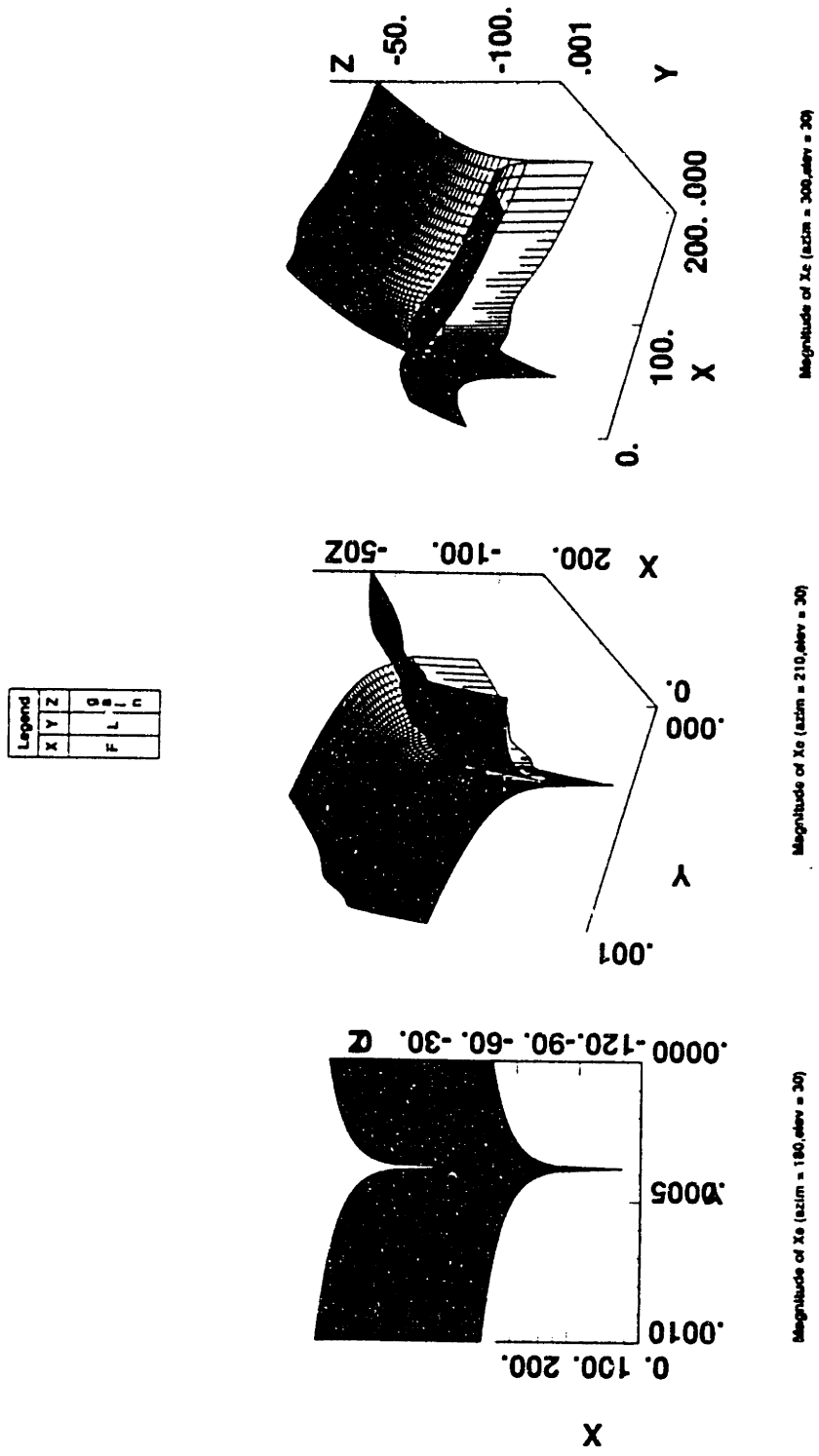

Figure 4.10: Three dimensional view of track position error as a function of gain (L) and input disturbance frequency (unfiltered).

4.7 Effect of Filtering Sensor

In an actual application of ADCS, the output from the accelerometer would need to be filtered to remove unwanted high frequency noise and to help ensure system stability in the presence of HDA flexible modes in excess of about 400Hz that might otherwise act to destabilize the existing servo system with the introduction of acceleration feedback.

4.7.1 200Hz 2-Pole Low Pass Filter

Since the rigid-body rotational resonance of the drive HDA is about 75Hz, a good first choice of a low pass filter would have a cut-off frequency of 200Hz. An example of a simple 2-pole low pass filter is shown below:

$$Filter_{200} = \frac{(2 \cdot \pi \cdot 200)^2}{s^2 + 2 \cdot (.7) \cdot 2 \cdot \pi \cdot 200 \cdot s + (2 \cdot \pi \cdot 200)^2} \tag{4.18}$$

Replacing the sensor transfer function, Q, in Equation 4.6 by the low pass filter described in Equation 4.18 gives the new system transfer function described below:

$$\frac{X_e}{\ddot{X}_s} = \frac{N_{200}}{D_{200}} \tag{4.19}$$

where (displayed to 3 significant digits):

$$\begin{aligned} N_{200} \;=\; & 6.64 \cdot 10^7 s^6 + 3.43 \cdot 10^{11} s^5 + (2.71 \cdot 10^{14} - 2.76 \cdot 10^{17} L) s^4 + \\ & (5.43 \cdot 10^{17} - 1.43 \cdot 10^{21} L) s^3 + (2.63 \cdot 10^{20} - 6.92 \cdot 10^{23} L) s^2 \end{aligned} \tag{4.20}$$

and:

$$\begin{aligned} D_{200} &= 1.45s^9 + 7.21 \cdot 10^3 s^8 + (7.33 \cdot 10^8 L + 2.41 \cdot 10^7)s^7 + \\ &\quad (3.46 \cdot 10^{12} L + 4.56 \cdot 10^{10})s^6 + (3.22 \cdot 10^{14} L + 4.86 \cdot 10^{13})s^5 + \\ &\quad (1.56 \cdot 10^{17} L + 6.26 \cdot 10^{16})s^4 + 2.33 \cdot 10^{19} s^3 + 1.36 \cdot 10^{22} s^2 + \\ &\quad 1.53 \cdot 10^{24} s + 4.32 \cdot 10^{26} \end{aligned} \tag{4.21}$$

However, with the low pass filter included in the model, the optimal gain, L_{opt}, now varies with frequency as shown in Figure 4.11. In this plot, the position error is shown on the (z-axis), the feedback gain, L, is shown on the (y-axis), and the frequency of a sinusoidal input disturbance, $\ddot{X}_s$, is shown on the (x-axis). In this plot, the optimal gain (trough in the plot), curves from a high optimal gain for low frequency disturbance inputs to a low optimal gain for higher frequency disturbance inputs. More clearly, with the 200Hz filter, the optimal gain varies from $(3.65 \cdot 10^{-4})$ at 40Hz to $(2.20 \cdot 10^{-4})$ at 130Hz. Therefore, it is impossible to choose a single gain to optimize the position error at all frequencies.

With the 200Hz low pass filter in the system, the open loop frequency response for the root locus computation becomes:

$$\frac{\ddot{\theta}_{hda}}{L_i} = \frac{I_{act} K_t s^2 T_{36} Q_{200}}{K_p K_t K_{tpd}(C_{det} I_{act} T_{36} + C_{det}) + I_{act} s^2} \tag{4.22}$$

Substituting numerical values into the above equation gives:

$$\frac{\ddot{\theta}_{hda}}{L_i} = \frac{N_{rl200}}{D_{rl200}} \tag{4.23}$$

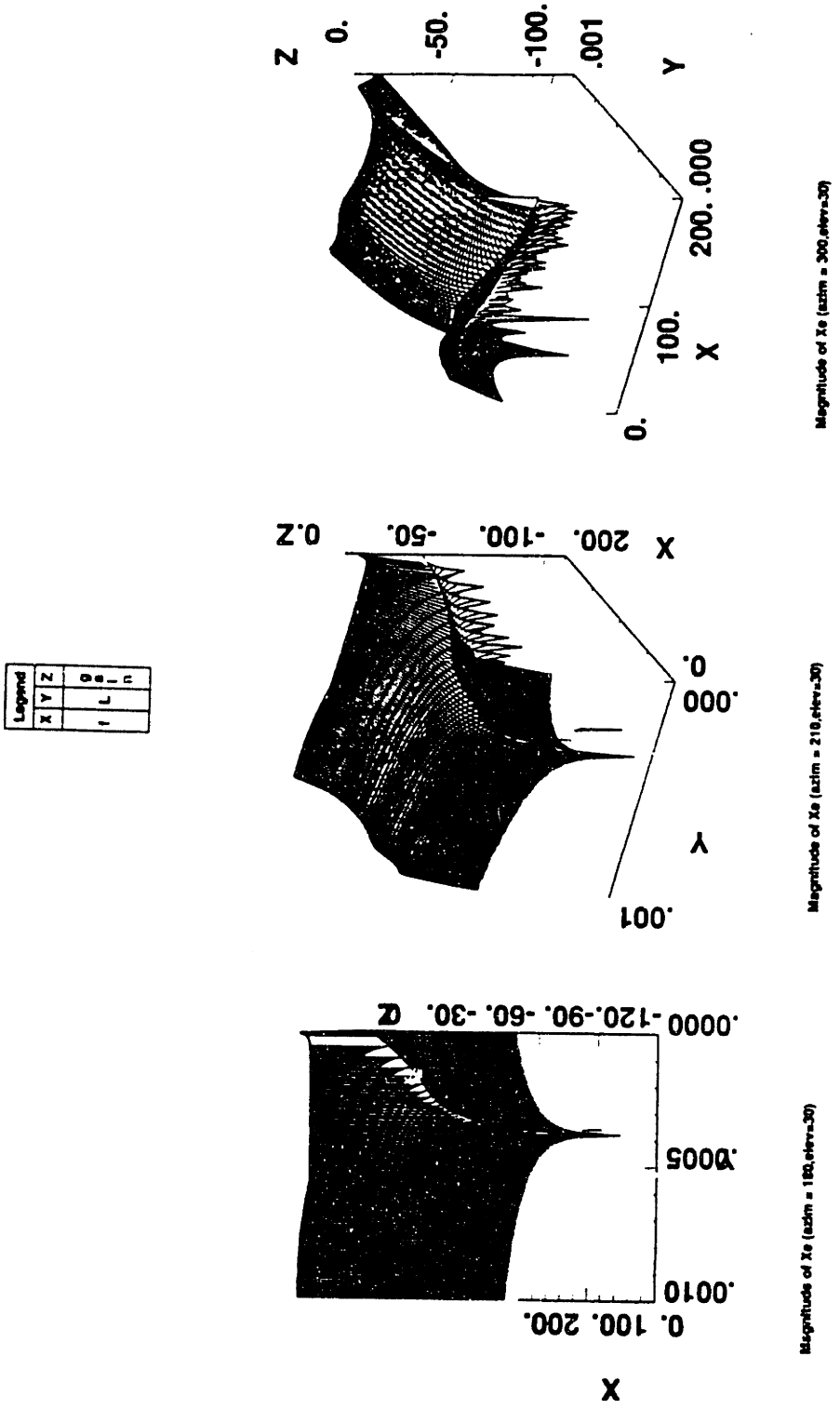

Figure 4.11: Three dimensional view of track position error as a function of gain (L) and input disturbance frequency (200Hz filter).

Table 4.5: Location of the poles on the root locus of the system with a 200Hz low pass filter at the optimal gain.

-38.769	+	206.61i
-38.769	-	206.61i
-118.40	+	473.47i
-118.40	-	473.47i
-817.15	+	866.28i
-817.15	-	866.28i
-1185.4	+	2616.8i
-1185.4	-	2616.8i
-2409.8		

where (displayed to 3 significant digits):

$$N_{rl200} = 5.06 \cdot 10^8 s^7 + 2.38 \cdot 10^{12} s^6 + 2.22 \cdot 10^{14} s^5 + 1.07 \cdot 10^{17} s^4 \tag{4.24}$$

and:

$$\begin{aligned} D_{rl200} \;=\; & s^9 + 6.73 \cdot 10^3 s^8 + 2.54 \cdot 10^7 s^7 + 5.79 \cdot 10^{10} s^6 + \\ & 7.50 \cdot 10^{13} s^5 + 6.02 \cdot 10^{16} s^4 + 2.63 \cdot 10^{19} s^3 + 1.05 \cdot 10^{22} s^2 + \\ & 1.38 \cdot 10^{24} s + 2.97 \cdot 10^{26} \end{aligned} \tag{4.25}$$

The 200Hz low pass filter adds two poles to the unfiltered system ($879.64 \pm 897.41i$). A plot of the root locus of the system with the 200Hz filter is shown in Figure 4.12. With the addition of a 200Hz filter, the range of stability increases from $1.3 \cdot 10^{-2}$ (unfiltered) to $2.0 \cdot 10^{-2}$ (200Hz filter). A plot of the position of the poles on the root locus when ($L = 3.79 \cdot 10^{-4}$) is shown in Figure 4.13. Table 4.5 contains the position of the poles on the root locus at a gain equal to L_{opt}.

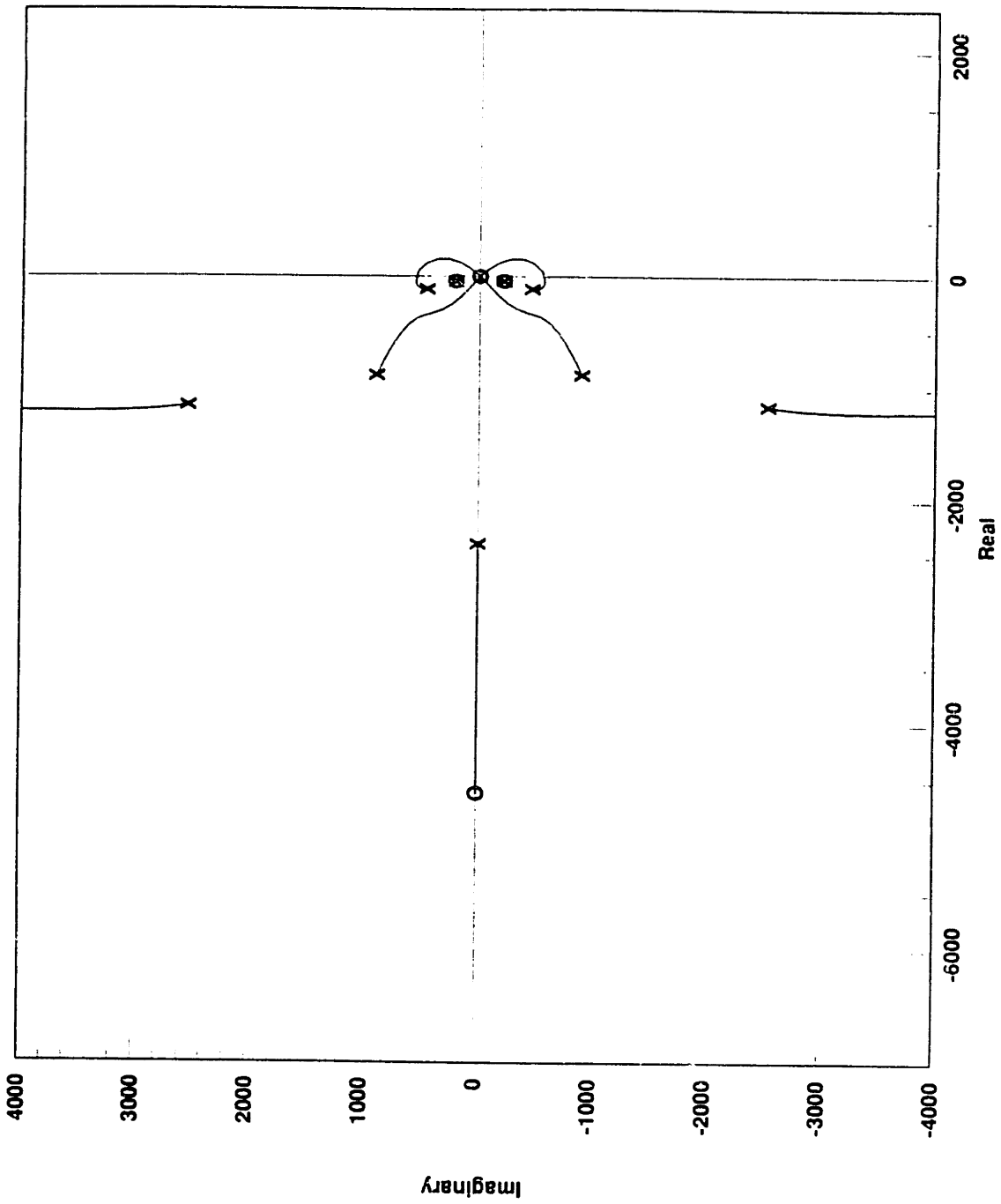

Figure 4.12: Root locus of system with 200Hz low pass filter.

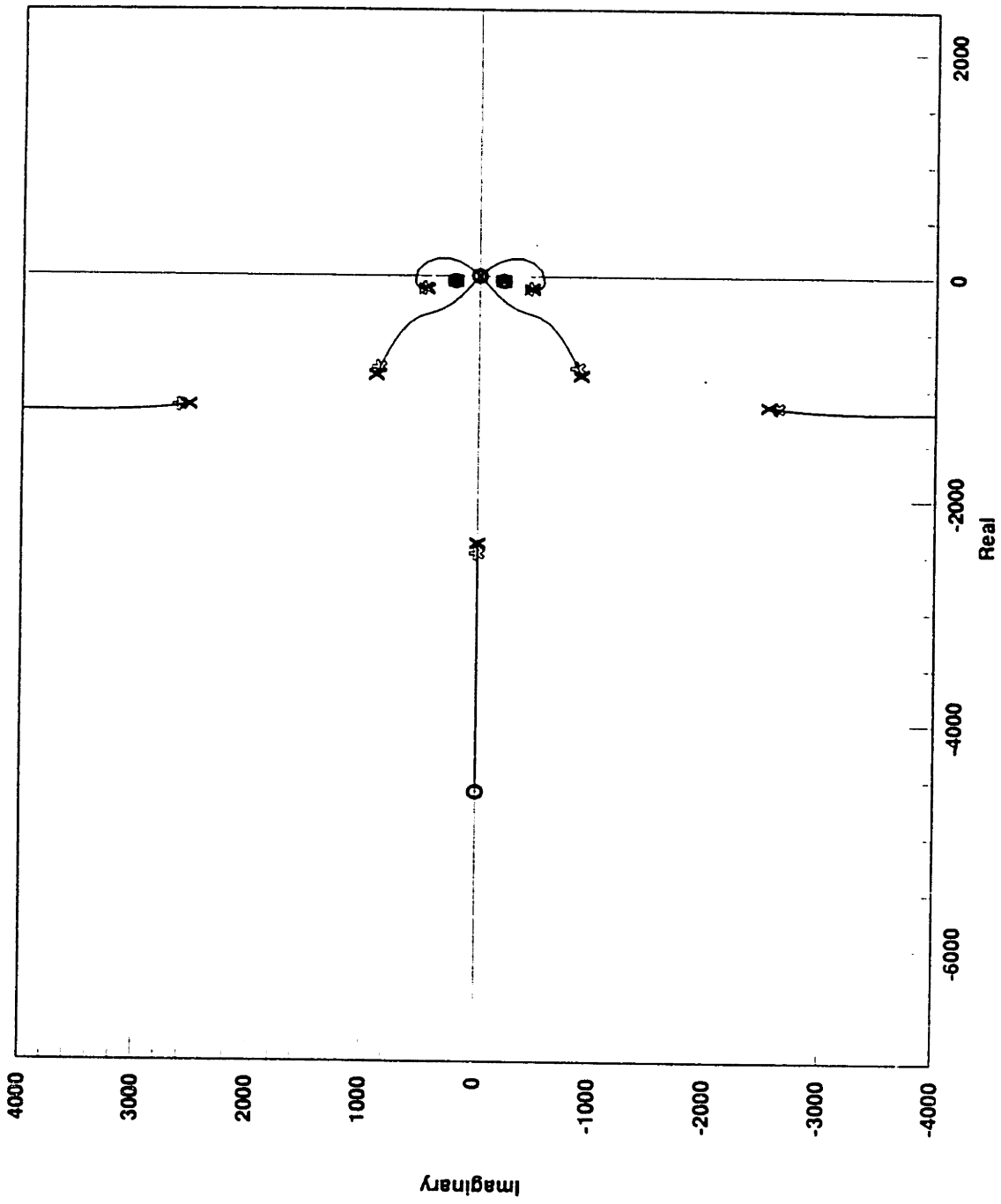

Figure 4.13: Position of poles on root locus at unfiltered optimal gain (200Hz filter).

4.7.2 400Hz 2-Pole Low Pass Filter

If the 200Hz low pass filter is replaced by a 400Hz low pass filter of the form shown below:

$$Filter_{400} = \frac{(2 \cdot \pi \cdot 400)^2}{s^2 + 2 \cdot (.7) \cdot 2 \cdot \pi \cdot 400 \cdot s + (2 \cdot \pi \cdot 400)^2} \tag{4.26}$$

The system transfer function becomes:

$$\frac{X_e}{\ddot{X}_s} = \frac{N_{400}}{D_{400}} \tag{4.27}$$

where (displayed to 3 significant digits):

$$\begin{aligned} N_{400} &= 1.08 \cdot 10^8 s^6 + 5.57 \cdot 10^{11} s^5 + (9.50 \cdot 10^{14} - 1.79 \cdot 10^{18} L) s^4 + \\ &\quad (3.52 \cdot 10^{18} - 9.26 \cdot 10^{21} L) s^3 + (1.71 \cdot 10^{21} - 4.49 \cdot 10^{24} L) s^2 \end{aligned} \tag{4.28}$$

and:

$$\begin{aligned} D_{400} &= 2.35 s^9 + 1.17 \cdot 10^4 s^8 + (4.76 \cdot 10^9 L + 5.03 \cdot 10^7) s^7 + \\ &\quad (2.24 \cdot 10^{13} L + 1.29 \cdot 10^{11}) s^6 + (2.09 \cdot 10^{15} L + 2.47 \cdot 10^{14}) s^5 + \\ &\quad (1.01 \cdot 10^{18} L + 3.65 \cdot 10^{17}) s^4 + 1.47 \cdot 10^{20} s^3 + 8.69 \cdot 10^{22} s^2 + \\ &\quad 9.90 \cdot 10^{24} s + 2.80 \cdot 10^{27} \end{aligned} \tag{4.29}$$

With a 400Hz low pass filter in place, the optimal gain, L_{opt} (shown as the trough in Figure 4.14), again varies with frequency, but the variation is less pronounced than in the 200Hz case.

Figure 4.15 shows a comparison of the simulated track position error due to an 80Hz translational external disturbance with and without compensation at $L = L_{opt}$. With the addition of the 400Hz low pass filter, the system cannot perfectly attenuate

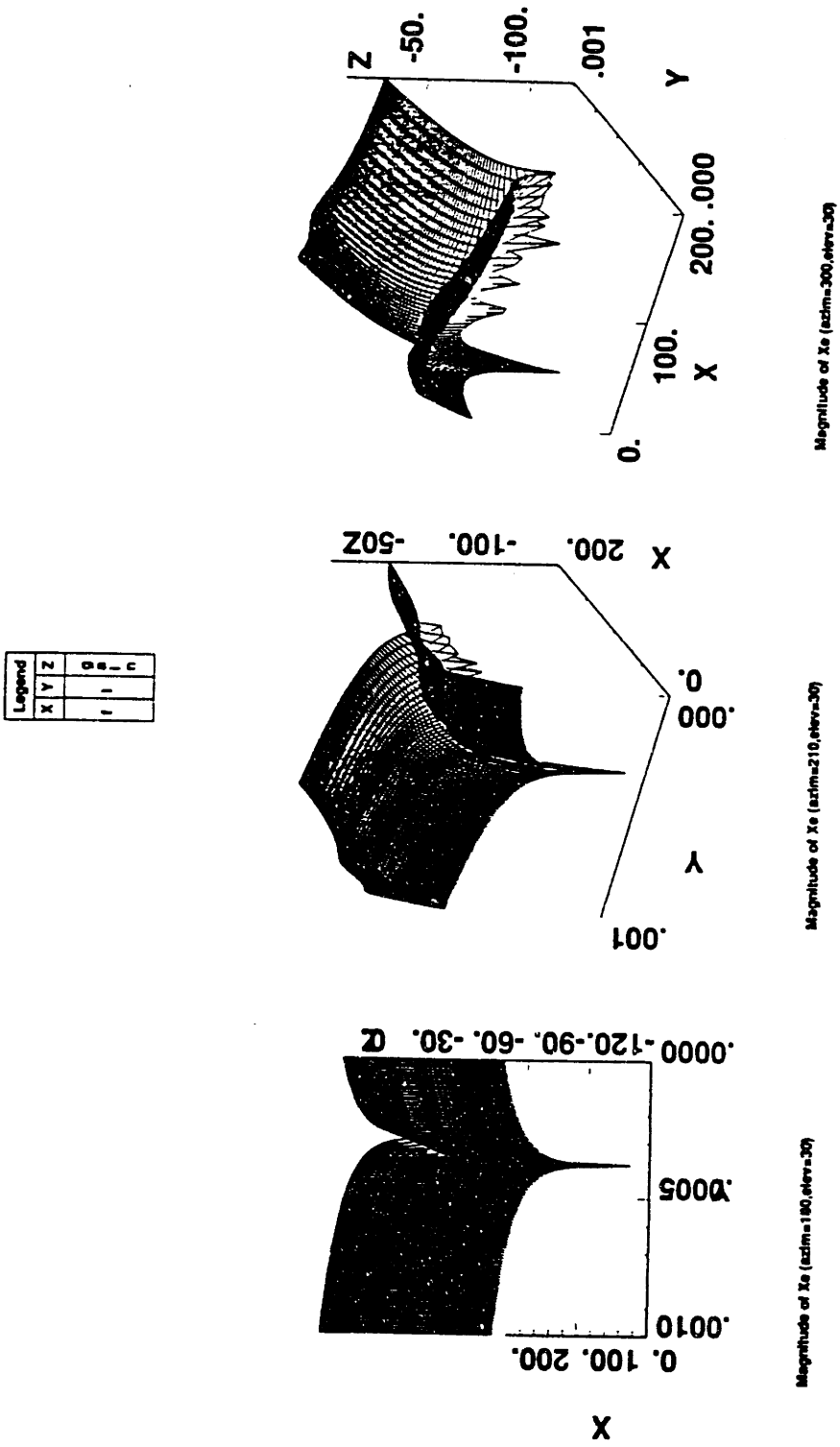

Figure 4.14: Three dimensional view of track position error as a function of gain (L) and input disturbance frequency (400Hz filter).

all position error due to shock vibration and wind-up for all frequencies. At the optimal gain for the unfiltered case, $L = L_{opt}$, the magnitude of the position error caused by an 80Hz sinusoidal external disturbance has decreased by a factor of 3.

Figure 4.16 shows a comparison of simulated track position error due to a 15ms seek with and without compensation at $L = L_{opt}$ for a system with a 400Hz low pass filter. In this case, the position error due to the torque input disturbance (seek) has been decreased by more than a factor of 2, but is not compensated for perfectly as in the unfiltered system.

With the 400Hz low pass filter in the system, the open loop frequency response for the root locus computation becomes:

$$\frac{\ddot{\theta}_{hda}}{L_i} = \frac{I_{act}K_t s^2 T_{36} Q_{400}}{K_p K_t K_{tpd}(C_{det} I_{act} T_{36} + C_{det}) + I_{act} s^2} \tag{4.30}$$

Substituting numerical values into the above equation gives:

$$\frac{\ddot{\theta}_{hda}}{L_i} = \frac{N_{rl400}}{D_{rl400}} \tag{4.31}$$

where (displayed to 3 significant digits):

$$N_{rl400} = 2.02 \cdot 10^9 s^7 + 9.53 \cdot 10^{12} s^6 + 8.87 \cdot 10^{14} s^5 + 4.30 \cdot 10^{17} s^4 \tag{4.32}$$

and:

$$\begin{aligned} D_{rl400} \;=\; & s^9 + 8.49 \cdot 10^3 s^8 + 3.88 \cdot 10^7 s^7 + 1.08 \cdot 10^{11} s^6 + \\ & 1.88 \cdot 10^{14} s^5 + 1.89 \cdot 10^{17} s^4 + 8.27 \cdot 10^{19} s^3 + 3.92 \cdot 10^{22} s^2 + \\ & 4.87 \cdot 10^{24} s + 1.19 \cdot 10^{27} \end{aligned} \tag{4.33}$$

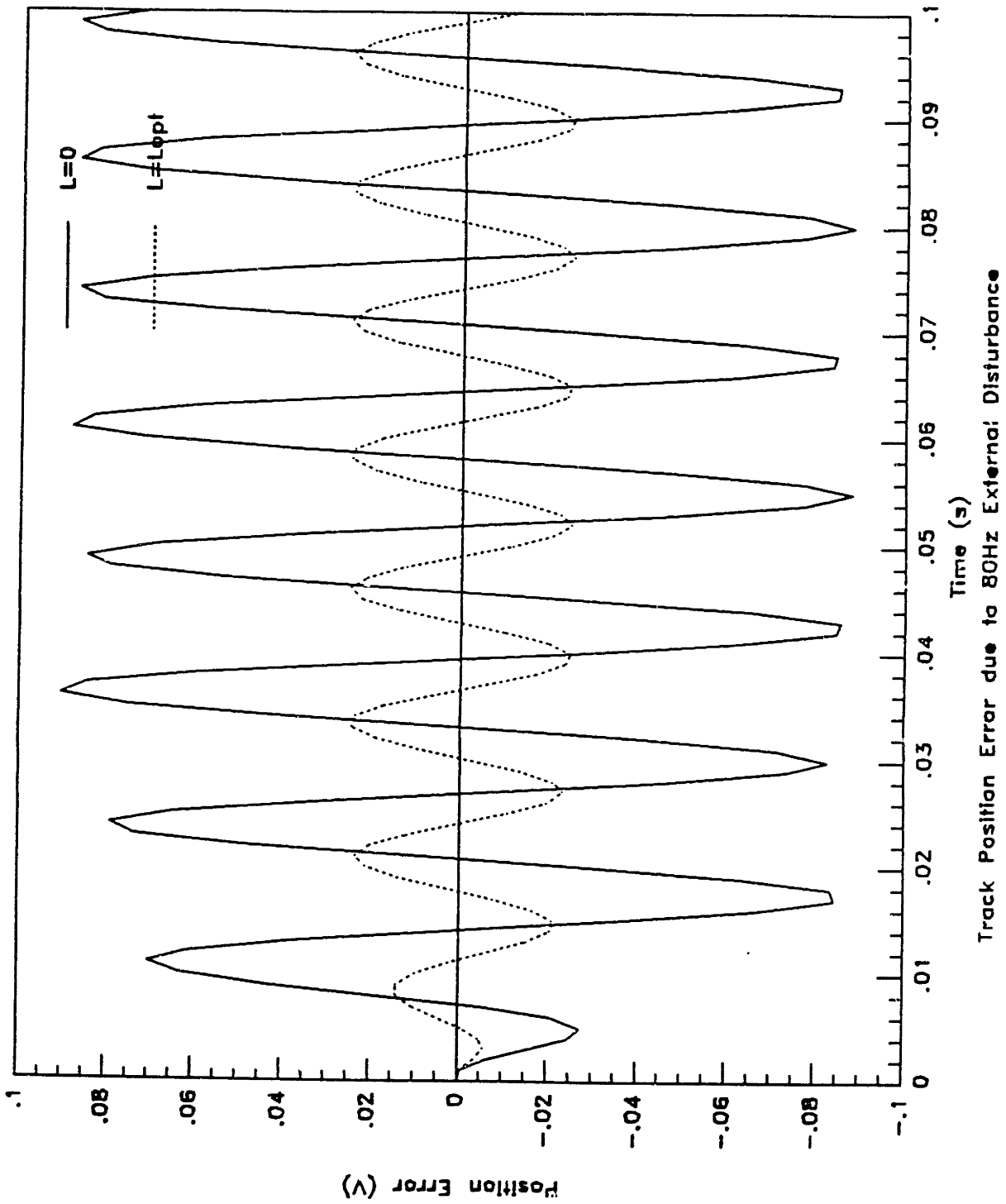

Figure 4.15: Comparison of simulated track position error due to an 80Hz translational external disturbance with and without compensation (400Hz filter).

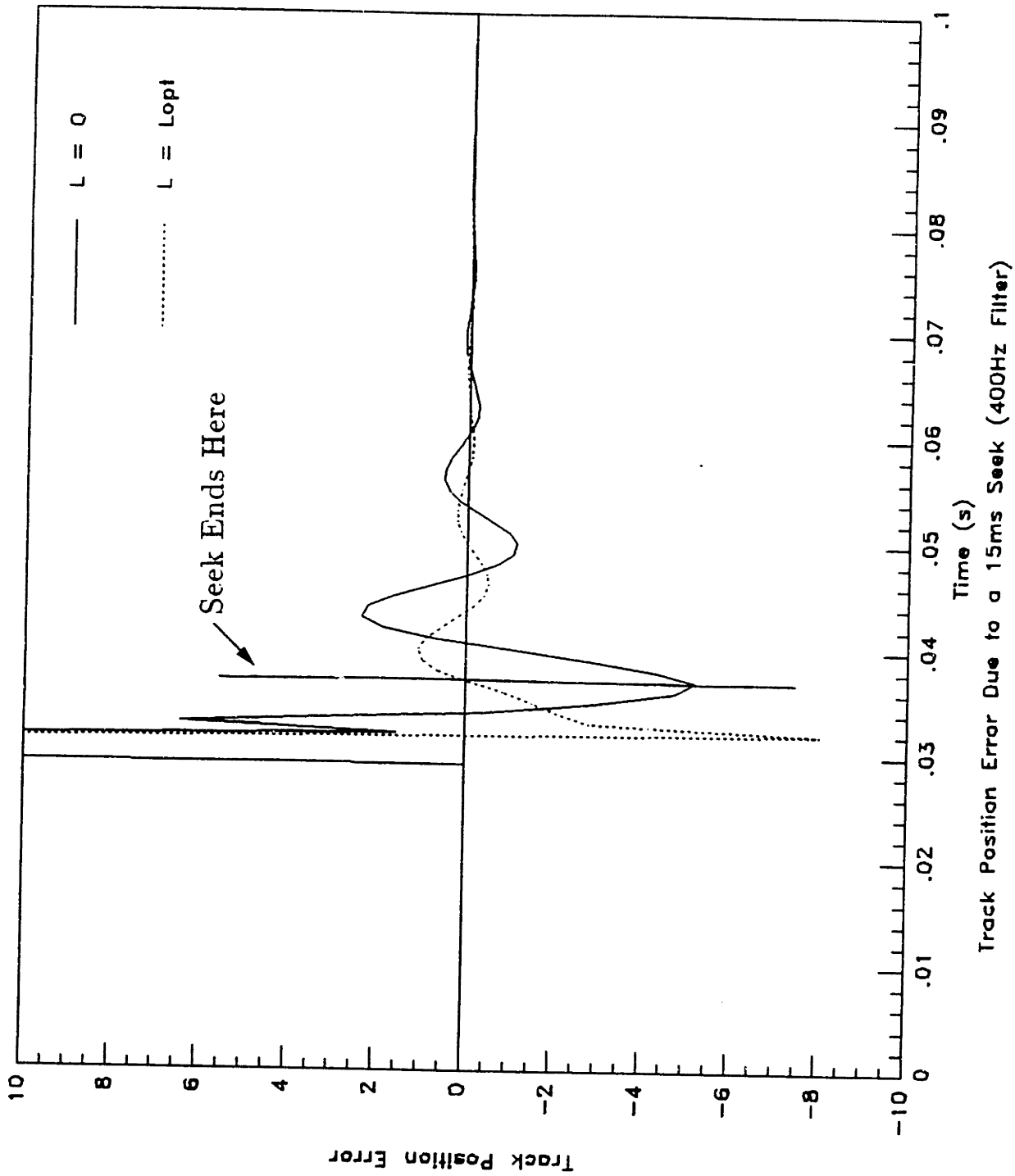

Figure 4.16: Comparison of simulated track position error due to a 15ms seek with and without compensation (400Hz filter).

Table 4.6: Location of poles in the system with a 400Hz low pass filter at the optimal gain.

-38.769	+	206.61i
-38.769	-	206.61i
-118.97	+	473.11i
-118.97	-	473.11i
-1309.4	+	1565.6i
-1309.4	-	1565.6i
-1459.9	+	2856.1i
-1459.9	-	2856.1i
-2634.5		

The 400Hz low pass filter adds two poles to the unfiltered system (1759.29 ± 1794.84). Figure 4.17 shows the system root locus with the 400Hz low pass filter. Figure 4.18 shows the position of all poles on the root locus at $L = L_{opt}$. Table 4.6 shows the location of the poles on the root locus at gain of L_{opt}. By increasing the bandwidth of the filter, the range of stability decreases from $2.0 \cdot 10^{-2}$ (200Hz filter) to $1.67 \cdot 10^{-2}$ (400Hz filter).

4.8 Conclusions

Based on the simulation, a feedback of drive angular acceleration is sufficient to simultaneously correct for external shock, vibration, and wind-up.

If low-pass filtering is required, the filter with the highest allowable cut-off should be used. This choice depends on the proximity of higher order modes of HDA vibration. For the test drive, the 400Hz filter suffices.

Finally, based on the root locus plots, the system has a large range of stabil-

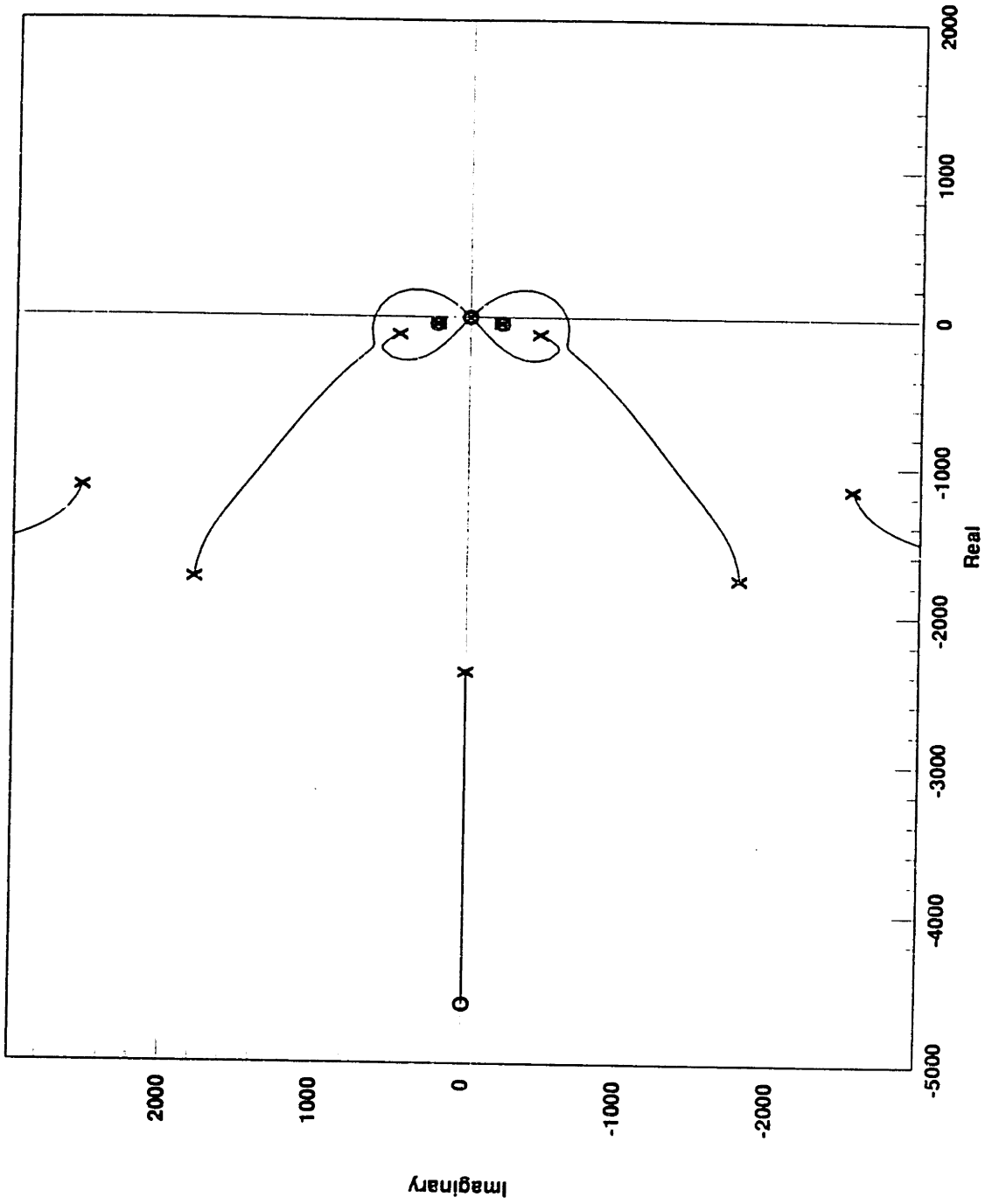

Figure 4.17: Root locus of system (400Hz filter).

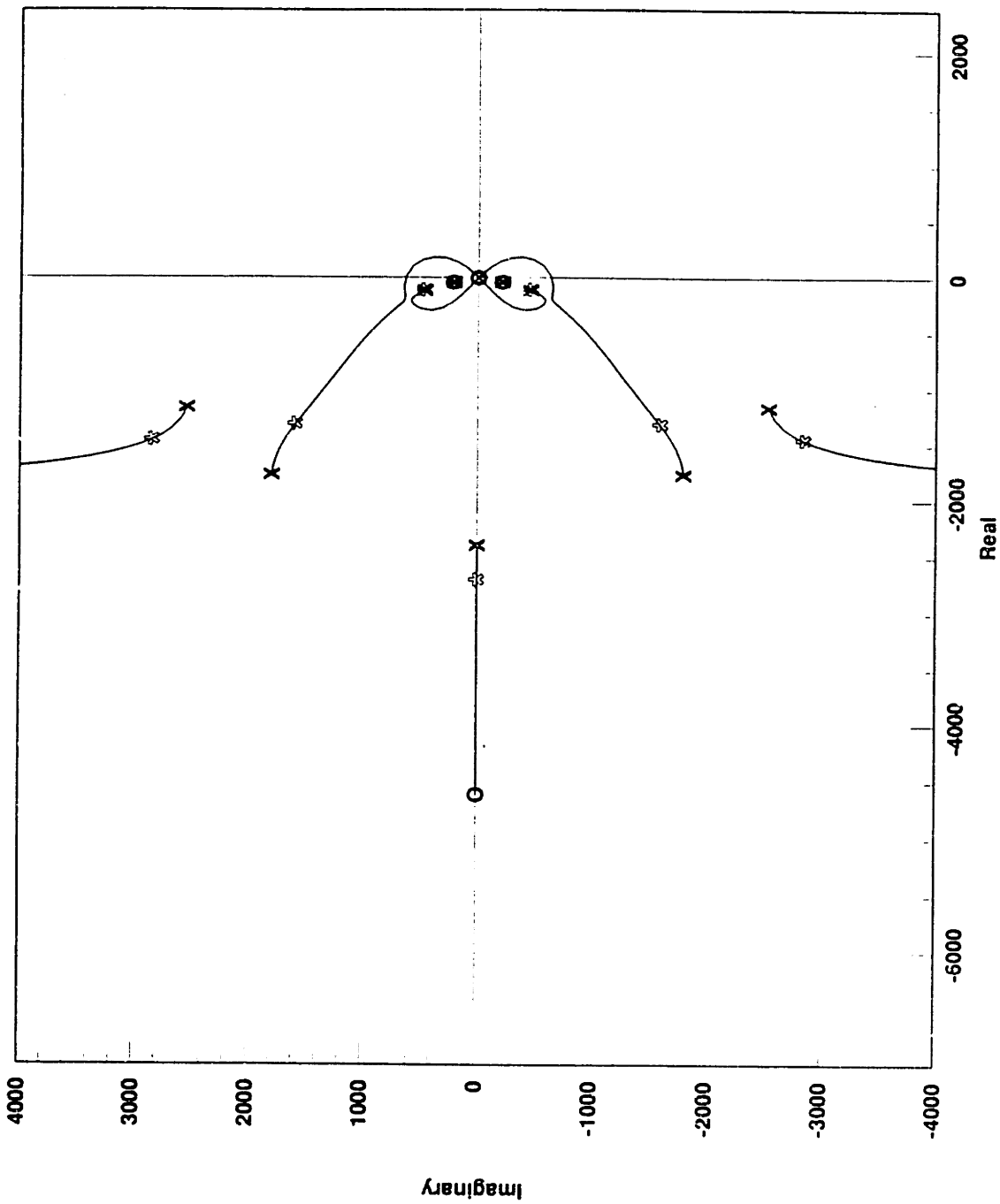

Figure 4.18: Position of poles on root locus at optimal gain (400Hz filter)

ity. Therefore, it should be difficult to destabilize an existing servo system with the introduction of HDA acceleration feedback.

Chapter 5

Experimental ADCS Work

This chapter describes the ADCS laboratory test results.

5.1 Experimental Optimal Gain Determination

The optimal gain for laboratory evaluation of the ADCS was derived using the following equation as discussed in Section 4.4:

$$L_{opt} = \frac{I_{act}}{K_t \cdot Q} \tag{5.1}$$

where I_{act} is the moment of inertia of the actuator ($Kg \cdot m^2$), K_t is the actuator motor torque constant ($\frac{N \cdot m}{amp}$), and Q is the sensor $\frac{s^2 \cdot V}{rad}$[1].

[1]Note: the gain is also fed through the transconductance power amplifier with an assumed gain $\frac{1amp}{1V}$.

5.2 Results

Figure 5.1 shows a comparison plot of the track position error signal with and without the ADCS for a disk drive seek operation 400 tracks in length with the HDA supporting frame rigidly mounted to an aluminum plate. This figure shows a dramatic improvement in disturbance rejection of wind-up. In Figure 5.1, the read/write heads reach their desired track at approximately point (A). At this point, the oscillation of an uncompensated system due to the wind-up is very pronounced. However, in a compensated system, all oscillation due to the wind-up is effectively eliminated. To reach the same settling level initially achieved by the compensated system, the uncompensated system must settle for more than 35 milliseconds.

Figure 5.2 shows a comparison plot with and without ADCS for a 1300 track seek. In this case, the wind-up is not as severe, but the ADCS again effectively attenuates the position error due to the wind-up.

Figure 5.3 shows a plot of track position error versus actuator motor current without active compensation (440 track seek). This plot has been included to show more effectively where the seek operation ends and where the read/write process begins. Figure 5.4 shows a comparison plot of track position error and actuator motor current with the ADCS (440 track seek).

Based on diagnostic software used to evaluate drive performance during manufacturing, the average seek time decreased by more than 10%. By observation, track position error due to wind-up of the HDA is nearly eliminated.

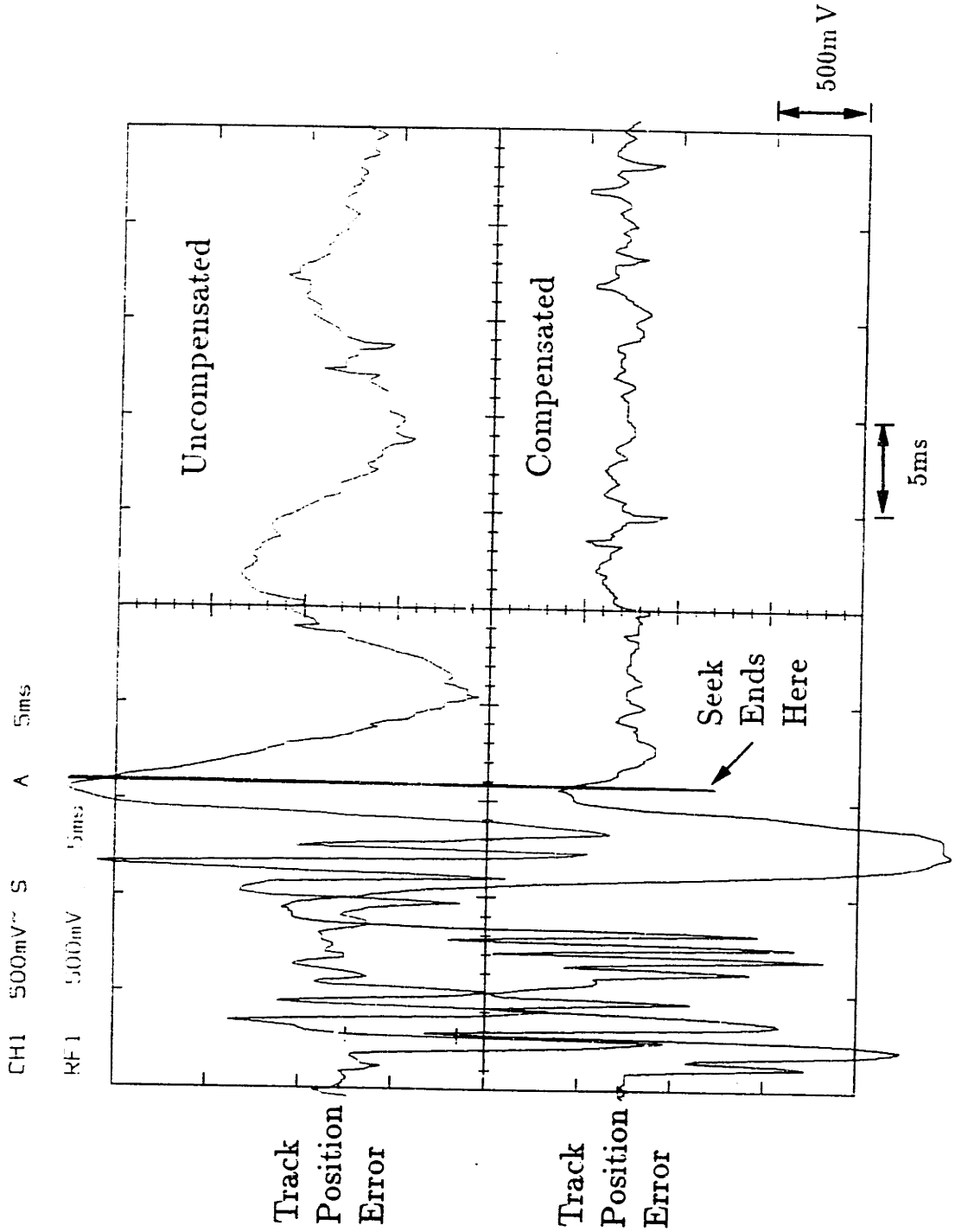

Figure 5.1: Comparison of track position error signal with and without ADCS for a 440 track seek.

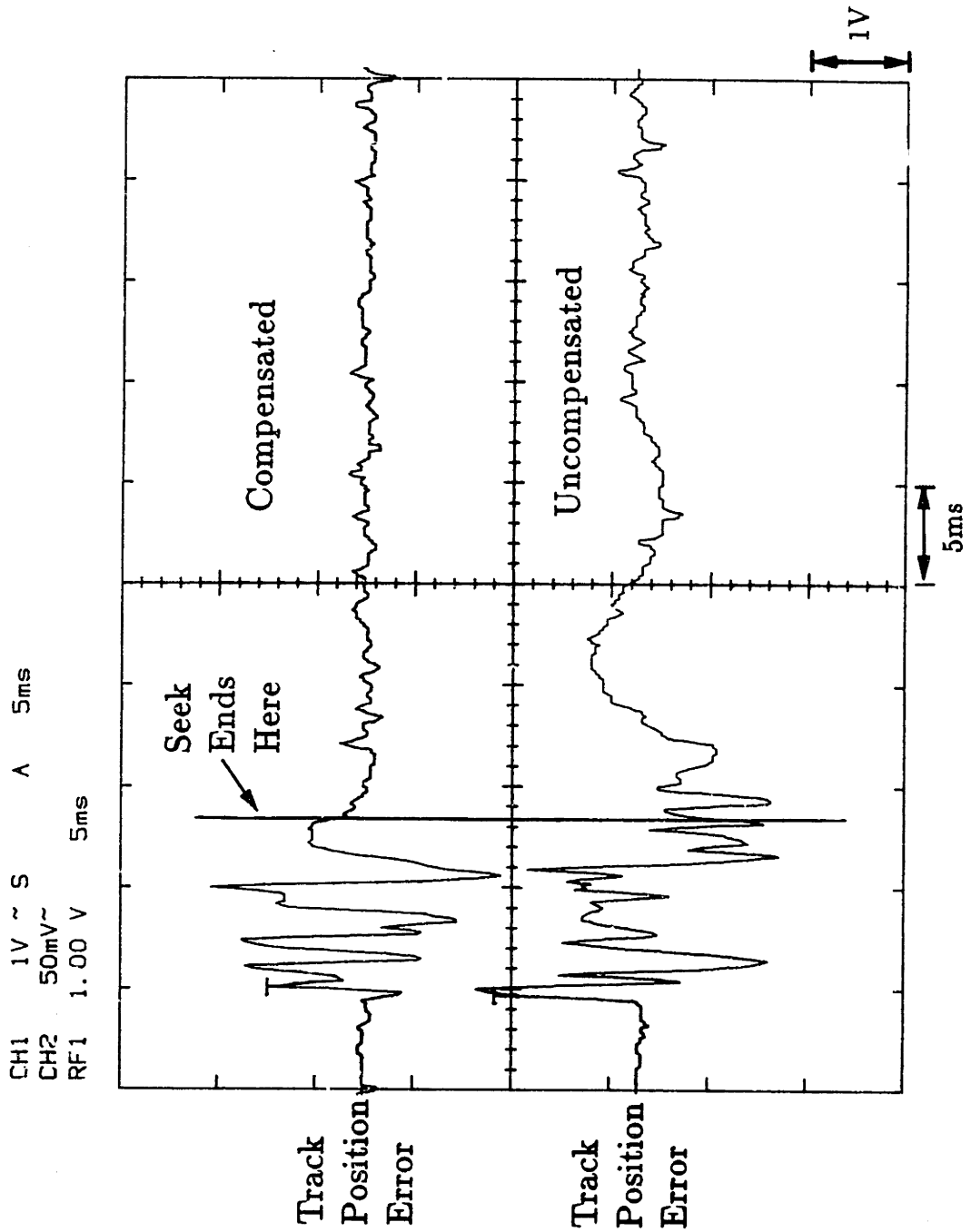

Figure 5.2: Comparison of track position error signal with and without ADCS for a 1300 track seek.

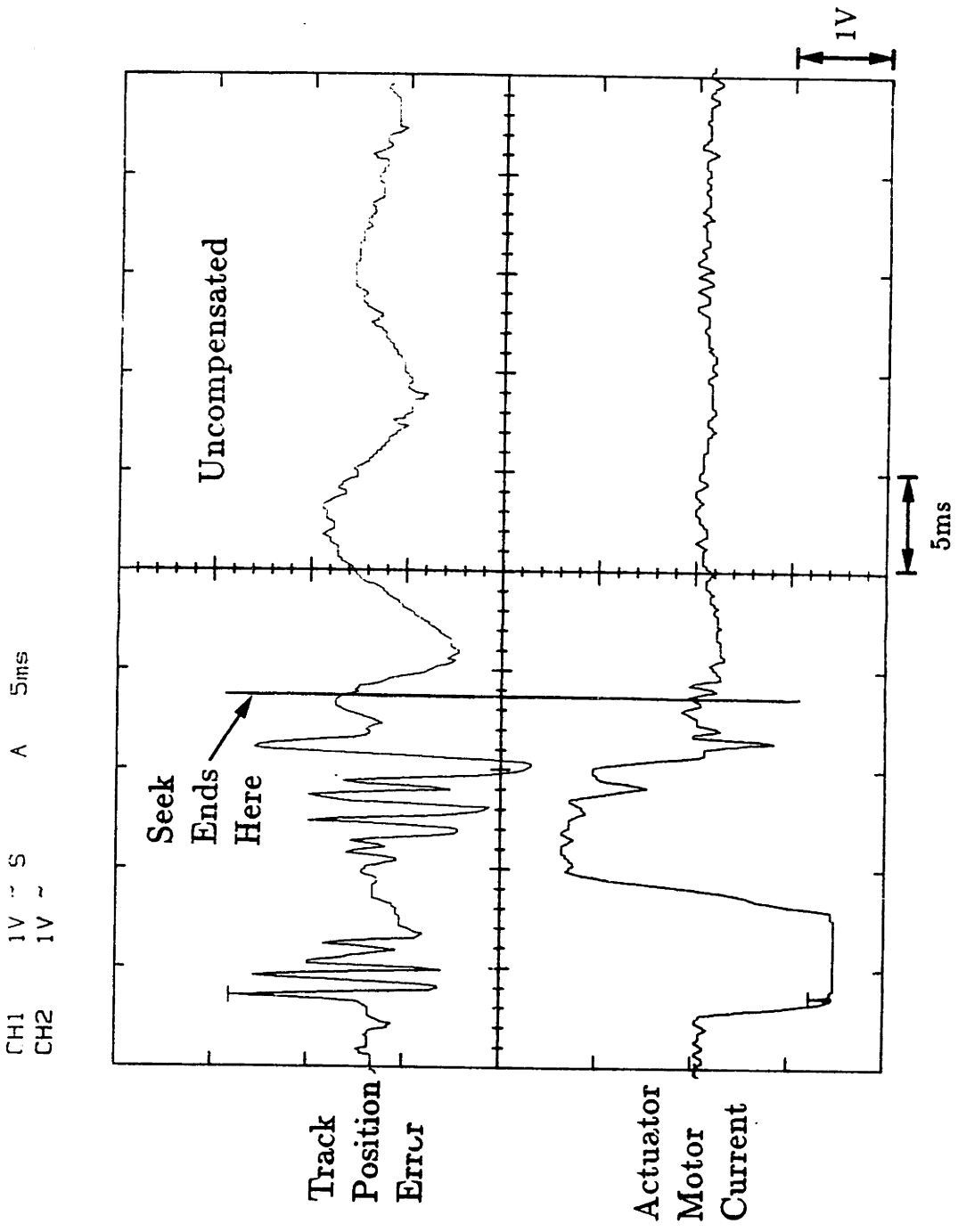

Figure 5.3: Track position error and actuator motor current without acceleration feedback (440 track seek).

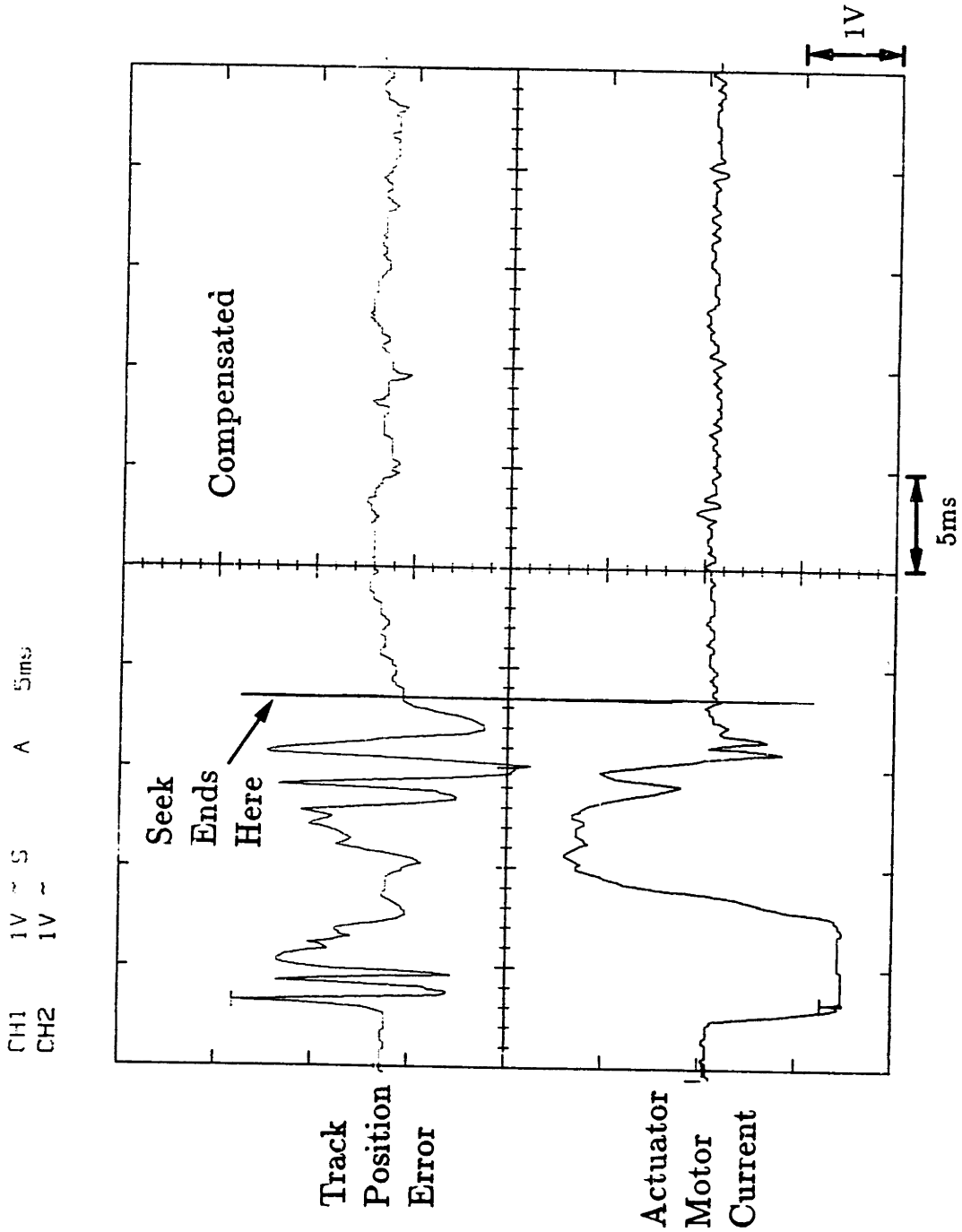

Figure 5.4: Track position error and actuator motor current with acceleration feedback (440 track seek).

Figure 5.5 shows a comparison of track position error due to a calibrated impulse to the HDA internal to the shock mounts. The impulse was applied by the impulse force hammer at a point on the HDA such that the impulse visually maximized position error. This test concludes that the feedback of HDA rotational acceleration is also extremely effective in attenuating position error due to shock and vibration.

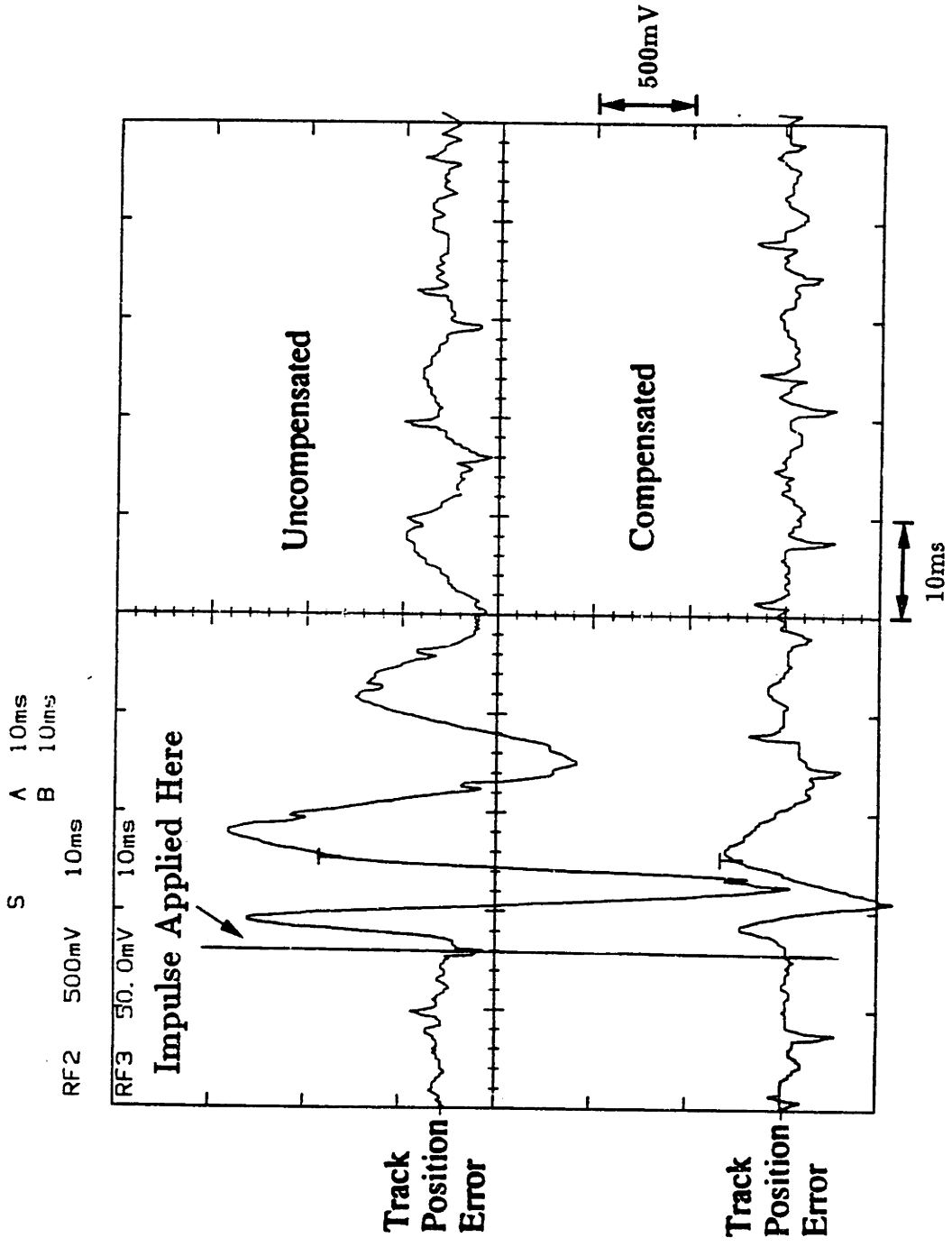

Figure 5.5: Comparison of track position error due to a calibrated impulse to the HDA (internal to the shock mounts).

Chapter 6

Conclusions

Based on the test results, the feedback of HDA angular acceleration is extremely effective in simultaneously compensating the read/write heads positioning servo system for track position error due to shock, vibration, and wind-up. In a *worst case* situation of a rigidly mounted supporting frame, average seek times are improved by more than 10% with track position error due to shock, vibration, and wind-up nearly eliminated.

As discussed in Section 4.4, the optimal feedback gain, L_{opt}, depends only on the moment of inertia of the actuator, I_{act}, the actuator torque constant, K_t, and the accelerometer characteristics, Q, as given by the relationship:

$$L_{opt} = \frac{I_{act}}{K_t Q} \tag{6.1}$$

Surprisingly, the active system is independent of the dynamics of the HDA, in-

cluding the mass of the HDA, the moment of inertia of the HDA, the shock mount stiffness, the shock mount damping, and the offset center of mass.

Therefore, the developed system can be simply adapted based on the above equation to function on any similar drive of the balanced, rotary-actuator design. This is desirable as the modeling and computer simulation of the active system can be a long and complex process.

6.1 Suggestions for Future Work

In developing an ADCS on a manufacturing level, consistency is critical. The optimal gain for an ADCS is based on the actuator torque constant, the moment of inertia of the HDA, and the accelerometer characteristics. If variations occur in any of these areas, the optimal gain must be varied to maintain drive performance. Therefore, a tolerance control on accelerometer gain may be required at a minimum to bring this type of system to a manufacturing level.

Appendix A

Hardware Specifications

MINIATURE 1 GRAM

QUARTZ ACCELEROMETER

Model 309A

PCB PIEZOTRONICS

about the size of a pencil eraser

- **small size, one gram**
- **low impedance, 5mV/g output**
- **resolution independent of cable length**
- **frequency range to 25 000 Hz**
- **with repairable, integral 6 ft cable**

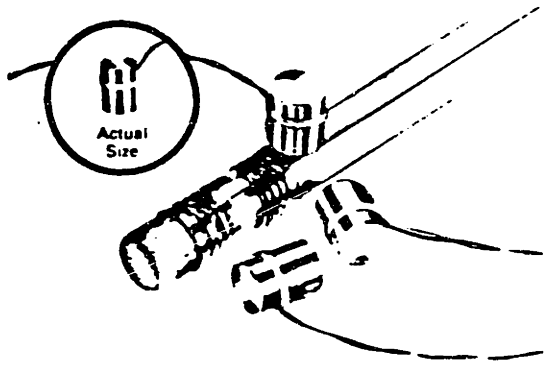

For vibration and shock measurements on PC boards and other lightweight structures requiring a low mass accelerometer and very high frequency response.

Model 309A Quartz Accelerometer was designed specifically for minimum size and weight. A built-in microelectronic amplifier converts the high impedance charge signal from the quartz crystal element into a high voltage, low impedance output signal capable of driving long cables without degradation of the high quality signal. This overcomes the signal/noise problem common to most miniature accelerometers.

The 309A is structured with naturally polarized compression mode quartz elements and a microelectronic amplifier housed in a lightweight metal case. Unlike other low mass accelerometers, the integral 6 foot, two conductor twisted cable is customer repairable. The cable terminates in a 10-32 micro connector for coupling to an extension cable and/or PCB constant current power unit. Adhesive mounting is recommended using a thin coat of the Petro Wax supplied with the accelerometer.

PCB offers a complete selection of low cost battery or line power units, with or without gain, in single or multichannel configurations to meet your system requirements. Several FFT analyzers now incorporate the correct power circuit for direct connection to PCB accelerometers.

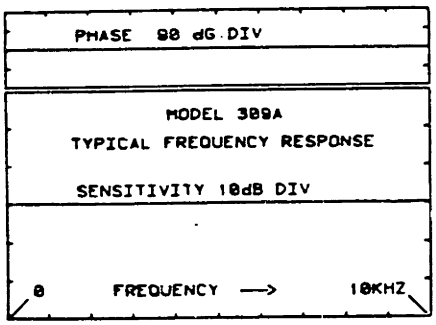

SPECIFICATIONS: Model No		309A
Range (for ±5V output)	g	1000
Resolution	g	0.02
Sensitivity (nominal)	mV/g	5
Resonant Frequency (Mtd.)	Hz	120000
Frequency Range (±5%)	Hz	5-10000
Frequency Range (±10%)	Hz	3 to 25000
Discharge Time Constant	s	0.1
Amplitude Linearity	%FS	1
Polarity		positive
Output Impedance	ohm	<100
Output Bias (nominal)	V	11
Overload Recovery	μs	10
Transverse Sensitivity	%	5
Temperature Range	°F	-40 to +150
Temp Coefficient	%/°F	0.05
Vibration (max)	g	1000
Shock (max)	g	2000
Size (dia x height)	in	.23 x .30
Case Material		SS
Weight	gm	1.0
Cable, 2 wire	ft	6
Termination	micro	10-32
Excitation (Constant Current)	mA	2 to 20
Voltage to Current Regulator	VDC	+18 to 28
Accessories:		**Model No.**
Mounting wax (supplied)		080A24

TYPICAL SYSTEM: K308A battery power kit is shown below. Also available as GK309A with gain X1, X10, X100. Recharge and long life external battery pack options available.

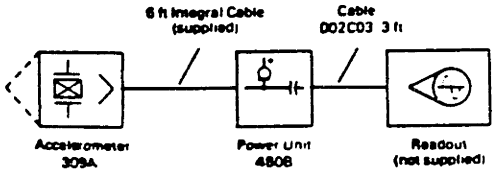

DIMENSIONS:

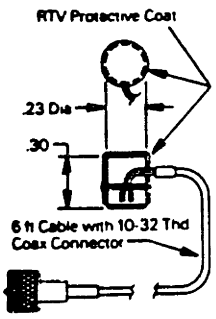

309184

PCB PIEZOTRONICS, INC. 3425 WALDEN AVENUE DEPEW NEW YORK 14043-2495 TELEPHONE 716-684-0001 TWX 710-263-1371

AMPLIFYING

BATTERY POWER UNIT

Model 480D06

PCB PIEZOTRONICS

- amplifies signals X1, 10 or 100
- operates from 27V extending range of many ICP transducers to 10 volts
- includes connector for external power option
- includes connector for charger option

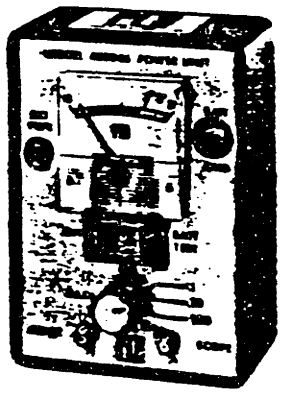

Model 488B Battery Charger with 3 NiCd Batteries (optional)

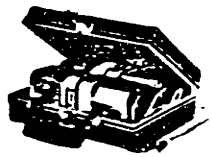

Model 073A05 long life, external Battery Pack (optional)

For use with low impedance (ICP) piezoelectric transducers, model 480D06 functions to power the transducer electronics, amplify the signal, debias the output signal and indicate normal or faulty system operation. It is a combination power supply and signal amplifier.

New model 480D06 features +27 volt power, provided by three standard 9 volt alkaline transistor radio batteries connected in series, to extend the dynamic range of many ICP transducers to 10 volts output. Other features include an external DC power jack for use with optional long life (1 year) battery pack model 073A05 and a battery charge jack for use with Model 488B Battery Charger/NiCd Battery option. If this option is ordered with the 480D06, NiCd instead of alkaline batteries will be provided. A decoupling capacitor located behind the output connector removes DC bias on the output signal and provides a drift free A.C. mode of operation. The self-test meter circuit, monitoring bias on the signal, indicates normal operation (green), short (red), or open circuit (yellow). It also checks battery voltage (+27V) when the rocker switch is depressed to the right. Circuits are housed in a shielded plastic case with a metal panel. Connectors are coaxial micro 10-32 jacks. Options and accessories include the following by model number:

480D09 - Power Unit with BNC connectors
480D06/488B - Power Unit with NiCd batteries and charger
488B - Charger with 3 NiCd batteries
073A09 - NiCd rechargeable battery
073A05 - Long life external battery pack

Sensor kits including Model 480D06 Power Unit simplify specifying and ordering. These kits contain the sensor (transducer), sensor cable (10 ft. long), power unit, scope cable (3 ft. long terminated in BNC) and accessories. To specify, add prefix GK to the sensor model number and add prefix cost to the sensor price. Use prefix GKR to specify kit with NiCd battery and charger option, e.g. GKR302A Accelerometer Kit.

SPECIFICATIONS: Model No.		480D06
Transducer Excitation	VDC	+27
Excitation Current	mA	2
Voltage Gain (selectable)	x	1, 10, 100
Coupling Capacitor	μF	22
Frequency Range (±5%)(1)	Hz	0.15 to 100 000
Output Signal	V	+10, -5
Noise Output (PK to PK) X1	mV	0.2
X10	mV	2
X100	mV	20
D.C. Offset (into 1 Megohm)	mV	30
Connectors	micro	10-32
Meter	VFS	27
Size (L, W, H)	in	1.8x2.9x4
Weight	oz (gm)	15 (425)
Batteries (three 9V alkaline)	V	27
Battery Life	hr	40

(1) Low frequency is specified into 1 megohm load

TYPICAL SYSTEM (GK kit)

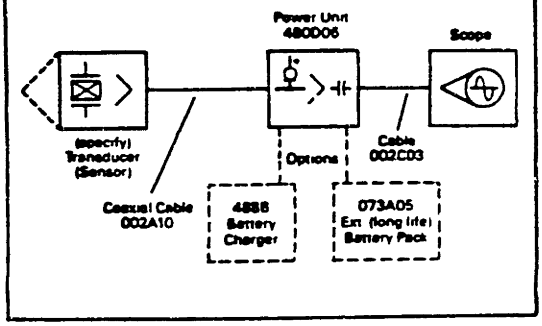

CIRCUIT

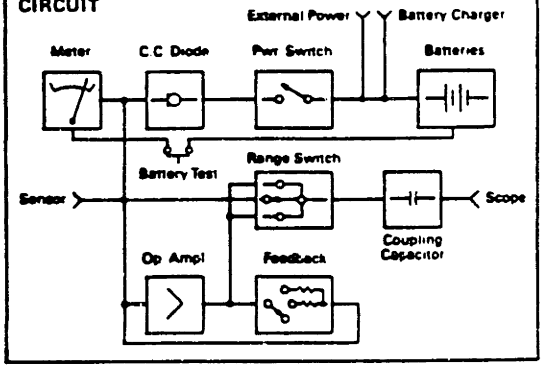

480D0203

PCB PIEZOTRONICS

SPECIFICATIONS

IMPULSE HAMMER

REVISIONS

MODEL NO.		086B01	086B02	086B03
FREQUENCY RANGE	kHz	10.0	8.0	8.0
HAMMER RANGE (EV OUTPUT)	lb_F(N)	100 (440)	100 (440)	500 (2200)
HAMMER SENSITIVITY (APPROX)	mV/lb_F(mV/N)	50 (12)	50 (12)	10 (2.3)
RESONANT FREQUENCY	kHz	31	31	31
HAMMER MASS	lb(Kg)	0.2 (.09)	0.3 (.14)	0.3 (.14)
HEAD DIAMETER	in(cm)	0.6 (1.5)	0.6 (1.5)	0.6 (1.5)
TIP DIAMETER	in(cm)	0.25 (.63)	0.25 (.63)	0.25 (.63)
HANDLE LENGTH	in(cm)	8.0 (20.3)	8.0 (20.3)	8.0 (20.3)
CONNECTOR (COAXIAL)	thd	10-32	10-32	10-32
CABLE (COAXIAL)	MOD NO	002A10	002A10	002A10
TIP SUPERSOFT	MOD NO	084B11	084B11	084B11
TIP SOFT	MOD NO	084B05	084B05	084B05
TIP MEDIUM	MOD NO	084B04	084B04	084B04
TIP HARD	MOD NO	084B03	084B03	084B03
TIP COVER	MOD NO	085A10	085A10	085A10
EXTENDER	MOD NO (MAT'L)	084A06(AL)	084A08(STL)	084A08(STL)
STUD MOUNTING	MOD NO	081B05	081B05	081B05
CASE	MOD NO	001A02	001A02	001A02

SUPPLIED ACCESSORIES:

MOD NO 070A02 ADAPTOR (1)
MOD NO 007T05 CABLE (1)
MOD NO 081B05 STUD (1)
MOD NO 085A10 TIP COVER (2)
MOD NO 085A07 TIP INSERT (4)
MOD NO 085A03 TIP INSERT (4)

APP'D	RICE	1/19/83	SPEC No
ENGR			086-2010-80
SALES	SHJL	1/19/83	

KD-2810 Series Specifications

(Values are typical for flat aluminum and will vary for other metals)

TARGET MATERIAL		
Non-Magnetic	Yes	
Magnetic	No	
MEASURING RANGE*		
+ Offset of 10,000	1000	μ inch
+ Offset of 250 μm	.25	μm
LINEARITY		
Within ± 1%	10	± μinch
	0.25	±μm
REPEATABILITY		
	0 1	μ inch
	0.0025	μm
RESOLUTION		
Static	0.1	μ inch
	0.0025	μm
SENSITIVITY		
	1	mV/μ inch
	40	mV/μm
FREQUENCY RESPONSE	Static to 10	kHz (-3 dB pt.)
OUTPUT, FULL RANGE		
Voltage, Analog	1.000	Vdc (Eng.)
	-1.000	Vdc (Met.)
Current	15 Max	mA
Impedance	< 5	ohms

* Customer Adjustable to ± 500 Microinches (± 12.5 μm) Measuring Range.

TEMPERATURE

Thermal Sensitivity Shift

Sensor, Cable and Electronics: <±1μ inch/°F (<± 0.05 μm/°C)

Operating Temperature Range

Sensor, Cable and Electronics: 50°F to 100°F (10°C to 38°C)

Storage Temperature

Sensor, Cable and Electronics: -67°F to 200°F (-55°C to 93°C)

POWER SUPPLY REQUIREMENTS

Voltage	Plus and Minus 15 Vdc
Voltage Regulation	± 0.5 Vdc
Current	55 mA Typical

Operating Principle*

The system uses a principle of impedance variation caused by eddy currents induced in a conductive nonmagnetic metal target material. The coupling between a coil in the sensor and a target is dependent upon their diplacement (gap).

The sensor cable transmits the signal between the sensor and electronics. The electronics package consists of an oscillator, amplifiers, and a demodulator that provide an analog voltage directly proportional to displacement.

*Patent Pending

Accessories

Recommended accessories for ease of system calibration and convenience are listed below:

- Power Supply: P-3500 with digital readout, to provide regulated + and - 15Vdc output for up to 6 systems. Input voltage is selectable 110, 120, 220, 240 Vac. Part No. 852077-001.
- Power and Output Cable: 10 ft. (3.1 m) Part No. 850874-010.
- Synchronization Kit: Includes a one foot interconnecting cable and tee. Part No. 850897-001.

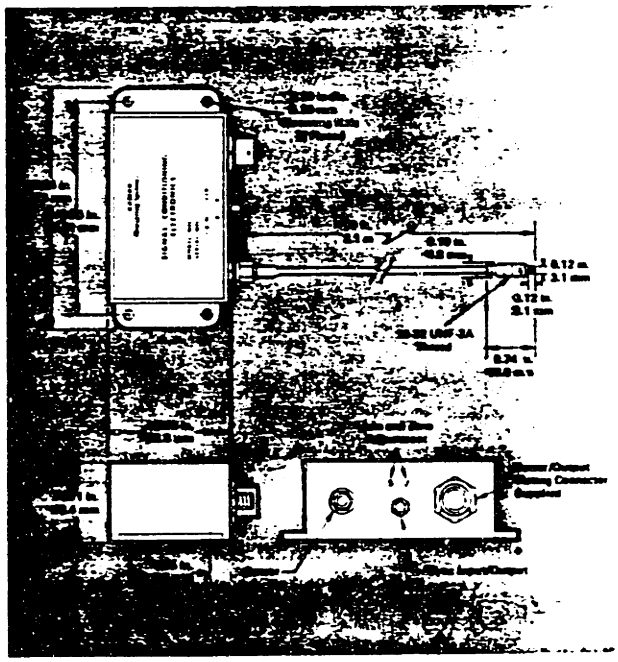

ORDERING INFORMATION: Specify by model number and desired options. All specifications are subject to change without notice.

Appendix C

HP 3562A SPECIFICATIONS

Specifications describe the instrument's warranted performance. Supplemental characteristics are intended to provide information useful in applying the instrument by giving typical, but non-warranted, performance specifications. Supplemental characteristics are denoted as 'typical,' 'nominal,' or 'approximately.'

Frequency

Measurement Range: 64 μHz to 100 kHz, both channels, single- or dual-channel operation

Accuracy: ± 0.004% of frequency reading

Resolution: Span/800, both channels, single- or dual-channel operation, Linear Resolution mode

Spans:	Baseband	Zoom
# of spans	66	65
min span	10.24 mHz	20.48 mHz
max span	100 kHz	100 kHz
time record (Sec)	800/span	800/span

Window Functions: Flat Top, Hann, Uniform, Force, Exponential and User-Defined

Window Parameters:	Flat Top	Hann	Uniform
Noise Equiv BW (% of span)	0.478	0.188	0.125
3 dB BW (% of span)	0.45	0.185	0.125
Shape factor (60 dB BW/3 dB BW)	2.6	9.1	716

Typical Real Time Bandwidths:

Single-channel, single display	2.5 kHz
Single-channel, Fast Averaging	10 kHz
Dual-channel, single display	2 kHz
Dual-channel, Fast Averaging	5 kHz
Throughput to CS/80 disc	
Single-channel	10 kHz
Dual-channel	5 kHz

Amplitude

Accuracy: Defined as Full Scale Accuracy at any of the 801 calculated frequency points. Overall accuracy is the sum of absolute accuracy, window flatness and noise level.

Absolute Accuracy:
Single Channel (Channel 1 or Channel 2)
± 0.15 dB ± 0.015% of input range (+ 27 dBV to − 40 dBV, input connections as specified in Cases 1 and 2 below)
± 0.25 dB ± 0.025% of input range (− 41 dBV to − 51 dBV, input connections as specified in Cases 1 and 2 below)

DC Response: Auto-Cal and Auto-Zero on

Input Range (dBV rms)	dc Level
+ 27 to − 35	> 30 dB below full scale
− 36 to − 51	> 20 dB below ful scale

Frequency Response Channel Match:
± 0.1 dB, ± 0.5 degree (input connections as specified in Cases 1 and 2 below)

Input Connections:
Cases 1 and 2 are the recommended input connections. For these cases, the amplitude accuracy specified above is applicable.

Case 1

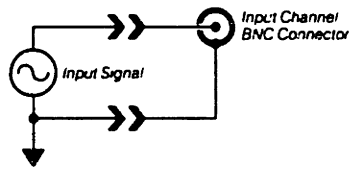

Case 2

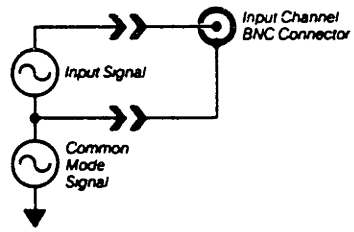

Cases 3 and 4 are input connections which degrade amplitude accuracy. For these cases, the amplitude accuracy specified above must be modified with the accuracy adders stated below.

Case 3

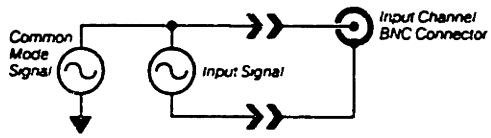

Case 4

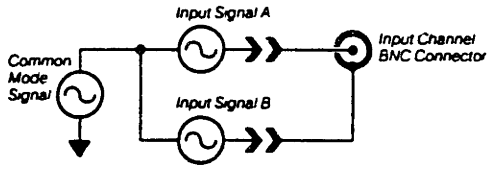

Accuracy Adder: Single-channel, inputs connected as shown in Cases 3 and 4 above.
Add ± 0.35 dB and ± 4.0 degrees to the absolute accuracy.

Accuracy Adder: Dual-channel measurements
Add ± 0.35 dB and ± 4.0 degrees once for each input connected as shown in Cases 3 and 4 above.

Window Flatness:

Flat Top:	+0, −0.01 dB
Hann:	+0, −1.5 dB
Uniform:	+0, −4.0

Noise Floor: Flat top window, 50 Ω source impedance, −51 dBV range
20 Hz to 1 kHz (1 kHz span) < −126 dBV (−134 dBV/√Hz)
1 kHz to 100 kHz (100 kHz span) < −116 dBV
(−144 dBV/√Hz)

Dynamic Range: All distortion (intermodulation and harmonic), spurious and alias products ≥ 80 dB below full scale input range (16 averages) < 10KΩ termination

Phase

Accuracy: Single channel, input connections as specified above in Cases 1 and 2, referenced to trigger point.

< 10 kHz	± 2.5 degrees
10 kHz to 100 kHz	± 12.0 degrees

Inputs

Input Impedance: 1 MΩ ± 5% shunted by < 100 pF

Input Coupling: The inputs may be ac or dc coupled; ac rolloff is < 3 dB at 1 Hz

Crosstalk: −140 dB (50 Ω source, 50 Ω input termination, input connectors shielded)

Common Mode Rejection:

0 Hz to 66 Hz	80 dB
66 Hz to 500 Hz	65 dB

Common Mode Voltage: dc to 500 Hz

Input Range (dBV rms)	Maximum (ac + dc)
+27 to −12	± 42.0 Vpeak
−13 to −51	± 18.0 Vpeak*

*For the −43 to −51 dBV input ranges, common mode signal levels cannot exceed ± 18 Vpeak or (Input Range) + (Common Mode Rejection), whichever is the lesser level.

Common Mode Voltage: 500 Hz to 100 kHz. The ac part of the signal is limited to 42 Vpeak or (Input Range) + (10 dB), whichever is the lesser level

Common Mode Distortion: For the levels specified, distortion of common mode signals will be less than the level of the rejected common mode signal.

External Trigger Input Impedance: Typically 50 kΩ ± 5%

External Sampling Input: TTL compatible input for signals ≤ 256 kHz (nominal maximum sample rate).

External Reference Input:
Input Frequencies: 1, 2, 5 or 10 MHz ± 0.01%
Amplitude Range: 0 dBm to + 20 dBm (50 Ω)

Trigger

Trigger Modes: Free Run, Input Channel 1, Input Channel 2, Source and External Trigger. Free Run applies to all Measurement Modes; Input Channel 1, Input Channel 2, Source and External Trigger apply to the Linear Resolution, Time Capture and Time Throughput measurement modes.

Trigger Conditions:
Free Run: A new measurement is initiated by the completion of the previous measurement.

Input: A new measurement is initiated when the input signal to either Channel 1 or Channel 2 meets the specified trigger conditions. Trigger Level range is ± 100% of Full Scale Input Range; Trigger Level is user-selected in steps of (Input Range in volts)/128.

Source: Measurements are synchronized with the periodic signal types (burst random, sine chirp and burst chirp).

External: A new measurement is initiated by a signal applied to the front panel External Trigger input. Trigger Level range is ± 10 Vpeak; Trigger Level is user selected in 80 mV steps.

Trigger Delay:
Pre-Trigger: The measurement can be based on data from 1 to 4096 samples (1/2048 to 2 time records) prior to trigger conditions being met. Resolution is 1 sample (1/2048 of a time record).

Post-Trigger: The measurement is initiated from 1 to 65,536 samples (1/2048 to 32 time records) after the trigger conditions are met. Resolution is 1 sample (1/2048 of a time record).

Source

Band limited, band translated random noise, burst random, sine chirp, burst chirp, as well as fixed sine and swept sine signals are available from the front panel Source output. DC Offset is also user-selectable

Output Impedance: 50 Ω (nominal)

Output Level: ≤ ± 10 Vpeak (ac + dc) into a ≥ 10 kΩ, < 1000 pF load. Maximum current = 50 mA.

AC Level: ± 5 Vpeak (≥ 10kΩ, < 1000 pF load)

DC Offset: ± 10 Vpeak in 100 mV steps. Residual offset at 0 V offset ≤ 10 mV.

% In-Band Energy: (1 kHz span, 5 kHz center frequency)
Random Noise: 70%
Sine Chirp: 85%

Accuracy and Purity: Fixed or Swept Sine
Flatness: ± 1 dB (0 to 65 kHz),
+ 1, − 1.5 dB (65 kHz to 100 kHz)

Distortion: (including subharmonics)

dc to 10 kHz	− 60 dB
10 kHz to 100 kHz	− 40 dB

General

Specifications apply when AUTO CAL is enabled, or within 5°C and 2 hrs of last internal calibration (except for transient environmental changes).

Ambient temperature: 0° to 55° C.
Relative Humidity: ≤ 95% at 40°C
Altitude: 4,572 m (15,000 ft)

Storage:
Temperature: − 40° to + 75°C.
Altitude: ≤ 15,240m (50,000 ft)

Power:
115 VAC + 10% — 25%, 48 to 440 Hz
230 VAC + 10% — 25%, 48 to 66 Hz
450 VA maximum

Weight:
26 kg (56 lbs) net
35 kg (77 lbs) shipping

Dimensions:
222 mm (8.75 in) high
426 mm (16.75 in) wide
578 mm (22.75 in) deep

HP-IB:
Implementation of IEEE Std 488-1978
SH1 AH1 T5 TE0 L4 LE0 SR1 RL1 PP0 DC1 DT1 C0
Supports the 91XX and 794X families of HP disc drives as well as Hewlett-Packard Graphics Language (HP-GL) digital plotters.

Appendix B

Transfer Function Matrix

The following are the numerical values for the transfer function matrix discussed in Section 3.6.1.

$$T_{11} = \frac{9.4 \cdot 10^{1} s^5 + 8.2 \cdot 10^{4} s^4 + 4.6 \cdot 10^{7} s^3 + 1.9 \cdot 10^{10} s^2 + 2.7 \cdot 10^{12} s + 5.9 \cdot 10^{14}}{s^6 + 4.3 \cdot 10^{2} s^5 + 4.1 \cdot 10^{5} s^4 + 8.0 \cdot 10^{7} s^3 + 3.1 \cdot 10^{10} s^2 + 2.7 \cdot 10^{12} s + 5.9 \cdot 10^{14}} \quad \text{(B.1)}$$

$$T_{12} = \frac{3.5 s^5 + 4.4 \cdot 10^{2} s^4 - 1.3 \cdot 10^{6} s^3 - 6.2 \cdot 10^{8} s^2}{s^6 + 4.3 \cdot 10^{2} s^5 + 4.1 \cdot 10^{5} s^4 + 8.0 \cdot 10^{7} s^3 + 3.1 \cdot 10^{10} s^2 + 2.7 \cdot 10^{12} s + 5.9 \cdot 10^{14}} \quad \text{(B.2)}$$

$$T_{13} = \frac{1.2 s^3 + 1.2 \cdot 10^{3} s^2}{s^4 + 3.4 \cdot 10^{2} s^3 + 3.3 \cdot 10^{5} s^2 3.3 \cdot 10^{7} s 1.1 \cdot 10^{10}} \quad \text{(B.3)}$$

$$T_{14} = \frac{4.2 \cdot 10^{-1} s^6 + 1.3 \cdot 10^{2} s^5 + 1.3 \cdot 10^{5} s^4 + 1.3 \cdot 10^{7} s^3 + 4.8 \cdot 10^{9} s^2}{s^6 + 4.3 \cdot 10^{2} s^5 + 4.1 \cdot 10^{5} s^4 + 8.0 \cdot 10^{7} s^5 + 3.1 \cdot 10^{10} s^2 + 2.7 \cdot 10^{12} s + 5.9 \cdot 10^{14}} \quad \text{(B.4)}$$

$$T_{15} = \frac{3.0 \cdot 10^{-2} s^6 + 1.4 s^5 + 1.3 \cdot 10^3 s^4 + 5.4 \cdot 10^5 s^3 + 2.4 \cdot 10^8 s^2}{s^6 + 4.3 \cdot 10^2 s^5 + 4.1 \cdot 10^5 s^4 + 8.0 \cdot 10^7 s^3 + 3.1 \cdot 10^{10} s^2 + 2.7 \cdot 10^{12} s + 5.9 \cdot 10^{14}} \quad \text{(B.5)}$$

$$T_{16} = \frac{6.1 s^4}{s^4 + 3.4 \cdot 10^2 s^3 + 3.3 \cdot 10^5 s^2 3.3 \cdot 10^7 s 1.1 \cdot 10^{10}} \quad \text{(B.6)}$$

$$T_{21} = \frac{3.5 s^5 + 4.4 \cdot 10^2 s^4 - 1.3 \cdot 10^6 s^3 - 6.2 \cdot 10^8 s^2}{s^6 + 4.3 \cdot 10^2 s^5 + 4.1 \cdot 10^5 s^4 + 8.0 \cdot 10^7 s^3 + 3.1 \cdot 10^{10} s^2 + 2.7 \cdot 10^{12} s + 5.9 \cdot 10^{14}} \quad \text{(B.7)}$$

$$T_{22} = \frac{9.4 \cdot 10^1 s^5 + 8.2 \cdot 10^4 s^4 + 4.6 \cdot 10^7 s^3 + 1.9 \cdot 10^{10} s^2 + 2.7 \cdot 10^{12} s + 5.9 \cdot 10^{14}}{s^6 + 4.3 \cdot 10^2 s^5 + 4.1 \cdot 10^5 s^4 + 8.0 \cdot 10^7 s^3 + 3.1 \cdot 10^{10} s^2 + 2.7 \cdot 10^{12} s + 5.9 \cdot 10^{14}} \quad \text{(B.8)}$$

$$T_{23} = \frac{1.2 s^3 + 1.2 \cdot 10^3 s^2}{s^4 + 3.4 \cdot 10^2 s^3 + 3.3 \cdot 10^5 s^2 3.3 \cdot 10^7 s 1.1 \cdot 10^{10}} \quad \text{(B.9)}$$

$$T_{24} = \frac{3.0 \cdot 10^{-2} s^6 + 1.4 s^5 + 1.3 \cdot 10^3 s^4 + 5.4 \cdot 10^5 s^3 + 2.4 \cdot 10^8 s^2}{s^6 + 4.3 \cdot 10^2 s^5 + 4.1 \cdot 10^5 s^4 + 8.0 \cdot 10^7 s^3 + 3.1 \cdot 10^{10} s^2 + 2.7 \cdot 10^{12} s + 5.9 \cdot 10^{14}} \quad \text{(B.10)}$$

$$T_{25} = \frac{4.2 \cdot 10^{-1} s^6 + 1.3 \cdot 10^2 s^5 + 1.3 \cdot 10^5 s^4 + 1.3 \cdot 10^7 s^3 + 4.8 \cdot 10^9 s^2}{s^6 + 4.3 \cdot 10^2 s^5 + 4.1 \cdot 10^5 s^4 + 8.0 \cdot 10^7 s^3 + 3.1 \cdot 10^{10} s^2 + 2.7 \cdot 10^{12} s + 5.9 \cdot 10^{14}} \quad \text{(B.11)}$$

$$T_{26} = \frac{6.1 s^4}{s^4 + 3.4 \cdot 10^2 s^3 + 3.3 \cdot 10^5 s^2 3.3 \cdot 10^7 s 1.1 \cdot 10^{10}} \quad \text{(B.12)}$$

$$T_{31} = \frac{1.3 \cdot 10^3 s^3 + 7.2 \cdot 10^5 s^2}{s^4 + 3.4 \cdot 10^2 s^3 + 3.3 \cdot 10^5 s^2 3.3 \cdot 10^7 s 1.1 \cdot 10^{10}} \tag{B.13}$$

$$T_{32} = \frac{1.3 \cdot 10^3 s^3 + 7.2 \cdot 10^5 s^2}{s^4 + 3.4 \cdot 10^2 s^3 + 3.3 \cdot 10^5 s^2 3.3 \cdot 10^7 s 1.1 \cdot 10^{10}} \tag{B.14}$$

$$T_{33} = \frac{2.4 \cdot 10^2 s^3 + 2.7 \cdot 10^5 s^2 + 3.3 \cdot 10^7 s + 1.1 \cdot 10^{10}}{s^4 + 3.4 \cdot 10^2 s^3 + 3.3 \cdot 10^5 s^2 3.3 \cdot 10^7 s 1.1 \cdot 10^{10}} \tag{B.15}$$

$$T_{34} = \frac{6.1 s^4}{s^4 + 3.4 \cdot 10^2 s^3 + 3.3 \cdot 10^5 s^2 3.3 \cdot 10^7 s 1.1 \cdot 10^{10}} \tag{B.16}$$

$$T_{35} = \frac{6.1 s^4}{s^4 + 3.4 \cdot 10^2 s^3 + 3.3 \cdot 10^5 s^2 3.3 \cdot 10^7 s 1.1 \cdot 10^{10}} \tag{B.17}$$

$$T_{36} = \frac{1.2 \cdot 10^3 s^4 + 1.0 \cdot 10^5 s^3 + 5.6 \cdot 10^7 s^2}{s^4 + 3.4 \cdot 10^2 s^3 + 3.3 \cdot 10^5 s^2 3.3 \cdot 10^7 s 1.1 \cdot 10^{10}} \tag{B.18}$$

Appendix C

MATRIXx Source Files

The following pages contain source files for the MATRIXX simulations.

```
// this program  contains the numerical values for the matrixx model
//
//
// parameter selection

mx = 2.54;                    // mass of drive
my = 2.54;                    // mass of drive
I = .000934;                  // estimate of moment of inertia of drive
r= .005;                      // offset of drive CG from center of shock mounts
cf = .05;                     // .035 seems to be th- right scaling factor
wxd = 35*2*pi;                // observed damped natural frequency x-direction
wyd = 35*2*pi;                // y-direction
wtd = 75*2*pi;                // rotationally
dax = .20;                    // damping ratio  (i.e. percentage of critical
                              // damping)
day = .20;                    // y-dir damping
dat = .225;                   // rotational damping
wx = wxd/(sqrt(1 - dax**2));  // natural freq derivation from damped nf
wy = wyd/(sqrt(1-day**2));
wt = wtd/(sqrt(1-dat**2));


mtx = mx*r;                   // coupling effect of offset CG
mty = my*r;
bx = 2*dax*wx*(mx);               // effective damping in x-dir
by = 2*day*wy*(my);                // effective damping in y-dir
bt = 2*dat*wt*(I);           // effective damping in rot
kx=wx*wx*(mx);                    // effective stiffness in x-dir
ky = wy*wy*(my);            // effective stiffness in y-dir
kt = wt*wt*(I);            // effective stiffness in rotation
kxy=cf*(kx);                  // magnitude of stiffness coupling
bxy =cf*bx;                   // magnitude of damping coupling
nn=3;                         //
h = [0 0 0 0 0 1];            // output matrix    (x-dot,y-dot,rot-dot,x,y,rot)
q = [1;0;0];               // Matrix describing distribution and magnitude of
                              // inputs  (x,y,rot)
                              // scaling input factor for shaker inputs=1.7e5

m = [mx   0.0 - mtx;             // mass matrix
     0.0   my  -mty;
     -mtx -mty   i];

b = [bx  -bxy 0 ;           // damping matrix
    -bxy  by  0 ;
     0    0   bt];

k = [kx -kxy  0 ;             // stiffness matrix
    -kxy ky   0 ;
     0   0    kt];


m
b
k

pause;
```

```
// this program takes the mass, stiffness, and damping matrices
// and converts them into a system matrix
//  PROGRAM resp.
ERASE
resp='EXEC(''resp.'',1)';
exec('mbk.',1);

//  BUILD STATE-SPACE MODEL FROM EQUATIONS OF MOTION.
     INVM=INV(M);
//     F=[-INVM*B -INVM*K; EYE(nn) 0*EYE(NN)];
//     G=[INVM*Q; 0*ONES(NN,1)];
//     H=[1 0 0 0 0 0];
//     J=[0];

       F=[-invm*b -invm*k invm*b invm*k;
            eye(3)  0*eye(3) 0*eye(3) 0*eye(3);
           0*eye(3) 0*eye(3) 0*eye(3) 0*eye(3);
           0*eye(3) 0*eye(3) eye(3) 0*eye(3)];

       in = [  1 0 0;            //translational input
               0 1 0;
               0 0 1];

       inquire tqinp  'Enter 1 for Torque input (0) for none'
       g = [ 0*eye(3) tqinp*invm; 0*eye(3) 0*eye(3); in 0*eye(3);
               0*eye(3) 0*eye(3)];


       h = [-invm*b -invm*k invm*b invm*k ];

//   this section allows for viewing of various transfer functions
       inquire outvar 'Enter output variable # for FR'
       inquire invar  'Enter input variable  # for FR'

      //       outvar = 2;
      //       invar  = 1;
       gsize = size(g);
       numinp = gsize(2);
       hsize = size(h);
       numout = hsize(1);

       j = [0*eye(3) tqinp*invm]

//  FINAL STATE-SPACE PLANT
     S=[F G;H J];
     NS=12;
//
//
// GENERATE BODE PLOT OF PLANT:
    HZMIN=20; HZMAX=210; NPTS=600;
    FNORM=2*PI;
    [OMEGA,FR]=FREQ(S,NS,[HZMIN*FNORM; HZMAX*FNORM; NPTS],'CONT'):
    HZ=OMEGA/FNORM;
    FR=FR(:,(outvar-1)*numinp + invar); // selects freq response
    FRMAG=ABS(FR);
    DB=20*LOG(FRMAG)/LOG(10);
//      db=20*log(frmag+1e-2*ones(frmag))/log(10);
    PHASE=180/PI*IMAG(LOG(FR));
    PLOT(HZ,DB,'REPORT1 LOGX NOXLABEL CHART 5 95 50 100'),...
    PLOT(HZ,PHASE,'REPORT1 LOGX CHART 5 95 0 50 XLABEL/FREQUENCY - HZ/ ...
     TITLE/CONTINUOUS PLANT TRANSFER FUNCTION FREQUENCY RESPONSE/ ')
    PAUSE;
HARDCOPY
```

Appendix D

DOE-MACSYMA Source Files

This appendix contains the source files for the simulations run using DOE-MACYSMA.

```
/* This program computes the closed loop transfer function from an
external translational acceleration input to track position error
output.  This system is unfiltered. */
kill(all);
convert(exp):= if mapatom(exp) then exp
    else block([co,den],den:denom(exp),co:coeff(den,s,hipow(den,s)),
         multthru(1/co,num(exp))/multthru(1/co,denom(exp)))$
normalize(mat):=matrixmap(convert,mat)$
fpprintprec:8$
ratprint:false$
ee1: th = d*t - tau*t36$
ee2: tau = kt*(l*q*th- xe*cdet*kpa)$
ee3: xe = ktpd*(tau/iact -th)/(s^2)$
programmode:false$
ans: solve([ee1,ee2,ee3],[xe,th,tau]);
substitute(3.4277e4,ktpd,e10);
substitute(2.5839e-1,kt,%)$
substitute(9.8122e-5,iact,%)$
qq: substitute((.61693*s + 8.4186e2)/(s+4.6289e3),cdet,%)$
tt31: (1.335e3*s^3 + 7.228e5*s^2)/( s^4 + 3.437e2*s^3 + 3.31e5*s^2 +
3.308e7*s + 1.18e10)$
tt36: ( 1.239e3*s^4 + 1.051e5*s^3 + 5.691e7*s^2)/(s^4 + 3.437e2*s^3
+ 3.31e5*s^2 + 3.308e7*s + 1.18e10)$
substitute(tt31,t, qq)$
substitute(tt36,t36,%)$
substitute(1,d,%)$
substitute(1,q,%)$
xx: substitute(.21,kpa,%)$
zz: fullratsimp(%)$
v: rhs(zz)$
v: convert(v)$
fin:bfloat(v)$
fin: lhs(zz) = fin$
/* The variable fin: gives the closed loop transfer function in terms
of L and s.  */
nev: substitute(80*2*%pi*%i,s,xx)$
rn: realpart(num((rhs(nev))))$
in: imagpart(num((rhs(nev))))$
rd: realpart(denom((rhs(nev))))$
id: imagpart(denom((rhs(nev))))$
pov: (rn^2 + in^2)/(rd^2 + id^2)$
povs: fullratsimp(pov)$
povb: bfloat(povs)$
pn: num(povs)$
pd: denom(povs)$
mn: multthru(1.0e-72,pn)$
md: multthru(1.0e-72,pd)$
men:  expand(mn) $
med:  expand(md) $
ansv: men/med$
ansf: float(ansv);
/* ansf: gives an equation in terms of L that can be substituted into to
give the square of the position error due to an 80Hz external disturbance */
```

```
/* this program computes the closed loop transfer function from an
external translational acceleration to track position error (200Hz filter) */
kill(all);
convert(exp):= if mapatom(exp) then exp
    else block([co,den],den:denom(exp),co:coeff(den,s,hipov(den,s)),
         multthru(1/co,num(exp))/multthru(1/co,denom(exp)))$
normalize(mat):=matrixmap(convert,mat)$
fpprintprec:8$
ratprint:false$
ee1: th = d*t - tau*t36$
ee2: tau = kt*(l*q*th- xe*cdet*kpa)$
ee3: xe = ktpd*(tau/iact -th)/(s^2)$
programmode:false$
ans: solve([ee1,ee2,ee3],[xe,th,tau]);
substitute(3.4277e4,ktpd,e10);
substitute(2.5839e-1,kt,%)$
substitute(9.8122e-5,iact,%)$
qq: substitute((.61693*s + 8.4186e2)/(s+4.6289e3),cdet,%)$
tt31: (1.335e3*s^3 + 7.228e5*s^2)/( s^4 + 3.437e2*s^3 + 3.31e5*s^2 +
3.308e7*s + 1.18e10)$
tt36: ( 1.239e3*s^4 + 1.051e5*s^3 + 5.691e7*s^2)/(s^4 + 3.437e2*s^3
+ 3.31e5*s^2 + 3.308e7*s + 1.18e10)$
substitute(tt31,t, qq)$
substitute(tt36,t36,%)$
substitute(1,d,%)$
substitute((2*%pi*200)/(s^2 + 2*.7*2*%pi*200 + (2*%pi*200)^2),q,%)$
xx: substitute(.21,kpa,%)$
zz: fullratsimp(%)$
w: rhs(zz)$
w: convert(w)$
fin:bfloat(w)$
fin: lhs(zz) = fin$
/* fin: gives the closed loop transfer function in terms of L and s */
new: substitute(80*2*%pi*%i,s,xx)$
rn: realpart(num((rhs(new))))$
in: imagpart(num((rhs(new))))$
rd: realpart(denom((rhs(new))))$
id: imagpart(denom((rhs(new))))$
pov: (rn^2 + in^2)/(rd^2 + id^2)$
povs: fullratsimp(pov)$
povb: bfloat(povs)$
pn: num(povs)$
pd: denom(povs)$
mn: multthru(1.0e-72,pn)$
md: multthru(1.0e-72,pd)$
men:  expand(mn) $
med:  expand(md) $
ansv: men/med$
ansf: float(ansv);
/* ansf: gives an equation in terms of only L that can be substituted into
to give the square of the position error due to a 80Hz external disturbance */
```

```
/* This program computes the closed loop system transfer function from an
external translational acceleration to a position error.  This system has
a 400 Hz low pass filter. */
kill(all);
convert(exp):= if mapatom(exp) then exp
    else block([co,den],den:denom(exp),co:coeff(den,s,hipow(den,s)),
         multthru(1/co,num(exp))/multthru(1/co,denom(exp)))$
normalize(mat):=matrixmap(convert,mat)$
fpprintprec:8$
ratprint:false$
ee1: th = d*t - tau*t36$
ee2: tau = kt*(1*q*th- xe*cdet*kpa)$
ee3: xe = ktpd*(tau/iact -th)/(s^2)$
programmode:false$
ans: solve([ee1,ee2,ee3],[xe,th,tau]);
substitute(3.4277e4,ktpd,e10);
substitute(2.5839e-1,kt,%)$
substitute(9.8122e-5,iact,%)$
qq: substitute((.61693*s + 8.4186e2)/(s+4.6289e3),cdet,%)$
tt31: (1.335e3*s^3 + 7.228e5*s^2)/( s^4 + 3.437e2*s^3 + 3.31e5*s^2 +
3.308e7*s + 1.18e10)$
tt36: ( 1.239e3*s^4 + 1.051e5*s^3 + 5.691e7*s^2)/(s^4 + 3.437e2*s^3
+ 3.31e5*s^2 + 3.308e7*s + 1.18e10)$
substitute(tt31,t, qq)$
substitute(tt36,t36,%)$
substitute(1,d,%)$
substitute((2*%pi*400)/(s^2 + 2*.7*2*%pi*400 + (2*%pi*400)^2),q,%)$
xx: substitute(.21,kpa,%)$
zz: fullratsimp(%)$
v: rhs(zz)$
v: convert(v)$
fin:bfloat(v)$
fin: lhs(zz) = fin$
/* fin: gives the closed loop transfer function */
nev: substitute(80*2*%pi*%i,s,xx)$
rn: realpart(num((rhs(nev))))$
in: imagpart(num((rhs(nev))))$
rd: realpart(denom((rhs(nev))))$
id: imagpart(denom((rhs(nev))))$
pov: (rn^2 + in^2)/(rd^2 + id^2)$
povs: fullratsimp(pov)$
povb: bfloat(povs)$
pn: num(povs)$
pd: denom(povs)$
mn: multthru(1.0e-72,pn)$
md: multthru(1.0e-72,pd)$
men:  expand(mn) $
med:  expand(md) $
ansv: men/med$
ansf: float(ansv);
/* ansf: gives an equation in terms of only L that can be substituted into
to find the square of the position error due to a 80Hz external disturbance */
```

```
/* This progr.. computes the open loop trexitansfer function for use in the
root locus calculations.  This system is unfiltered */
kill(all);
convert(exp):= if mapatom(exp) then exp
    else block([co,den],den:denom(exp),co:coeff(den,s,hipow(den,s)),
         multthru(1/co,num(exp))/multthru(1/co,denom(exp)))$
normalize(mat):=matrixmap(convert,mat)$
fpprintprec:8$
ratprint:false$
ee1: Tau = kt*(LI + kpa*-1*cdet*ktpd*(1/s)*(1/s)*(tau*(1/iact) - th));
ee2: tau *-1*t36 = th;
ee3: th*q*1 = lout;
programmode:false$
ans: solve([ee1,ee2,ee3],[th,tau,lout]);
substitute(3.4277e4,ktpd,e10)$
substitute(2.5839e-1,kt,%)$
substitute(9.8122e-5,iact,%)$
qq: substitute((.61693*s + 8.4186e2)/(s+4.6289e3),cdet,%)$
tt31: (1.335e3*s^3 + 7.228e5*s^2)/( s^4 + 3.437e2*s^3 + 3.31e5*s^2 +
3.308e7*s + 1.18e10)$
tt36: ( 1.239e3*s^4 + 1.051e5*s^3 + 5.691e7*s^2)/(s^4 + 3.437e2*s^3
+ 3.31e5*s^2 + 3.308e7*s + 1.18e10)$
substitute(tt31,t, qq)$
substitute(tt36,t36,%)$
substitute(1,d,%)$
substitute(1,li,%)$
substitute(1,q,%)$
xx: substitute(.21,kpa,%)$
zz: fullratsimp(%)$
w: rhs(zz)$
w: convert(w)$
fin:bfloat(w)$
fin: lhs(zz) = fin$
/* the variable fin: gives the open loop transfer function */
```

```
/* This program computes the open loop transfer function for root
locus plots.  The system has a 200Hz low pass filter.  */
kill(all);
convert(exp):= if mapatom(exp) then exp
    else block([co,den],den:denom(exp),co:coeff(den,s,hipow(den,s)),
         multthru(1/co,num(exp))/multthru(1/co,denom(exp)))$
normalize(mat):=matrixmap(convert,mat)$
fpprintprec:8$
ratprint:false$
ee1: Tau = kt*(LI + kpa*-1*cdet*ktpd*(1/s)*(1/s)*(tau*(1/iact) - th));
ee2: tau *-1*t36 = th;
ee3: th*q*l = lout;
programmode:false$
ans: solve([ee1,ee2,ee3],[th,tau,lout]);
substitute(3.4277e4,ktpd,e10)$
substitute(2.5839e-1,kt,%)$
substitute(9.8122e-5,iact,%)$
qq: substitute((.61693*s + 8.4186e2)/(s+4.6289e3),cdet,%)$
tt31: (1.335e3*s^3 + 7.228e5*s^2)/( s^4 + 3.437e2*s^3 + 3.31e5*s^2 +
3.308e7*s + 1.18e10)$
tt36: ( 1.239e3*s^4 + 1.051e5*s^3 + 5.691e7*s^2)/(s^4 + 3.437e2*s^3
+ 3.31e5*s^2 + 3.308e7*s + 1.18e10)$
substitute(tt31,t, qq)$
substitute(tt36,t36,%)$
substitute(1,d,%)$
substitute(1,li,%)$
substitute(((200*2*%pi)^2)/(s^2 + 2*.7*2*%pi*200*s + (200*2*%pi)^2) ,q,%)$
xx: substitute(.21,kpa,%)$
zz: fullratsimp(%)$
w: rhs(zz)$
w: convert(w)$
fin:bfloat(w)$
fin: lhs(zz) = fin$
/* the variable fin: gives the open loop transfer function in terms of
L and s */
```

```
/* This program computes the open loop transfer function for root locus
use.  This system has a 400Hz filter.  */
kill(all);
convert(exp):= if mapatom(exp) then exp
    else block([co,den],den:denom(exp),co:coeff(den,s,hipov(den,s)),
         multthru(1/co,num(exp))/multthru(1/co,denom(exp)))$
normalize(mat):=matrixmap(convert,mat)$
fpprintprec:8$
ratprint:false$
ee1: Tau = kt*(LI + kpa*-1*cdet*ktpd*(1/s)*(1/s)*(tau*(1/iact) - th));
ee2: tau *-1*t36 = th;
ee3: th*q*l = lout;
programmode:false$
ans: solve([ee1,ee2,ee3],[th,tau,lout]);
substitute(3.4277e4,ktpd,e10)$
substitute(2.5839e-1,kt,%)$
substitute(9.8122e-5,iact,%)$
qq: substitute((.61693*s + 8.4186e2)/(s+4.6289e3),cdet,%)$
tt31: (1.335e3*s^3 + 7.228e5*s^2)/( s^4 + 3.437e2*s^3 + 3.31e5*s^2 +
3.308e7*s + 1.18e10)$
tt36: ( 1.239e3*s^4 + 1.051e5*s^3 + 5.691e7*s^2)/(s^4 + 3.437e2*s^3
+ 3.31e5*s^2 + 3.308e7*s + 1.18e10)$
substitute(tt31,t, qq)$
substitute(tt36,t36,%)$
substitute(1,d,%)$
substitute(1,li,%)$
substitute(((400*2*%pi)^2)/(s^2 + 2*.7*2*%pi*400*s + (400*2*%pi)^2) ,q,%)$
xx: substitute(.21,kpa,%)$
zz: fullratsimp(%)$
v: rhs(zz)$
v: convert(v)$
fin:bfloat(v)$
fin: lhs(zz) = fin$
/* the variable fin: gives the open loop transfer function in terms of
L and s.  */
```

```
/* This program converts the transfer function matrix based on the mass,
damping, and stiffness matrices derived previously. */
kill(all)$
ratprint:false$
fpprintprec:2$
doallmxops:true$
listarith:true$
convert(exp):= if mapatom(exp) then exp
    else block([co,den],den:denom(exp),co:coeff(den,s,hipow(den,s)),
         multthru(1/co,num(exp))/multthru(1/co,denom(exp)))$
normalize(mat):=matrixmap(convert,mat)$
ratmx:true$
m: matrix([2.54,0,-1.27e-2],[0,2.54,-1.27e-2],[-1.27e-2,-1.27e-2,9.34e-4])$
b:matrix([223.4,-7.820,0],[-7.820,223.4,0],[0,0,.1981])$
k:matrix([1.228e5,-6.14e3,0],[-6.14e3,1.228e5,0],[0,0,207.41])$
i:matrix([1,0,0],[0,1,0],[0,0,1])$
id: ident(12)$
z:  zeromatrix(3,3)$
f: 0*id$
im: (m^^-1)$
iib: (-im.b)$
iik: (-im.k)$
ib: (im.b)$
ik: (im.k)$
for y:1 thru 3  do
        for x: 1 thru 3 do
                f[y,x]: iib[y,x]$
for y:1 thru 3  do
        for x: 1 thru 3   do
                f[y,x+3]: iik[y,x]$
for y:1 thru 3  do
        for x: 1 thru 3  do
                f[y,x+6]:  ib[y,x]$
for y:1 thru 3  do
        for x: 1 thru 3 do
                f[y,x+9]: ik[y,x]$
for y:1 thru 3  do
        for x: 1 thru 3  do
                f[y+3,x]: i[y,x]$
for y:1 thru 3  do
        for x: 1 thru 9  do
                f[y+3,x+3]: 0$
for y:1 thru 3  do
        for x: 1 thru 12  do
                f[y+6,x]: 0$
for y:1 thru 3   do
        for x: 1 thru 6 do
                f[y+9,x]: 0$
for y:1 thru 3  do
        for x: 1 thru 3  do
                f[y+9,x+6]:  i[y,x]$
for y:1 thru 3  do
        for x: 1 thru 3  do
                f[y+9,x+9]: 0$
g: zeromatrix(12,6)$
for y:1 thru 3  do
        for x: 1 thru 3  do
                g[y,x]: 0$
for y:1 thru 3  do
        for x: 1 thru 3  do
                g[y,x+3]: im[y,x]$
for y:1 thru 3  do
        for x: 1 thru 6  do
                g[y+3,x]: 0$
for y:1 thru 3  do
        for x: 1 thru 3  do
```

```
                g[y+6,x]: i[y,x]$
for y:1 thru 3  do
        for x: 1 thru 3  do
                g[y+6,x+3]: 0$
for y:1 thru 3  do
        for x: 1 thru 6  do
                g[y+9,x]: 0$
h: zeromatrix(3,12)$
for y:1 thru 3  do
        for x: 1 thru 3 do
                h[y,x]: iib[y,x]$
for y:1 thru 3  do
        for x: 1 thru 3   do
                h[y,x+3]: iik[y,x]$
for y:1 thru 3  do
        for x: 1 thru 3  do
                h[y,x+6]:  ib[y,x]$
for y:1 thru 3  do
        for x: 1 thru 3 do
                h[y,x+9]: ik[y,x]$

j: zeromatrix(3,6)$
for y:1 thru 3  do
        for x: 1 thru 3 do
                j[y,x]: 0$
for y:1 thru 3  do
        for x: 1 thru 3 do
                j[y,x+3]: im[y,x]$
vv: (h.((s*id-f)^^-1).g + J)$
t:ratsimp(vv)$
t: normalize(t)$
t: bfloat(t)$

t;

/* t is the transfer function matrix */
```

Bibliography

[1] Robert A. White. *Shock Force Compensating System*, United States Patent 4.040,103, August 2, 1977.

[2] Knowles, Vernon Lynn and Darwin Mitchell Hanks. *Shock and Vibration Disturbance Compensation for Disc Drives*, United States Patent Claim 922585, October 24, 1986.

[3] Knowles, Vernon Lynn and Darwin Mitchell Hanks. *Shock and Vibration Disturbance Compensation for Disc Drives*, European Patent Application 0 264 535, May 6, 1987.

[4] Mitsuro Moriya, Kazuharu Shiragami, and Hiroyuki Yamaguchi. *Recording and Reproduction Apparatus Having Improved Reliability with Respect to Externally Applied Vibration or Impact*, United States Patent 4,692,915, September 8, 1987.

[5] Keiji Aruga, Yoshifumi Mizoshita, Masahito Iwatsubo, and Toshifumi Hatagami. *Control System of Magnetic Head Positioners of a Multipositioner Magnetic Disk Storage Apparatus*, European Patent Application 0 306 715, March 15, 1989.

[6] Keiji Aruga, Yoshifumi Mizoshita, Masahito Iwatsubo, and Toshifumi Hatagami. *Acceleration Feedforward Control for Head Positioning in Magnetic Disk Drives*, The International Conference on Advanced Mechatronics, Tokyo, Japan, May 21-24, 1989.

[7] Eric M. Dunstan, Dennis Hogg, John E. Scura, and Ming-Goei Sheu, *Shock Resistant Winchester Disk Drive*, United States Patent 4,947,093, June 7, 1990.

[8] Class Notes, Dynamics, Prof. J. H. Williams, Jr., Massachusetts Institute of Technology, Spring, 1989.

[9] Robert H. Cannon, Jr., *Dynamics of Physical Systems*, McGraw-Hill, New York, 1967, p. 248.

[10] MATRIXx User's Guide, Version 6.0, Integrated Systems Inc., Palo Alto, CA, May, 1986.

[11] Macsyma Reference Manual, Version 10, Mathlab Group, Massachusetts Institute of Technology. Cambridge, MA., January, 1983.

[12] STARModal Guide, Version 2.00, Structural Measurement Systems, Milpitas, CA, June 1989.

[13] Joe Thornhill, *Modal Analysis Theory and Experimental Technique: A Short Course*, GSD AUSTIN, 550/003, Tieline 678 x3746.